

Condition Assessment of Overhead Line Insulators using Advanced Techniques

Thesis Submitted by
Kaushik Sit

Doctor of Philosophy (Engineering)

Electrical Engineering Department
Faculty Council of Engineering & Technology
Jadavpur University
Kolkata, India

2023

**JADAVPUR UNIVERSITY
KOLKATA-700032, INDIA**

INDEX NO. 121/19/E

1. Title of the thesis

*Condition Assessment of Overhead Line Insulators using
Advanced Techniques*

**2. Name, Designation and Institution of the
Supervisors**

Dr. Sovan Dalai

Professor

Electrical Engineering Department

Jadavpur University

Kolkata 700032

Dr. Arpan Kumar Pradhan

Assistant Professor

Electrical Engineering Department

Jadavpur University

Kolkata 700032

Proforma-1
Statement of Originality

I, **Kaushik Sit**, registered on 11th June 2019 declare that this thesis entitled "**Condition Assessment of Overhead Line Insulators using Advanced Techniques**" contains a literature survey and original research work done by the undersigned candidate as part of doctoral studies.


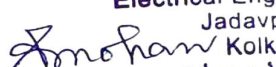
All information in this thesis have been obtained and presented in accordance with existing academic rules and ethical conduct. I declare that, as required by these rules and conduct, I have fully cited and referred all materials and results that are not original to this work.

I also declare that I have checked this thesis as per the "Policy on Anti Plagiarism, Jadavpur University, 2019", and the level of similarity as checked by iThenticate software is 2 %.

Signature of Candidate: *Kaushik Sit*

Date: 19/9/2023


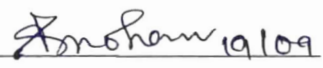
Certified by Supervisor(s):
(Signature with date, seal)

1. 
19/09/2023
Dr. Sovan Dalai
Professor
Electrical Engineering Department
Jadavpur University
Kolkata-700032
2. 
19/09/2023
Dr. Arpan Kr. Pradhan
Assistant Professor,
Electrical Engineering Department
Jadavpur University
Kolkata-700032

Proforma-2

Certificate from the supervisors

This is to certify that the thesis entitled “**Condition Assessment of Overhead Line Insulators using Advanced Techniques**” submitted by Shri **Kaushik Sit**, who got his name registered on 11th June 2019 (Registration no. 1021906007) for the award of Ph. D. (Engineering) degree of Jadavpur University, is absolutely based upon his work under the joint supervision of Prof. Sovan Dalai along with Dr. Arpan Kumar Pradhan and that neither his thesis nor any part of the thesis has been submitted for any degree/diploma or any other academic award anywhere before.

1.  19/09/2023.  19/09/2023

Signature of the Supervisor and date
with Official Seal

Signature of the Supervisor and date
with Official Seal
Dr. Arpan Kr. Pradhan
Assistant Professor,
Electrical Engineering Department
Jadavpur University
Kolkata-700032

Dr. Sovan Dalai
Professor
Electrical Engineering Department
Jadavpur University
Kolkata-700032

Acknowledgement

The author would like to extend his most sincere appreciation and profound gratitude to his supervisors Prof. Sovan Dalai and Dr. Arpan Kumar Pradhan of the Electrical Engineering Department, Jadavpur University, for their invaluable guidance and constant encouragement in carrying out the research work. The author has all the necessary freedom during the research work. At the same time, the intense supervision by the supervisors helped enhance the research quality.

The author would like to express his sincere gratitude and deep appreciation to Prof. Biswendu Chatterjee, Professor of Electrical Engineering Department, Jadavpur University and Dr. Debangshu Dey, Associate Professor of Electrical Engineering Department, Jadavpur University, for their active involvement, assistance, advice, and valuable suggestions in carrying out the research work.

The author is grateful to the Head of the Electrical Engineering Department, Jadavpur University, for providing the laboratory facilities required for carrying out this work.

The author is thankful to his co-research scholars, namely Dr. Suhas Deb, Dr. Arup Kumar Das, Mr. Biswajit Chakraborty, Mr. Subhajit Maur, Mr. Rakesh Das, Mr. Sandipan Paul, Mr. Pradipta Ghosh (NIT Mizoram) and Mr. Soumydeep Maity (NIT Mizoram) for providing their continuous emotional support and for making the laboratory an exciting place to work.

The author would also like to thank his superiors Dr. Nasirul Haque (Assistant Professor, NIT Calicut), Dr. Arijit Baral (Assistant Professor, IIT ISM Dhanbad), Dr. Riddhi Ghosh (Research Scientist, Hitachi Energy Ltd., Sweden), Mr. Arijit Basuroy (Managing Director, NTPL Pvt. Ltd.) and Ms. Keya Sit (Cyber Defence Analyst, Transurban Ltd.) for providing enormous technical support at every stage of the research work.

The author would like to convey his deep love and respect towards his parents (Late Shri Kanai Lal Sit and Smt. Kalpana Sit) and sister (Ms. Kakali Sit) for their never-ending support and encouragement during difficult times. Without their support, this work could never have been completed.

Last but not the least; the author would like to thank those persons whose names are not mentioned here who have contributed to bringing this work to its present stage.

Kaushik Sit

KAUSHIK SIT
September 2023

Contents

Chapter 1	Page No.
Condition Assessment of Overhead Line Insulators	1 – 47
1.1. Introduction	1
1.2. Importance of Overhead line Insulators	2
1.3. Types of Overhead line insulators	3
1.3.1. Silicone Rubber (SiR) Insulator	3
1.3.2. Non-Polymeric Insulators	7
1.3.2.1. Porcelain Insulator	7
1.3.2.2. Glass Insulator	9
1.4. Factors for Degradation of Overhead Line Insulators	10
1.4.1. Effect of Environmental Factors	10
1.4.1.1 Effect of Temperature	12
1.4.1.2 Effect of Moisture	13
1.4.1.3 Effect of Rain Falls	14
1.4.1.4 Effect of Salt and Dust	14
1.4.2 Effect of Thermal Stress	15
1.4.3 Effect of Electrical Stress	16
1.4.4 Effect of Mechanical Stress	16
1.4.5 Effect of Chemical Reaction	17
1.4.6 Effect of Aging	18
1.4.6.1 Effect of Thermal Aging	18
1.4.6.2 Effect of Ultraviolet (UV) Aging	19
1.5. Parameters to Determine the Condition of Overhead Line Insulators	20
1.5.1 Equivalent Salt Deposit Density (ESDD)	20
1.5.2 Non-soluble Salt Deposit Density (NSDD)	20
1.5.3 Electrical Parameters	20
1.5.3.1 Flashover Voltage	21
1.5.3.2 Puncture Voltage	21
1.5.3.3 Surface Leakage Current (SLC)	21
1.6. Condition Assessment Techniques of Overhead Line Insulators	22
1.6.1 Importance of Condition Assessment Techniques of Overhead Line Insulators	23
1.6.2 Types of Condition Assessment Techniques of Overhead Line Insulators	23
1.6.2.1 Analysis of Physical Properties	24
1.6.2.1.1 Hydrophobicity	24
1.6.2.1.2 Accumulation of Pollutants on the Insulators Surface	26
1.6.2.2 Analysis of Chemical Properties	28

1.6.2.2.1	Fourier Transform Infrared (FT-IR) Spectroscopy	28
1.6.2.2.2	Energy Dispersive X-Ray (EDX) Technique	29
1.6.2.2.3	X-Ray Diffraction (XRD) Technique	30
1.6.2.2.4	X-Ray Photoelectron Spectroscopy (XPS) Technique	30
1.6.2.2.5	Secondary Ion Mass Spectroscopy (SIMS) Method	31
1.6.2.2.6	Surface Roughness / Scanning Electron Microscope Technique	31
1.6.2.2.7	Gas Chromatography (GC) / Mass Spectroscopy Technique	32
1.6.2.2.8	Solvent Extraction (SE _x) Technique	32
1.6.2.2.9	Terahertz and Laser Induced Spectroscopy Method	33
1.6.2.3	Analysis of Electrical Property	34
1.6.2.3.1	Surface Leakage Current Analysis	34
1.6.2.3.1.1	Factors for Estimating the Surface Degradation of Overhead Line Insulators	35
1.6.2.3.1.1.1	Amplitudes of Surface Leakage Current	35
1.6.2.3.1.1.2	Ratio of 5 th to 3 rd Harmonic Components of Surface Leakage Current Harmonics	37
1.6.2.3.1.1.3	Calculation of Total Harmonics Distortion (THD)	38
1.6.2.3.1.1.4	Calculation of Phase Angle	39
1.6.2.3.2	Partial Discharge (PD) and Corona Discharge Analysis	39
1.6.2.3.3	Analysis of Flashover Voltage (FOV)	41
1.6.2.3.4	Erosion and Tracking Resistance Analysis	42
1.7	Scope of the Thesis	45
1.8	Originality of the Thesis	46
 Chapter 2		
Experimental Setup for Surface Leakage Current Signature Acquisition and Procedure of Artificially Contaminated Sample Preparation		48 – 62
2.1.	Introduction	48
2.2.	Experimental Procedure	50
2.2.1.	Preparation of Samples	50

2.2.2. Experimental Setup for Data Acquisition of Surface Leakage Current (SLC)	52
2.2.2.1 Major Components used in the Experimental Setup	53
2.2.2.2 Extraction of Surface Leakage Current (SLC) Signals and Input Voltage	58
2.3. Estimation of Equivalent Salt Deposit Density (ESDD)	60
2.4. Conclusion	62

Chapter 3

Classification of Contamination Levels by Measuring the Leakage Current of Porcelain Insulator with the help of Mathematical Morphology and Random Forest Classifier 63 – 75

3.1 Introduction	63
3.2 Classification of Artificial Surface Contamination of Porcelain Insulators	64
3.3 Surface Leakage Current Signals Acquisition Setup	65
3.3.1 Effect of Contamination Severity on Surface Leakage Current Signal	66
3.4 Features Extraction from Surface Leakage Current Signal	67
3.4.1 Fundamental Concept of Mathematical Morphology	67
3.4.2 Extracted Features after Mathematical Morphology Operation	67
3.5 Procedure of Features Classification	69
3.5.1 Feature Selection using Filter Method	69
3.5.2 Features Classification using Random Forest (RF) Classifier	71
3.5.2.1 Working Strategy of Random Forest (RF) Classifier	72
3.6 Results and Discussions	73
3.7 Conclusion	75

Chapter 4

Condition Assessment of Overhead Line Silicone Rubber Insulators by Employing Surface Leakage Current Signal and Hyperbolic Stockwell Window Transform 77 – 100

4.1 Introduction	77
4.2 Artificial Contamination of SiR insulator	80
4.2.1 Preparation of Samples	80
4.2.2 Description of Contamination Classes	81
4.3 Acquisition of Surface Leakage Current (SLC) Signal	81

4.4 Features Extraction by Hyperbolic Stockwell Transform (HST)	82
4.4.1 Fundamental of Hyperbolic Window Stockwell Transform (HST)	82
4.4.2 Tuning of Hyperbolic Stockwell Window Parameters	84
4.4.3 Time-Frequency Domain's Extracted HST Features	85
4.5 Machine Learning Classifiers	87
4.5.1 Support Vector Machine (SVM)	87
4.5.2 k-Nearest Neighbor (k-NN)	89
4.5.3 Gaussian Naïve Bayes (GNB)	90
4.5.4 Random Forest (RF)	91
4.6 Results and Discussion	91
4.6.1 Variation of Surface Leakage Current (SLC) Signal for Various Contamination Levels	91
4.6.2 Analysis of Selected HST Features	92
4.6.3 Performance Analysis of Machine Learning Classifiers	96
4.6.4 Comparative Study on Other Time-Frequency Methods	98
4.7 Conclusion	100

Chapter 5

Time-Frequency Domain Analysis of Leakage Current Signal of Overhead line Polymeric Insulator by Cross Hyperbolic Stockwell Transform Aided Fine-Tuned Convolutional Neural Network Technique	101 - 117
5.1 Introduction	101
5.2 Basic Concept of Hyperbolic Stockwell Transform (HST)	103
5.2.1 Window Parameter Tuning of Hyperbolic Stockwell Transform (HST)	105
5.2.2 Effect of Contamination Severity on Surface Leakage Current Signal	106
5.3 Convolutional Neural Network (CNN) Base Approach	108
5.3.1 Transfer Learning Aided Fine-Tuning Approach to Proposed CNN Model	110
5.4 Results and Discussion	113
5.4.1 Evaluation of the Proposed Framework's Performance	113
5.4.2 Impact of Fine-Tuning on Pre-Trained Architecture System	114
5.4.3 Comparison with other Time-Frequency Imaging Techniques	115

5.4.4 Validation with Different Dimensions SiR	115
Insulator	117
5.5 Conclusion	
Chapter 6	
Conclusions and Future Scope	118 - 121
6.1 Conclusions	118
6.2 Scope of Future Work	120
References	122 - 140

Preface

Most of overhead line insulators are employed for outdoor applications, due to which environmental pollutants accumulate on the surface of outdoor insulators. Notably, incremental surface contamination reduces surface insulation resistance. As a result, the surface conductivity of overhead line insulators also changes. The outer surface of overhead line insulators is mainly affected by different climatic conditions like fog, raindrops, dew, sea salt, sand, dust, soil, and air pollution. In coastal areas, predominant environmental contaminants such as sand, dirt, and soluble salt (NaCl) accumulate on the surface of overhead line insulators. In rainforest regions, the pollutant is mainly Kaolin ($\text{Al}_2\text{Si}_2\text{O}_5(\text{OH})_4$), which accumulates on the surface of overhead line insulators. The clean surface of overhead line insulators cannot form a conductive path with water particles in humid conditions because the water particles are deposited on the clean surface as a droplet instead of making a water film.

On the other hand, accumulated pollutants degrade the surface insulating property of overhead line insulators. Soluble pollutants can easily mix with molecules of water and then develop conduction paths on the surface of overhead line insulators. As a result, the surface leakage current flows through the contaminated housing of overhead line insulators. The amplitude of the surface leakage current relies mainly on the dissolved soluble pollutants. It is worth noting that higher levels of contamination increase the leakage current flow at the insulators' surface. The surface temperature of the overhead line insulator is also increased due to the joule-heating effect. As a result, the water molecules partially evaporate from the wet surface, causing dry bands to form, followed by dry band discharge phenomena on the surface of the overhead line insulators. Because of the localized dry band formation, the voltage is not uniformly distributed across the surface of the insulator. Ultimately, flashover events occur in overhead line insulators for the reasons mentioned above, leading to the premature failure of overhead line insulators. Therefore, scheduled condition monitoring of overhead line insulators for an uninterrupted power supply is essential.

In order to address the surface condition of the overhead line insulators and prevent them from premature failure, it is essential to establish techniques which correlate with the surface contamination levels of overhead line insulators. To identify the degree of surface contamination, different methods are implemented, such as Non-soluble Salt Deposit Density or NSDD, equivalent salt deposit density or ESDD, leakage current measurement, flashover voltage test, and air pollution. Among them, the surface leakage current signal is a dynamic parameter because it varies with changes in pollution intensity. It is noteworthy that surface leakage current measurements are more consistent and effective than traditional methods. In this reported thesis work, based on the measurement of leakage current approach helps to identify the severity of the surface degradation of overhead line insulators. Different advanced approaches to assessing the surface condition of overhead line insulators are demonstrated in various chapters of the thesis.

In the second chapter of the thesis work, an experimental setup has been used to acquire the surface leakage current (SLC) signals in the laboratory. Additionally, an elaborate discussion of the different components of the hardware setup is presented in this chapter. In this regard, artificially contaminated samples of overhead line insulators are prepared in the laboratory. Besides that, the severity of surface contamination is classified as per the IEC 60815 standard. The detailed procedure to acquire the surface leakage current signals using an experimental setup according to the IEC 60507 standard is demonstrated in this chapter. Notably, experimental observation reveals that leakage current becomes distorted and non-stationary as the surface contamination severity increases. After the SLC data acquisition, that data is stored on the computer for data analysis purposes.

In the third chapter, a framework has been presented that applies mathematical morphology on surface leakage current signals in order to extract significant features about surface contamination severity. In this regard, the SLC signals corresponding to the different contamination levels are recorded. It is noteworthy to mention that the signature of the SLC is dependent on the input voltage magnitude and sensitive to the degradation level of the surface contamination. Mathematical morphology is applied in the proposed model to capture

local features of SLC leakage current, which can be useful to classify the SLC of overhead line insulators corresponding to different surface contamination levels. Apart from this, the proposed filter technique can efficiently eliminate unwanted features and provide optimal features, which improve the proposed framework's prediction accuracy. After that, the extracted features are fed to a Random Forest (RF) classifier to identify the contamination level of overhead line insulators based on the morphological features. The results show that extracted features of mathematical morphology can predict overhead line insulators' surface contamination severity with satisfactory results for the RF classifier. Although the mathematical morphology-aided approach shows very satisfactory performance on the nonlinear SLC signals, but framework requires additional information about the input voltage profile. However, on field measurement of input voltage is a very difficult task, which requires more protective measures and apparatus. It is noteworthy to mention that employing the proposed filter model with mathematical morphology operation for acquiring features from SLC signals is time-consuming and cumbersome. In addition, the process of mathematical morphological technique depends on structural element dimensions. On the opposite side, assigning the dimension of the structural elements depends on the signature of the input signal, which is complicated. Notably, the proposed model's success rate has been examined with only one machine learning classifier (i.e., Random Forest). With respect to this, it is impractical to validate the proposed framework for the identification of surface contamination levels of overhead line insulators.

In chapter four, an integrated time-frequency signal processing technique has been applied to SLC signals to overcome the flaws mentioned in the mathematical metaphorical-based model. Using a data acquisition experimental setup, SLC signals of different contamination classes are acquired and converted into a joint time-frequency image data bank by Hyperbolic Stockwell Transform (HST). In addition, HST provides different statistical features from the image bank as output features. Optimal features are extracted using the LASSO regression technique to improve the model's outcome. Notable, the framework's performance is validated in comparison with four benchmark classifiers such as Support Vector Machine (SVM), Random Forest (RF),

Gaussian Naïve Bayes (GNB) and k-Nearest Neighbor (k-NN). The outcome indicates that the proposed framework returns satisfactory performance regarding the surface contamination severity assessment of overhead line insulators. In contrast, the proposed framework's feature classification process is a supervised learning approach, which is cumbersome. The generated features matrix from the HST method can only be utilized if it is arranged as input and output variables for supervised feature classification. Also, the process of feature extraction in HST aided approach is handcrafted. Besides that, the classifier models must perform iterative operations based on the training dataset to predict the correct contamination level. It has been observed that the proposed model's algorithm is terminated when it reaches an acceptable performance level. That is why it is time-consuming to predict the contamination class of the overhead line insulators.

In chapter five of the thesis, a deep learning-aided framework has been implemented to extract features from cross time-frequency spectrum of SLC signals automatically. By using the cross hyperbolic Stockwell transform (XHST) approach, the distinct characteristics of surface leakage current (SLC) signal at different surface contamination levels of overhead line insulator samples have been revealed. Notably, the extracted features are not affected by external noise and the aliasing effects. Furthermore, the XHST method is a powerful tool for detecting surface contamination because it is cross-correlated with a reference signal (i.e., the SLC at the clean surface of the overhead line insulator). In addition, time-frequency cross-spectrum images are fed to a pre-trained CNN architecture (i.e., VGGNet-16). Automatic feature extraction and classification are achieved using the transfer learning strategy with fine-tuning techniques to train VGGNet-16 architecture. The performance of the proposed model is validated for any dimension of the overhead line insulators. In a deep learning framework, feature extraction is fully automated, and the abundant features are eliminated without any supervision. The cross-spectrum deep learning framework described here is simple, accurate, and robust, which makes it potentially suitable for predicting overhead line insulators' surface contamination severity. The pre-trained deep VGGNet-16 architectures' major advantage is the process of feature extraction and the prediction of the contamination classes is automatic. This significantly reduces the

effort and time needed to develop a model for a specific task. Furthermore, the pre-conditioned deep learning models can be further fine-tuned over a few epochs to validate the model performance for any dimension's overhead line insulators.

Chapter six summarizes the thesis work, such as research gaps, findings and comparison between existing research work and the proposed research model. The author describes the possible research opportunities and developments in the condition assessment study of overhead line insulators.

Kaushik Sit

KAUSHIK SIT
September 2023

List of Figures

Figure No.	Figure Caption	Page No.
1.1	Image of Silicone Rubber (SiR) Insulators (i.e., 11 kV and 33 kV)	3
1.2	Image of Chemical Construction of Polydimethylsiloxane (PDMS) (a) PDMS Solo unit monomer, (b) Cyclic PDMS molecule	4
1.3	Cross-sectional image of physical structure of Silicone Rubber (SiR) insulator	6
1.4	Picture of a 11 kV Porcelain Insulator Disc	8
1.5	Picture of a 11 kV Glass Insulator Disc	9
1.6	A schematic representation of Contact Angle (CA) (a) Static Contact Angle, (b) Dynamic Contact Angle	25
1.7	The patterns of the LC waveform vary with the contamination levels: (a) Very Light, (b) Light, (c) Moderate, (d) High and (e) Extremely High contamination, respectively.	36
2.1	Images of deposited water droplets on the surface of overhead line insulators	48
2.2	Images of different types of contaminated overhead line insulators	51
2.3	Flowchart of artificial surface contamination process using solid layer method	52
2.4 (a)	Schematic diagram of Surface Leakage Current (SLC) data acquisition system	52
2.4 (b)	Actual Hardware setup for Surface Leakage Current (SLC) measuring system	52
2.5 (a)	High Voltage on-load Voltage Regulator (VR)	53
2.5 (b)	High Voltage Auto-transformer	54
2.5 (c)	High Voltage Testing Transformer	54
2.6	High Voltage Potential Divider	55
2.7 (a)	Image of Actual Control Panel	55
2.7 (b)	Schematic diagram of Actual Control Panel	56
2.8	Image of the Water Resistance	56
2.9 (a)	Pictures of Protective Current Shunt Circuit	57
2.9 (b)	Image of Digital Storage Oscilloscope (DSO) during the SLC experiment.	57

2.10 (a)	Waveform of acquired Surface Leakage Current (SLC) signals of five different classes of contamination such as (a) Very Light, (b) Light, (c) Moderate, (d) High and (e) Very High contamination	59
2.10 (b)	Waveform of input voltage profile of five different classes of contamination such as (a) Very High, (b) High, (c) Moderate, (d) Light and (e) Very Light contamination	60
2.11	Conductivity Meter (HANNA)	61
3.1	Photography of artificially surface contaminated and uncontaminated porcelain insulators	65
3.2	The waveform of the acquired Surface Leakage Current (SLC) signals representing five distinct categories of contamination, including Very Light, Light, Moderate, High, and Very High	66
3.3	Infographics of the Filter Method	71
3.4	Schematic of Random Forest Classifier	73
4.1	Waveforms of surface leakage current signal for (a) High and (b) Extremely high contamination level	79
4.2	Image of artificially contaminated SiR insulator (11 kV)	81
4.3	Outline of Grid Search Optimization.	85
4.4	Schematic diagram of Multiclass SVM construction	89
4.5	SLC waveform of SiR insulator for class: (a) CL-1 (b) CL-2 (c) CL-3 (d) CL-4 and (e) CL-5	92
4.6	Magnitude contour plots of SLC converted Hyperbolic Stockwell (HS) matrix for class (a) CL-2 (ρ_H^F , ρ_H^B and $\beta_H = 0.11, 0.23$ and 307) (b) CL-3 (ρ_H^F , ρ_H^B and $\beta_H = 0.11, 0.21$ and 324.5) and (c) CL-5 (ρ_H^F , ρ_H^B and $\beta_H = 0.12, 0.23$ and 321.5)	93
4.7	Box-whisker plot of time-frequency HST features of SLC signal: (a) F-2 (b) F-3 (c) F-7 (d) F-9 (e) F-14	96

4.8	Outline of the recommended model for contamination class predictions for overhead line SiR insulators	97
5.1	XHST spectrum images of surface leakage current correspond to (a) Very Light (VL) (b) Light (L) (c) Moderate (M) (d) High (H) and (e) Very High (VH) surface contamination severity.	107
5.2	Schematic diagram of Convolutional Neural Network (CNN) architecture	109
5.3	Training and validation performance of the proposed CNN module using XHST image dataset	111
5.4	Proposed transfer learning framework with a fine-tuning strategy to identify contamination classes	112
5.5	Image of Actual Hardware Setup for SLC Measurement using of 33 kV rated SiR Insulator	116
5.6	Validation Performance of the Proposed CNN framework	116

List of Tables

Table No.	Table Caption	Page No.
1.1	Various types of filler elements and their characteristics	5
1.2	Technical Specifications of 11 kV and 33 kV SiR insulators	7
1.3	Technical Specifications of 11 kV Porcelain Insulator Disc	9
1.4	Technical Specifications of 11 kV Glass insulator Disc	10
1.5	Various types of Environmental Pollinating Sources for the Overhead Line Insulators	11
1.6	Summary of various external factors and their effects on SiR Insulators	22
1.7	Relationship among the Contact Angle, surface condition of the insulator, physical condition of the insulator and contamination level (ESDD)	26
1.8	A description of the different categories of contamination classes	27
1.9	Pollution parameters before and after UV aging of SiR insulators	28
1.10	Comparison study of SEM-EDX results	30
1.11	Results for HTV-SiR insulator samples after the aging test using XPS analysis under different conditions	31
1.12	Results of the Solvent Extraction method of HTV-SiR	33
1.13	Porcelain and SiR insulators Leakage Current's deviations with environmental constraints	36
1.14	Comparative Analysis of Leakage Current Flow, Power Dissipation and Surface Resistance of Aged SiR Insulators	38
1.15	Representation of odd LC harmonics in surface flashover before and after UV exposure	42
1.16	Comparative analysis of Tracking and Erosion properties of various SiR additives	43
1.17	Comparative analysis of various Inorganic Fillers of SiR Insulators	44

2.1	Technical properties of both SiR and Porcelain disc insulators	50
2.2	Technical specification and function of current shunt protective device	58
2.3	Classification of contamination level based on ESDD range and amount of NaCl salt	62
3.1	Features Description	69
3.2	Acquired Features after Mathematical Morphology operation	70
3.3	Result of Filter Methodology	74
4.1	Features extracted from the HS matrix	86
4.2	Selection of true features by LASSO from the HST features	95
4.3	Classifiers performance by the proposed method	98
4.4	Comparative Performance analysis with other time-frequency methods	99
4.5	Comparative analysis with existing methods	99
5.1	Training Parameter of Pre-trained VGGNet-16 Model	111
5.2	Performance of Fine-Tuned Proposed CNN Model for Different Training Parameters	113
5.3	Performance of Pre-Trained Proposed CNN Model	114
5.4	Comparison Study with Different Time-Frequency Strategies	115
5.5	Technical Specification of 33 kV SiR Insulator	115

List of Abbreviations and Symbols

Symbols and Abbreviations	Description
%	Percentage
$\hat{\partial}_c$	Crystal's Refractive Index
$\hat{\partial}_s$	Sample's Refractive index
μl	Micro-litter
A_w	Weight of the Atom
1- ϕ	Single Phase
b_{hp}	Bias terms of hyperplane
$Al(OH)_3$	Aluminium Hydroxide
$AlSi_2O_5(OH)_4$	Kaolinite
Al_2O_3	Alumina dioxide
$BaTiO_3$	Barium Titanate
C - H	Carbon-hydrogen Bond
$CaCO_3$	Calcium Carbonate
C_Z	Class level of SVM
C_H	Hyperbola
CH_3	Methyl radical
$C(.)$	Cost function
$C(j)$	Closing Operation
C_1	High Voltage Side Capacitor
C_2	Low Voltage Side Capacitor
C_{pen}	Cost penalty factor of SVM
$\cos \theta_C$	Cosine value of contact angle
CO_2	Carbon dioxide
$D(j)$	Dilation Operator
D_j	Class variable set of GNB
$E(j)$	Erosion Operator
$ECM_{(\omega^f, \omega^s, \delta)} \Big _{\max}$	Maximum Energy Concentration Measurement
E_n	Entropy
F_1	Variance of D(j)
F_2	Variance of E(j)
F_3	Variance of O(j)
F_4	Variance of C(j)

F_5	Variance of δX_{DE} (j)
F_6	Variance of δX_{OC} (j)
F_7	Kurtosis of D(j)
F_8	Kurtosis of E(j)
F_9	Kurtosis of O(j)
F_{10}	Kurtosis of C(j)
F_{11}	Kurtosis of δX_{DE} (j)
F_{12}	Kurtosis of δX_{OC} (j)
F_{13}	Skewness of D(j)
F_{14}	Skewness of E(j)
F_{15}	Skewness of O(j)
F_{16}	Skewness of C(j)
F_{17}	Skewness of δX_{DE} (j)
F_{18}	Skewness of δX_{OC} (j)
F_{19}	Average of dilated signal $D_{avg}(j)$
F_{20}	Average of eroded signal $E_{avg}(j)$
$F-1$	Maximum value of magnitude spectrum $M_{m,l}$ of HS matrix
$F-2$	Mean value of the column corresponds to max value of magnitude spectrum $M_{m,l}$ of HS matrix
$F-3$	Power of the column corresponding to max value of magnitude spectrum $M_{m,l}$ of HS matrix
$F-4$	Standard Deviation of the column corresponding to max value of magnitude spectrum $M_{m,l}$ of HS matrix
$F-5$	Skewness of the column corresponding to max value of magnitude spectrum $M_{m,l}$ of HS matrix
$F-6$	Kurtosis of the column corresponding to max value of magnitude spectrum $M_{m,l}$ of HS matrix
$F-7$	Mean value of the row corresponds to max value of magnitude spectrum $M_{m,l}$ of HS matrix
$F-8$	Power of the row corresponding to max value of magnitude spectrum $M_{m,l}$ of HS matrix

<i>F-9</i>	Standard Deviation of the row corresponding to max value of magnitude spectrum $M_{m,l}$ of HS matrix
<i>F-10</i>	Skewness of the row corresponding to max value of magnitude spectrum $M_{m,l}$ of HS matrix
<i>F-11</i>	Kurtosis of the row corresponding to max value of magnitude spectrum $M_{m,l}$ of HS matrix
<i>F-12</i>	Mean value of the column corresponds to max value of phase spectrum $e^{\psi_{m,l}}$ of HS matrix
<i>F-13</i>	Power of the column corresponds to max value of phase spectrum $e^{\psi_{m,l}}$ of HS matrix
<i>F-14</i>	Standard Deviation of the column corresponds to max value of phase spectrum $e^{\psi_{m,l}}$ of HS matrix
<i>F-15</i>	Mean of the row corresponds to max value of phase spectrum $e^{\psi_{m,l}}$ of HS matrix
<i>F-16</i>	Power of the row corresponds to max value of phase spectrum $e^{\psi_{m,l}}$ of HS matrix
<i>F-17</i>	Standard Deviation of the row corresponds to max value of phase spectrum $e^{\psi_{m,l}}$ of HS matrix
<i>F_{as}</i>	Contact Angle between Air and Solid
<i>f_i</i>	Input feature variable
<i>f_s</i>	Sampling Frequency
<i>F_{sw}</i>	Contact Angle between Solid and Water
<i>F_{wa}</i>	Contact Angle between Water and Air
<i>h_p(x)</i>	Hyperplane of SVM process
<i>H_s(m,l)</i>	Hyperbolic window S-transform
<i>i_l</i>	Fundamental component of the surface leakage current
<i>I_{gn}</i>	Information Gain
<i>I_{max}</i>	Maximum Value of the Leakage Current
<i>i_n</i>	n^{th} order harmonic component of surface leakage current
<i>I_p</i>	Porcelain Leakage Current
<i>i_R</i>	SLC signal of the clean surface
<i>I_{SiR}</i>	SiR Leakage Current
<i>i_{SLC}</i>	SLC signal of the contaminated SiR insulator

$k\Omega$	Kilo Ohm
$M_{m,l}$	Hyperbolic stockwell (HS) matrix magnitude component
NO_x	Nitrogen oxides
N	Total number of samples
$NaCl$	Sodium Chloride
n_T	Datum number of training dataset
$^{\circ}C$	Degree Centigrade
$O(j)$	Opening Operation
O_2	Oxygen
$O-H$	Hydroxide
p	Factor that changes with solutions' temperature
$p(j)$	Input Signal
$s(k)$	Structure Element
S_a	Salinity of the coated layer
Si	Silicon
$Si - O$	Silicon-oxygen bond
$Si - O - Si$	Siloxanes
SiO_2	Silicon dioxide
SO_x	Sulfur oxides
$S_{p_{j\pm}}$	Number of the j^{th} sleep stage in the training subset
ST	Stockwell Transform
T_T	Training dataset for SVM
t	Constant value in equation 2.1
T^*	XHST complex 2D matrix
t_h	Threshold value
TiO_2	Titanium dioxide
TM	Trade Mark
T_s	Training Dataset
T_{S_i}	Subsets
$S_{p_{j\pm}}$	Number of the j^{th} sleep stage in the training subset
w_{AH}	Asymmetric hyperbolic window's FT
w_H	Hyperbolic window
w_{hp}	Weight Vector of hyperplane

x_T	Unlabeled testing dataset
x_z	Samples of training dataset
Y_z	Maximum probability function
Z_n	Atomic number
$Zn_3B_2O_6$	Zine Borate
ZnO	Zinc Oxide
β_H	Positive Curvature parameters
δ	Window shape controlling parameter
δ_p	Penetration depth
δ_S	Kernel function with gaussian form
$\delta X_{DE}(j)$	Dilation Erosion Difference
$\delta Y_{OC}(j)$	Opening Closing Difference
θ	Agle of incident
θ_{adv}	Advancing Contact Angle
θ_C	Contact Angle (degree)
θ_{rec}	Receiving Contact Angle
θ_S	Sliding Angle
θ_t	Ambient Temperature
λ	Wavelength
δ_p	Penetration depth
δ_S	Kernel function with gaussian form
λ_l	Coefficient of LASSO regularization
μ_{D_j}	Mean value of feature variable at each class level D_j
ξ^H	Translation Factor
$\rho(f_i D_j)$	Probability function of a feature characteristic f_i at each class level D_j
$\rho(D F)$	Probability of feature attribute's function
ρ_{si}	Density of the material
ρ_{SLC}	Shifted form of discrete Fourier Transform
σ	Gaussian window parameter
σ_{20}	Conductivity of the solution in ($\mu S/m$) at $20^\circ C$
σ_{θ_t}	Conductivity of the solution in ($\mu S/m$) at $\theta_t^\circ C$
ψ	Translational factor

ρ_{si}	Density of the material
ω^f	Forward taper parameter
ω^b	Back taper parameter
ζ_z	Slack Variable
σ_{D_j}	Standard Deviation at each class level D_j
$ST_{(\tau, f_a)}$	Stockwell transform function
$S_{SLC}(\sigma, f_s)$	Classical Stockwell Transformation
$p(t)$	Time Varying Signal
$ f_a $	Absolute sampling frequency
$g_w(t)$	Gaussian window function
$w_{sw}(\sigma - t, f_s)$	Gaussian Window function of Stockwell Transform
$g_w(t)$	Fixed-shaped Gaussian Window
τ	Translational parameter
$HST_{(\tau, f_a)}$	Hyperbolic Stockwell transform function
ρ_H^F	Front Tapper
ρ_H^B	Back Tapper
$M_{m,l}$	Hyperbolic stockwell (HS) matrix magnitude component
$e^{j\psi_{m,l}}$	Hyperbolic stockwell (HS) matrix phase component
$\varphi_s(x)$	Nonlinear mapping function
\mathbb{R}^{n_r}	Original data space
ξ^{lasso}	LASSO function
y_{t_i}	Marked value of i^{th} datum
f_{ij}	j^{th} property of i^{th} datum
ξ_j	Regression coefficient of j^{th} property
λ_l	Coefficient of LASSO regularization
f_s	Sampling Frequency
σ	Gaussian window parameter
C_H	Hyperbola
$XHST^{islc^k}(jR, \frac{n}{NR})$	XHST function

$\left[T^{*}(jR, \frac{n}{NR}) \right]^*$	Complex conjugate form of T-matrix for reference signal
$K_s(x_i, x_j)$	Kernel function with gaussian form
<i>2D</i>	Two Dimensional
<i>1D</i>	One Dimensional
<i>A</i>	Ampere
A_a	Surface area of the insulator's sample
<i>AC</i>	Alternating Current
<i>Al</i>	Aluminum
<i>AlN</i>	Aluminium Nitride
<i>ATH</i>	Alumina Trihydrate
<i>ATR</i>	Attenuated Total Internal Reflection
<i>AVR</i>	Automatic Voltage Regulator
<i>BN</i>	Boron Nitride
<i>BO</i>	Bayesian Optimization
<i>C</i>	Carbon
<i>CA</i>	Contact Angle
<i>CART algo</i>	Classification And Regression Tree algorithm
<i>CIGRE</i>	Conseil International des Grands Réseaux Electriques
<i>CL-1</i>	Contamination of Class: One
<i>CL-2</i>	Contamination of Class: Second
<i>CL-3</i>	Contamination of Class: Third
<i>CL-4</i>	Contamination of Class: Four
<i>CL-5</i>	Contamination of Class: Five
<i>CM</i>	Condition Monitoring
<i>cm</i>	Centimeter
<i>CNN</i>	Convolutional neural network
<i>Conv-1D</i>	1D convolutional layer
<i>COV</i>	Cross Over Voltage
<i>CPU</i>	Central Processing Unit
<i>CWT</i>	Continuous Wavelet Transform
<i>D</i>	Penetration depth
<i>DC</i>	Direct Current
<i>DDR4</i>	Double Data Rate Fourth Generation
<i>DIPUPES-MQ</i>	Ureido-modified MQ silicone resin

<i>DSO</i>	Digital Storage Oscilloscope
<i>EC</i>	Energy Concentration
<i>EDX</i>	Energy Dispersive X-Ray
<i>EH</i>	Extremely High
<i>EPDM</i>	Ethylene-Propylene-Diene Monomer
<i>ESCA</i>	Electron Spectroscopy for Chemical Analysis
<i>ESDD</i>	Equivalent Salt Deposit Density
<i>F</i>	Feature variable set of GNB
<i>FC layer</i>	Fully Connected layer
<i>FFT</i>	Fast Fourier Transform
<i>FN</i>	False Negative
<i>FOV</i>	Flashover Voltage
<i>FP</i>	False Positive
<i>FPR</i>	False Positive Rate
<i>FRP</i>	Fibre-reinforced Plastic
<i>FT</i>	Fourier Transforms
<i>FTIR</i>	Fourier-Transform Infrared Spectroscopy
<i>g</i>	Gram
<i>GB</i>	GigaByte
<i>GC</i>	Gas Chromatography
<i>GDT</i>	Gas Discharge Tube
<i>GHz</i>	Gigahertz
<i>GNB</i>	Gaussian Naïve Bayes
<i>GSO</i>	Grid Search Optimization
<i>H</i>	Frequency component of SLC signals
<i>Hz</i>	Hertz
<i>HCR</i>	High Compatible Rubber
<i>HS</i>	Hyperbolic Stockwell
<i>HST</i>	Hyperbolic window Stockwell transform
<i>HTV</i>	High Temperature Vulcanized rubber
<i>HTV_{1S1}</i>	Fresh Sample of High Temperature Vulcanized rubber
<i>HTV_{2S2}</i>	Aged Sample of High Temperature Vulcanized rubber
<i>HTV-SiR</i>	High Temperature Vulcanized Silicone Rubber
<i>HV</i>	High Voltage
<i>HVAC</i>	High Voltage Alternating Current
<i>HVDC</i>	High Voltage Direct Current

<i>IEC</i>	International Electrotechnical Commission
<i>IEC TR</i>	International Electrotechnical Commission Technical Report
<i>IPT</i>	Inclined-Plane Test
<i>IR</i>	Infrared
k_E	Euclidean distance in k-NN
<i>KCl</i>	Potassium Chloride
<i>keV</i>	Electron energy
<i>k-NN</i>	k-Nearest Neighbor
<i>kV</i>	Kilo Voltage
<i>kVA</i>	Kilo Volt Ampere
<i>kVrms</i>	RMS value of Kilo Voltage
<i>L</i>	Light
<i>LASSO</i>	Least Absolute Shrinkage and Selection Operator
<i>LC</i>	Leakage Current
<i>LIBS</i>	Laser-Induced Breakdown Spectroscopy
<i>LMW</i>	Low Molecular Weight
<i>LSR</i>	Liquid Silicone Rubber
<i>M</i>	Moderate
<i>mA</i>	Milliampere
<i>mg</i>	Milligram
<i>MHz</i>	Megahertz
<i>mm</i>	Millimeter
<i>MM</i>	Mathematical Morphology
<i>ms</i>	Millisecond
<i>NCF</i>	Nano-Fibrillated Cellulose
<i>NDT</i>	Non-destructive Testing
<i>nF</i>	Nano Farad
<i>NMR</i>	Nuclear Magnetic Resonance
<i>NSDD</i>	Non-Soluble Deposit Density
<i>OAA</i>	One Against All
<i>OMMT</i>	Organically Modified Montmorillonite
<i>p. u</i>	Per Unit
<i>PD</i>	Partial discharge
<i>PDMS</i>	Polydimethylsiloxane
<i>pF</i>	Pico Farad

<i>ph</i>	Phase
<i>QFOSF</i>	Quick-Flashover Salt Fog
<i>R</i>	Hyperbola function
<i>RAM</i>	Random-Access Memory
<i>RBF</i>	Radial Basis Function
<i>RC</i>	Resistance Capacitance
<i>ReLu</i>	Rectified Linear Unit
<i>RF</i>	Random Forest
<i>RFOCF</i>	Rapid-Flashover Clean Fog
<i>RH</i>	Relative Humidity
<i>RTV</i>	Room Temperature Vulcanized rubber
<i>s</i>	Second
<i>S</i>	Sample points of the SLC signals
<i>SCC</i>	Stress Corrosion Cracking
<i>SE_x</i>	Solvent Extraction
<i>SE</i>	Structure Element
<i>SEM</i>	Scanning Electron Microscopy
<i>SEM-EDX</i>	Scanning electron microscopy with energy dispersive X-ray spectroscopy
<i>SIMS</i>	Secondary Ion Mass Spectroscopy
<i>SiR</i>	Silicone Rubber
<i>SLC</i>	Surface Leakage Current
<i>SLM</i>	Solid Layer Method
<i>STFT</i>	Short Time Fourier Transform
<i>STRI-I</i>	Swedish Transmission Research Institute Index
<i>SVM</i>	Support Vector Machine
<i>T-F</i>	Time-Frequency
<i>TG</i>	Thermogravimetric
<i>THD</i>	Total Harmonics Distortion
<i>THz</i>	Terahertz
<i>TN</i>	True Negative
<i>TP</i>	True Positive
<i>USB</i>	Universal Serial Bus
<i>UV</i>	Ultraviolet
<i>V</i>	Volume of the solution

<i>VGGNet-16</i>	16-layer Visual Geometry Group Deep Convolutional Neural Network
<i>VL</i>	Very Light
<i>VR</i>	Voltage Regulator
<i>W</i>	Watt
<i>WT</i>	Wavelet Transforms
<i>XHST</i>	Cross-Hyperbolic Stockwell transform
<i>XLPE</i>	Cross Linked Polyethylene
<i>XPS</i>	X-Ray Photoelectron Spectroscopy
<i>XRD</i>	X-Ray Diffraction

Chapter 1

Condition Assessment of Overhead Line Insulators

1.1 Introduction

Overhead line conductors are employed on transmission and distribution power system networks. They have not been covered with any insulation coating. Insulators are therefore used to secure conductors to support structures. In addition, they ensure no leakage current flows from the insulator's surface to the earth. The cross arm and the live conductors are separated by insulators. Moreover, the insulators provide enough space between the wires and metal structures as well as proper insulation. The insulators must provide proper insulation and necessary clearance against high voltage in the most adverse atmospheric conditions to which the line will likely be subjected. The insulators also prevent short-circuiting between different phase conductors and provide essential mechanical support for line conductors [1] – [4]. When it comes to transmission and distribution of power networks, the insulator is unquestionably regarded as crucial and highly esteemed. In this regard, it is vital to select the appropriate components in order to ensure the smooth operation of overhead transmission and distribution systems. The key properties of an overhead line insulator are:

- The insulator possesses great strength in order to bear the load of conductors, wind, ice, and additional conductors resting upon it.
- The insulators have a high relative permittivity and high dielectric strength.
- It has a strong insulation resistance to prevent electricity from flowing into the ground.
- The rapture strength is much higher than the voltage to cause a flashover.
- The ability to handle drastic changes in temperature. In other words, it should not break when it gets very hot in the summer or very cold in the winter.

The dielectric strength should remain unaffected under different conditions of temperature and pressure [5]. The material used should not be porous and impervious to fluids as well as gases in the atmosphere. Moreover, it should be free of internal impurities, cracks, and other defects since these lower the dielectric strength. To ensure power system stability, overhead line insulators must be maintained on a regular schedule. Condition Monitoring (CM) techniques are used to investigate overhead line insulators' life span. CM techniques provide information about the condition of the insulators and can detect problems before they lead to stochastic failure. This can help to prevent outages and reduce maintenance costs. CM techniques also provide valuable data that can be used to improve the design of future insulators. In

Condition Assessment of Overhead Line Insulators

other words, condition monitoring refers to a method or process by which overhead line insulators are monitored in such a way that identifies the changes in their electrical characteristics. This can be used to assess overhead line insulators' longevity and predict maintenance needs before serious deterioration or breakdown occurs. As part of the CM process, data must be gathered for analysis, and identification the trends [5], [7]. A detailed discussion of various condition assessment techniques for overhead line insulators is illustrated in section 1.6.

1.2 Importance of Overhead Line Insulators

Power system network experiences different levels of voltage stress due to power transmission and distribution demands. Due to high electric field stresses, deterioration of insulation properties in power equipment can result in destructive failure of the entire electrical system [1] – [6]. Overhead line insulators play a crucial role in power systems by providing electrical insulation and mechanical support for transmission and distribution lines. These insulators are typically made of porcelain, glass, or composite polymer. Overhead power lines are designed to handle high-voltage stress and harsh environmental conditions. The main functions of overhead line insulators are:

- ***Electrical insulation:*** Insulators prevent electrical current flow through the transmission or distribution line to the ground. This helps to ensure that electrical power is efficiently transmitted and distributed to end-users without losses due to leakage or faults in circuits.
- ***Mechanical support:*** Insulators support the weight of power lines and other components such as conductors, fittings, and other metal parts of power lines. They also help maintain proper spacing between the conductors and prevent them from coming into contact with each other or the supporting structure.
- ***Protection against lightning:*** Overhead line insulators protect against lightning strikes. They can help provide a low-impedance path for lightning-induced electrical discharge to the ground. As a result, power lines and other components of the power system will not be damaged.
- ***Reduced power losses:*** Overhead line insulators reduce power losses by preventing electrical power leakage to the ground. This ensures maximum power is transmitted from the power source to the end user, improving efficiency.

In summary, overhead line insulators are integral to electricity transmission and distribution. They reduce interference with power flow, fire hazards, and ionization risks. The power system would have suffered from dangerous and costly problems without overhead line insulators.

1.3 Types of Overhead line insulators

Overhead line insulators play a crucial role in power system transmission and distribution networks [7] – [10]. In power networks, two types of insulators are used. These are mainly composite polymers and non-polymer insulators [10]. Insulators made from glass or porcelain are non-polymeric insulators. In contrast, composite polymer insulators (i.e., silicone Rubber (SiR)) are also utilized in power system networks. The following sections discuss various types of overhead line insulators in detail.

1.3.1 Silicone Rubber (SiR) Insulators

Silicone rubber (SiR) insulators are preferred for power grid transmission and distribution line applications. There are three main reasons why silicone rubber composite insulators are widely used in the power grid: first, they are light, easy to install, and their mechanical strength is no less than that of porcelain or glass insulators. Second, the manufacturing process is relatively simple. The shade configuration can be changed according to the mold to meet the requirements of different projects for creepage distance. Third and most importantly, when it comes to mitigating flashovers caused by pollution, silicone rubber composite insulators are superior to porcelain or glass insulators. Additionally, the silicone rubber composite insulator is capable of resisting the formation of the water film on its surface [1] – [3], [6] – [8].



Fig. 1.1 Image of Silicone Rubber (SiR) Insulators (i.e., 11 kV and 33 kV).

The performance advantages of SiR composite insulators are further enhanced when they apply power lines with voltage levels above 220 kV [5],

Condition Assessment of Overhead Line Insulators

[10] and railway-yard substations [11] – [13]. It has been found that healthy SiR insulators can work satisfactorily near about 8 to 20 years [7], [8], [10]. In Fig. 1.1, two different ratings of SiR insulators are shown (i.e., 11 kV and 33 kV).

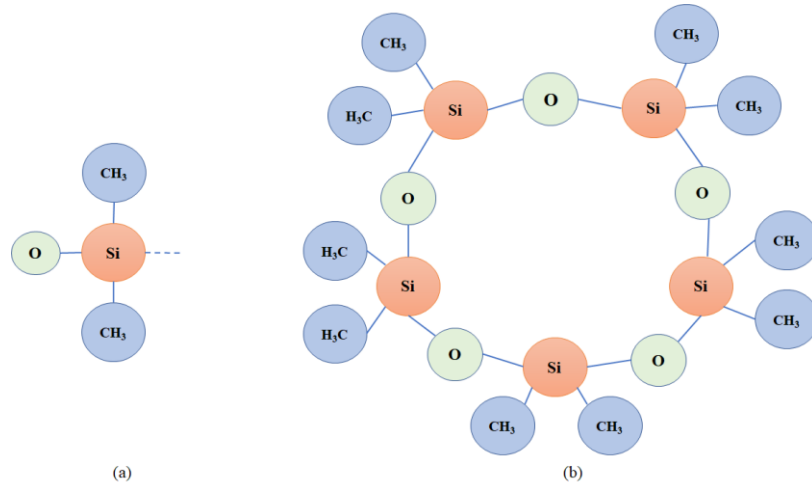


Fig. 1.2 Image of Chemical Construction of Polydimethylsiloxane (PDMS) (a) PDMS Solo unit monomer, (b) Cyclic PDMS molecule [13].

The type of material used in SiR is an elastomer. This elastomer is made of mainly silicon and oxygen atoms. According to the chemical structure, methyl groups are in the side chain (as shown in Fig. 1.2). SiR is colorless and it looks like oil or rubber type of substance. SiR is used in electrical insulation, heat insulators and medical science applications [2], [8]. SiR insulators have long-term reliable performance, but they are affected by electrical discharge, natural or artificial aging and environmental stresses [3], [6] – [8], [10].

The chemical composition of silicone elastomer or Silicone Rubber (SiR) is explained in detail in this section. Organic fillers (i.e., Organically Modified Montmorillonite (OMMT), nano-fibrillated cellulose (NCF) etc.) and inorganic fillers (i.e., Calcium Carbonate (CaCO₃), Silica, Zinc oxide (ZnO) etc.) are mainly used in SiR polymers [13]. These fillers provide the more rigid structure of SiR polymer through the vulcanization process [14], [15]. A fundamental form of SiR is made up of Polydimethylsiloxane (PDMS) with organic methyl groups of silicon-oxygen structure. The PDMS is expressed as $CH_3[Si(CH_3)_2O]_n Si(CH_3)_3$, where the letter n indicates the quantity of monomers [16]. The chemical structure of the single monomer unit (linear) and general ring structure of PDMS is shown in Fig. 1.2. Due to the Si - O bond in the SiR chemical structure, SiR insulators exhibit good thermal conductivity, hydrophobicity and anti-oxidant properties. The thermal stability range of the SiR insulators is from +180°C to -50°C. The reason for

having such a wide thermal range is due to the stable *Si - O* bond [8]. *Si - O* bonds are much stronger than conventional *C - O* and *C - H* bonds [7], [40]. In addition, *Si - O*'s bond energy is 8.3 eV. Chakraborty *et al.* reported that the base material in any SiR insulator is PDMS, where the primary molecular components are composed of carbon (50%), oxygen (25%) and silicon (25%) [5].

Table 1.1 Various types of filler elements and their characteristics [8].

Filler Elements	Effective Features
ATH	Increase the tracking and erosion resistance. Improve the thermal and electrical conductivity.
SiO ₂	Increase the ability to overcome erosion and tracking. Improve the thermal conductivity.
Al ₂ O ₃	Enhance the thermal conductivity. Increase the tracking and erosion resistance.
TiO ₂	The relative permittivity and the thermal stability increased.
ZnO	Improve the mechanical power and the thermal strength. Boost the relative permittivity.
CaCO ₃	Improve the hydrophobicity and the ability to hinder fires.
BaTiO ₃	Boost up the relative permittivity and the thermal constancy.
Carbon Black	Properties of the mechanical and electrical are improved.
Graphite	The thermal conductivity is boosted significantly.
Boron Nitride	Erosion get decreases and increases in tracking endurance.
Silicon Carbide	Increment of the tracking endurance and resistance to erosion is increased.

The mass of the cyclic molecule in SiR is 341. Methyl groups of the chemical structure of PDMS have the inherent quality of water repellence

Condition Assessment of Overhead Line Insulators

[16]. Two fundamental characteristics are viscosity and volatility, determined by the molecule chain's length [14], [16]. Because of crosslinking events on the chemical structures of the material, the outer surface of the aged SiR insulator becomes hard [17]. The study [18] said that the surface of the SiR insulator becomes rougher after continuous aging. The SiR insulator is enhanced in terms of electrical conductivity, mechanical strength, and temperature withstand capability by incorporating fillers. SiR primarily consists of pure Polydimethylsiloxane (PDMS), a substance known for its reduced intermolecular energy and limited mechanical strength [2], [7] – [8]. The Silica ($SiO_2 \cdot nH_2O$) [9], [19] or Alumina Trihydrate (ATH) ($Al_2O_3 \cdot 0.3H_2O$) [19] – [22], feldspar, Kaolin [23] and others substances, are commonly utilized as fillers of SiR insulators. Different types of filler elements and their advantages are summarized in Table 1.1. The SiR insulators contain four parts in their physical structure [12], [24] – [26]. These are: (1) two end fittings (metal), (2) FRP rod, (3) Silicone Rubber made of polymeric housing and (4) Edge between the FRP rod and SiR polymer housing (Shown in Fig. 1.3) [6]. The interface condition between the FRP rod and SiR polymer housing is the most vital factor in determining the insulator's longevity. The Steep forward impulse voltage and water diffusion test help to determine the volume and surface resistance at the interface of SiR polymers and FRP rods by the IEC 60093 standard [27]. Fig. 1.3 shows a cross-sectional view of the SiR insulator's physical structure. Also, the technical specification of the 11 kV and 33 kV outdoor SiR insulators is illustrated in Table 1.2 [28] – [29].

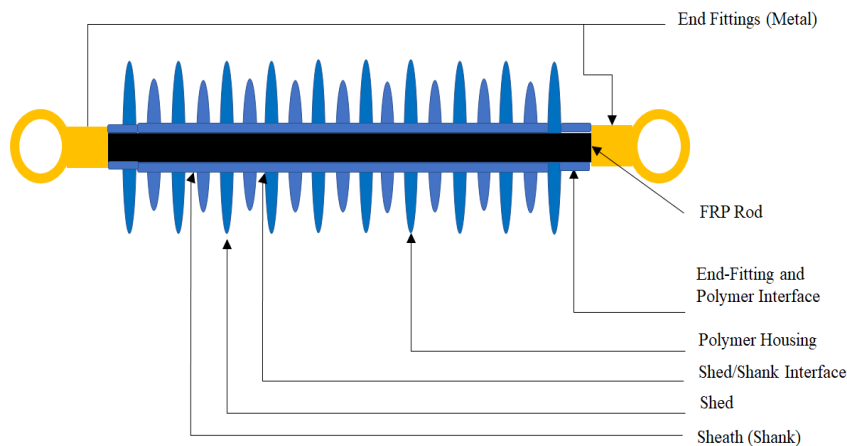


Fig. 1.3 Cross-sectional image of physical structure of Silicone Rubber (SiR) insulator [6], [24].

Table 1.2 Technical Specifications of 11 kV and 33 kV SiR insulators.

Technical Parameters	11 kV SiR Insulator	33 kV SiR Insulator
Housing Material	Silicone Rubber (SiR)	Silicone Rubber (SiR)
Rated Voltage	11 kV _{rms}	33 kV _{rms}
Total Creepage Distance	320 mm	900 mm
No of Disc	3	8
Disc Diameter	124 mm	124 mm
Sectional Length	250 mm	mm
Weight	730 g	1024 g

1.3.2 Non-Polymeric Insulators

Non-polymeric insulators are classified into two categories: porcelain insulators and glass insulators. Porcelain insulators are composed of ceramic material and a steel core, while glass insulators are composed of glass reinforced with fiberglass and a metal cap. Both insulators are designed to withstand harsh outdoor environments and ensure safe power transmission. All types of non-polymeric insulators are described in the following sections.

1.3.2.1 Porcelain Insulator

At controlled temperatures, the mixture of feldspar, kaolin, and quartz produces porcelain insulators by firing [30] – [34]. The porcelain insulator is stronger than glass, but not homogeneous, as each component shell is glazed during the manufacturing process. It does not allow too much leakage current to flow on its surface during operation. Moreover, porcelain insulators are not affected by changes in temperature and due to smooth surface, they do not get dirty easily [30] – [34]. However, it is difficult to find faults because they are not transparent. During mechanical stretching, porcelain is often not strong and cannot handle pulling forces higher than 5 kg/mm². The insulator can withstand a voltage of about 6.5 kV/mm of its thickness. In addition, it can handle a pressure of about 700 kg/mm² [30] – [34]. Normally it is difficult to manufacture homogeneous porcelain in the thickness required for some types of insulators and, therefore, for a particular operating voltage, a two or more-piece construction is adopted in which each piece is fired and glazed separately and then they are cemented together.

The mechanical qualities of this insulating material increase when it is produced at a lower temperature, but the material is still porous, so it may degrade after it is used. This material's porous is minimized when produced at a high temperature, but the substance becomes fragile. The porosity of this insulating material also reduces its dielectric strength. In addition, any impurities or bubbles left within the material result in a lower dielectric

Condition Assessment of Overhead Line Insulators

strength. Therefore, a compromise is made between the mechanical strength and the porosity of the material and a suitable temperature of the kiln is designed. The picture of a 11 kV porcelain insulator disc is show in Fig. 1.4.



Fig. 1.4 Picture of a 11 kV Porcelain Insulator Disc.

Porcelain insulators can withstand high thermal impact on its surface as it has high thermal resistance. This type of insulator can withstand high levels of compressive stress. Moreover, the porcelain insulator's surface is not easily degraded by environmental pollutants. Therefore, surface leakage current activity cannot be detected. In the electrical transmission and distribution network, porcelain insulators are preferred for on-load applications due to their aforesaid advantages. The major disadvantages of this type of non-polymeric insulator are that they are heavy, which adds additional weight to the overhead line system. However, they are vulnerable and for this reason, mishandling damages their surface. Apart from this, porcelain insulators have low tensile strength. The technical specification of the 11 kV porcelain insulators disc is illustrated in Table 1.3.

Table 1.3 Technical Specifications of 11 kV Porcelain Insulator Disc [34].

Technical Specifications	Parameters
Housing Material	Porcelain
Rated Voltage	11 kV _{rms}
Total Creepage Distance	338 mm
No of Disc	1
Disc Diameter	257 mm
Axial Height	145 mm
Weight	4298 g

1.3.2.2 Glass Insulator

With suitable toughening and annealing, glass has a higher resistivity and dielectric strength (i.e., 14 kV/mm of material thickness) than porcelain and is less expensive in simpler designs [35]. Porcelain cannot sustain the higher compressive forces than glass can, despite being a more uniform material. It has a smaller index of thermal expansion than other materials, which reduces stresses brought on by temperature fluctuations. Additionally, the material is translucent in nature, making it easy to see if there are any defects.



Fig. 1.5 Picture of a 11 kV Glass Insulator Disc.

Condition Assessment of Overhead Line Insulators

The glass Insulator's principal drawback is that moisture condenses more easily on its surface, making it easier for dust deposition as layers. This causes surface leakage current to flow [35]. Glass insulators, on the other hand, are effective up to 50 kV in a dirty and dry environment and up to 25 kV under normal atmospheric circumstances. The picture of the 11 kV glass insulator disc is shown in Fig. 1.5. Noticeably, the tensile strength of glass insulators varies from 5.34 kg/mm² to 8.35 kg/mm². Moreover, the breakdown strength varies from 70 kV/mm to 120 kV/mm, and the glass insulators' dielectric constant is nearly 6.8. The technical details about the 11kV glass insulator disc are illustrated in table 1.4.

Table 1.4 Technical Specifications of 11 kV Glass Insulator Disc [35].

Technical Specifications	Parameters
Housing Material	Glass
Rated Voltage	11 kV _{rms}
Total Creepage Distance	380 mm
No of Disc	1
Disc Diameter	420 mm
Axial Height	146 mm
Weight	7200 g

1.4 Factors for Degradation of Overhead Line Insulators

Overhead line insulators lose their insulation properties due to various factors. Overhead line insulators are mostly used in outdoor applications. That is why they are affected by various environmental factors at a greater rate. This includes extreme weather conditions, such as temperature fluctuations, humidity variation, rainfall, snow or ice deposition, and the deposition of dust. Apart from this, thermal, chemical, mechanical, electrical stresses and UV radiation also weaken the material's properties over time. As a result, regular maintenance and inspection are necessary to ensure insulators remain in an efficient working order. An elaborate discussion about overhead line insulator's degradation is presented in the following sections.

1.4.1 Effect of Environmental Factors

Environmental factors play an essential role in the deterioration of overhead line insulators. Outdoor insulators remain exposed to various climatic conditions. According to CIGRE Task Force 33.04.01, pollutants are classified based on four primary ecological circumstances [36]. These are desert, marine, agricultural and industrial environments. Under harsh environmental conditions, overhead line insulators degrade very quickly. Furthermore, they are susceptible to breakage due to heavy mechanical

shocks or lightning strikes. This is causing significant damage to the power supply network, leading to disruptions in economic growth and costly maintenance. To combat this issue, it is critical to use insulators with high hydrophobicity, chemical stability, and mechanical strength. In this regard, preventative maintenance strategies should also be employed to ensure these insulators' longevity. In Table 1.5, various types of environmental pollutants and their sources are illustrated. The following sections are discussed elaborately about the various types of environmental factors responsible for affecting overhead line insulators.

Table 1.5 Various types of Environmental Pollinating Sources for the Overhead Line Insulators [36].

SI. No.	Types of Pollutants	Source of Pollutants
1	Sea Salt	<ul style="list-style-type: none"> • Sea side areas. • Industries areas. • Roads side areas. • Hilly areas where salt get utilized for melting snow.
2	Cement	<ul style="list-style-type: none"> • Constructional areas. • Rock excavations areas. • Ploughed fields.
3	Fertilizer	<ul style="list-style-type: none"> • Plants for fertilising. • Recurrent utilization of fertilizers in agricultural fields.
4	Coal	<ul style="list-style-type: none"> • Coal mine areas. • Thermal power plant areas. • Brick Kilns areas / Coal burning.
5	Metallic	<ul style="list-style-type: none"> • Mining handling processes. • Mineral handling processes.
6	Volcanic Ash	<ul style="list-style-type: none"> • Areas where volcanic activity occur. • Ash handling areas.
7	Chemical	<ul style="list-style-type: none"> • Oil refineries, process industries areas where wide varieties of chemical are used. • Plants fertilising areas.
8	Smog	<ul style="list-style-type: none"> • From diesel engine emissions. • Railway crossing, yards and automobile at highways crossing areas.

1.4.1.1 Effect of Temperature

Temperature can affect overhead line insulators' performance and life expectancy, as high temperatures can accelerate degeneration. Therefore, it is worthwhile to consider temperature when selecting the type of insulator and designing the installation. As the temperature of the insulator rises, it will become less effective at conducting electricity. This can lead to increased arcing, which can cause the insulator to break down, resulting in power outages or other issues. The results show that the temperature changes the internal molecular configuration [37] – [38]. The permeability of temperature rise was more significant at the HV end because of the concentration of electric fields.

Which may lead to increased insulator polarization loss. A combination of strong field strength, high relative humidity, and quick temperature rise led to decay-like defects in composite insulators reported by Zhong *et al.* [37]. In addition, the biggest element influencing the environment's temperature, according to the research, is excessive relative humidity [38] – [39]. Notably, incremental temperature mostly affects the SiR insulators' surface and degrades the quality of the insulators. Consequently, dielectric losses increase in the presence of an alternating electric field, leading to SLC flow on the surface of the SiR insulator. For this reason, polarization loss appears in the molecular structure [38]. Rainfall, temperature, humidity, and other environmental factors also affect the performance of the overhead line insulator. At high environmental temperatures with a contaminated atmosphere, overhead insulators deteriorate faster and show low contamination flashover voltage under normal operating conditions. The reason is surface conductivity changes due to temperature rise and surface contamination. IEC 60507 [41] states that temperature change can alter solution conductivity, as detailed in Chapter 2 (section 2.3).

In [40], it was stated that the highest temperature value in thermal and dynamic testing for SiR insulators was $50^{\circ}\text{C} \pm 5^{\circ}\text{C}$. The temperature rise mostly affects the composite insulators' lower fittings, so the insulators lose their radial tension. It is important to note that the optimum operating temperature range at the end fittings of composite insulators as per CIGRE is 85°C to 100°C [40]. Under that range, composite insulators retain mechanical strength (i.e., radial stress). It has been reported by Bielecki *et al.* that when the fitting's temperature rises, an additional radial burden occurs in the compact region of the SiR insulator's glass-epoxy resin core [39]. Moreover, the operational durability of composite insulators might be impacted by this 20% increase in radial stress with respect to ambient temperature. Mizuno *et al.* reported that when the temperature goes down, the contamination flashover voltage increases [41]. On the other hand, when the pressure decreases, the contamination flashover voltage decreases. They also reported that pressure and temperature decrease at high altitudes. As a result, they predicted that the contamination flashover voltage would be 5% lower at 2000m altitude than at sea level [41]. Therefore, the atmospheric temperature

variation is one of the crucial characters to control the performance of overhead line insulators.

1.4.1.2 Effect of Moisture

Overhead Line insulators are exposed to various environmental conditions, including humidity. Humidity, or the existence of water particles in the atmosphere, can influence the surface degradation of these insulators in several ways.

- **Leakage Current:** High humidity can increase the leakage current along the surface of insulators. When moisture condenses on the insulator's surface, it forms a thin layer of conductive water film. This can lead to an increase in leakage current, which may result in partial discharges or corona activity [42] – [43].
- **Pollutant Deposition:** Humidity can facilitate the deposition of airborne pollutants on the insulator's surface. Moisture acts as a carrier for these contaminants, such as dust, salt, and industrial pollutants. The accumulation of these pollutants on the insulator's surface can lead to the formation of conductive paths, promoting surface degradation and eventually flashover events during electrical operation [38], [45].
- **Hydrophobicity Reduction:** Many insulators are designed with a hydrophobic (i.e., water-repellent) surface coating to maintain their insulating properties. High humidity levels can cause a reduction in the hydrophobicity of the coating, making the insulator more susceptible to moisture absorption and increased surface conductivity [43].

As a result of ambient humidity, composite insulators experience a temperature rise, making it difficult to screen the decay of composite insulators. The impact of change in humidity on temperature increase is essential for the study of investigation. Tu *et al.* mentioned that relative humidity (RH) increases the surface leakage current (SLC) flowing through the housing of the insulator which causes localized temperature rises on the surface of insulators [42]. Further, the dielectric loss of the insulating material of overhead line insulators contributes to local heating. It is noteworthy to mention that high RH along with high AC electric field intensity stimulates dielectric loss in overhead line insulators [44]. Yuan *et al.* reported a decay-like insulator generates heat when the humidity is high (i.e., 72% \pm 7% RH) or low (35% \pm 7% RH), thus generates heat under both conditions [38], [45]. It is noticeable that the moisture content of the overhead line insulator surface is different at various relative humidity. Consequently, there are variations in dielectric loss observed that are the primary source of local heating [46]. In this regard, rapid growth of the local heating may lead to the flashover event on the overhead line insulators [45]. Therefore, preventative maintenance is the most effective way to deal with this issue. Insulators should be regularly inspected for any signs of physical abnormality which may cause the breakdown of the insulators.

1.4.1.3 Effect of Rain falls

Rainfall is a key environmental factor impacting the performance and degradation of overhead line insulators. Overhead line insulators are typically made of glass, ceramic, or composite polymers. Their surface properties are essential for electrical insulation and preventing flashover events. The Effect of rainfalls on the surface degradation of Overhead Line Insulators are [47]:

- **Water Absorption:** Rain water can be absorbed by the surface of insulators, leading to increased surface conductivity. This can facilitate the formation of leakage currents and increase the likelihood of flashovers, particularly in polluted or contaminated environments.
- **Wetting and Drying Cycles:** During rainy periods, insulators can be subjected to wetting and drying cycles. These cycles can cause mechanical stresses on the insulator's surface. The reason of mechanical stress is due to thermal expansion and shrinkage, leading to micro-cracks or defects that could accelerate aging and degradation.
- **Pollution Deposition:** In regions with high levels of airborne pollutants, rain water can act as a solvent, washing the contaminants off the air and depositing them on the insulator surface. This pollution layer can form a conductive path, leading to partial discharge and flashovers.

On the other hand, heavy rainfalls may clean the insulator surface effectively. Jiang *et al.* reported in their research that mist, dew, fog, and light rain circumstances are ineffective for contaminated surfaces [46]. In addition, light rainy conditions caused surface leakage current (SLC) to flow rapidly, leading to flashover in overhead line insulators. They also reported that a period of five years was used to determine the amount of contamination accumulating on insulators. This was done based on climatological data, non-soluble deposit density (NSDD) and equivalent salt deposit density (ESDD) analysis. Notably, in dry seasons (i.e., January – April), contamination accumulates, while in wet seasons (i.e., June – October), contamination is washed off. In [47], it was reported that value of NSDD changed slower with increasing rainfall intensity because NSDD solely depends on non-dissolved contamination. Alternatively, the estimation of ESDD uniquely depends on soluble pollutants and does not change with rainfall duration. Therefore, rainfall plays a major role in the contamination of the surface of overhead line insulators.

1.4.1.4 Effect of Salt and Dust

Salt and dust can significantly affect overhead line insulators, especially in outdoor environments. As stated above environmental contaminants can lead to changes in the surface properties of the insulators, impacting their electrical characteristics.

Effect of Salt: Salt deposition on overhead line insulators can occur in coastal regions or areas with marine aerosols [48], [49]. When salt accumulates on insulator surfaces, it attracts moisture from the atmosphere and forms a conductive layer. This conductive layer can create a path for leakage currents to flow. In addition, localized partial discharge appears which can reduce the electrical resistance of the insulator and compromise its ability to withstand voltage stress, potentially leading to flashovers and power interruptions [48]. Sharma *et al.* investigated the impact of salt contamination on outdoor polymer insulators using artificial pollution tests. Moreover, the authors stated that the deposited salt contamination evaluated the performance of overhead line insulators under various voltage and weather conditions [49]. Notably, when the insulator becomes coated with salt, it can lead to "salt-fog tracking" [50]. This occurs especially during periods of high humidity or fog and when the salt layer absorbs moisture from the air and forms a conductive path for allowing current leakage across the insulator surface. Salt-fog tracking can eventually lead to flashovers, where arcs through the air between the insulator and the conductor, causing a temporary short circuit [50], [51].

Effect of Dust: Dust accumulation on overhead line insulators is common in arid and dusty environments. Dust particles deposition on the insulator surface can create a layer to reduce surface resistance. This layer can facilitate the formation of a conductive path between the line conductor and the ground, leading to leakage currents and partial discharges. As a result, the insulator's dielectric strength may be compromised, and the risk of breakdown increases. Moreover, dust can deposit on the insulator surface, forming a layer that reduces surface hydrophobicity. As a result, the insulator may be less effective in repelling water, which leaves it prone to surface contamination by pollutants. Similar to the salt-fog tracking effect, the dust layer may develop a conductive track for SLC when paired with water particles [52]. Additionally, dust accumulation can reduce flashover voltage, leading to electrical failures. Notably, particle size distribution features are substantially influenced by air velocity, relative humidity, and the charge deposited on insulators' housing [53]. All three factors have a significant influence on particle size distribution characteristics, including relative humidity, air velocity, and charges accumulated on the surface [54]. In contrast, the difference in particle bonding concentrations mostly reflects the impact of electric field distribution [54] – [55].

In conclusion, both salt and dust can affect overhead line insulators' performance. Proper maintenance, natural and artificial cleaning, condition assessment techniques and selection of appropriate insulator materials are essential to mitigate the impact of these environmental factors and ensure the reliable operation of power transmission and distribution systems.

1.4.2 Effect of Thermal Stress

Thermal stresses have several potential sources. Thermal strains can be caused in overhead line insulators by lightning strikes, short circuits, forest fires and overloads [56]. The aforementioned factors might have a substantial impact on the insulation's effectiveness. It is significant to mention that polymeric insulators can be deteriorated mechanically and chemically by thermochemical strains. Most thermal strains are caused by a combination of electrical and environmental factors. Corona, dry band arcing, partial discharge and UV radiation are influential factors resulting in overhead line insulator thermochemical degradation. Thermochemical depolymerization occurs more frequently in polymeric insulators than in non-polymeric insulators [3], [56].

1.4.3 Effect of Electrical Stress

Overhead line insulators are experienced typically two types of electrical stress on them. The overvoltage brought on by various electrical loading effects, which can result in flashovers, is referred to as power frequency electrical stresses [57]. Power frequency electrical stresses refer to continuous electrical stresses on an insulator that can resist such stresses. Impulse stresses can be attributed to lightning and switching effects on electrical systems. Energized overhead line conductors pose a large electric field in their circumference, which causes electrical stress in overhead line insulators [58]. As the voltage increases, the electric field strength around the conductor and insulator surface also increases, leading to higher electrical stress on the insulator.

Electrical stress on overhead line insulators can be influenced by the following factors such as [57] – [58]:

- Voltage level: Higher voltages result in higher electrical stress on the insulator.
- Insulator design and material: Different insulator designs and materials have varying resistance to electrical stress.
- Contamination: Contaminants like dust, dirt, salt, or pollution can alter the electrical properties of the insulator surface, affecting electrical stress.
- Line geometry: The configuration of the overhead lines and the arrangement of insulators can impact the distribution of electrical stress.
- Weather conditions: Humidity and temperature can affect the electrical properties of the insulator material and influence electrical stress.
- Electrical loading: Electrical stress may vary with the load on the power line.

1.4.4 Effect of Mechanical Stress

Mechanical stresses can result from factors such as wind direction, ice deposition, snowfalls, vibrations, sagging and even occasional physical impacts [58]. Wind flow may produce downward, horizontal, and vertical stresses on the conductor's catenary in the case of overhead lines [58]. The conductor's weight in the vertical position is increased by the load.

The combination of solar radiation and environmental temperature during warm weather may increase the insulator's temperature [58] - [59]. Notably, temperature increases cause the majority of insulators to deteriorate their mechanical durability. In addition, high wind conditions linked to maximum electrical loads cannot cause temperatures to rise [59]. Some of the common mechanical stresses that affect overhead line insulators include [59]:

- **Vibration:** Vibrations caused by wind, conductor movement, or nearby machinery can lead to fatigue and wear of the insulator material.
- **Tension and Compression:** The insulator experiences tension and compression force due to the weight of the conductor and the conductors' sag.
- **Ice and Snow Loading:** Accumulation of ice and snow on the insulators can increase their weight and introduce additional mechanical stress.
- **Aeolian Vibrations:** These are wind-induced vibrations that can cause significant stress on the insulators.
- **Dynamic Loads:** Sudden changes in mechanical loads, such as those caused by short circuits or line faults, can impact the insulators.

The degradation of insulators due to mechanical stress can result in a variety of failure modes, such as cracks, fractures, surface erosion, and reduced electrical performance. Prolonged exposure to mechanical stress can weaken the insulator's structural integrity, increasing the risk of catastrophic failures and power outages [58] – [59].

1.4.5 Effect of Chemical Reaction

Outdoor insulators are crucial elements of electrical power networks that prevent current leakage and ensure safe and efficient power transmission. These insulators are typically made of porcelain, glass, or composite polymers. However, they are exposed to various environmental conditions, including air pollution and chemical pollutants. These conditions can lead to chemical reactions on their surfaces and affect their performance. It is worthwhile to mention that a chemical pollution layer is formed on the insulator surface by the wind [60] – [61]. This pollution layer becomes conducting when water molecules from the atmosphere come into the vicinity of the insulators surface [60]. Then, surface leakage current (SLC) starts flowing through these layers day by day, and as a consequence, a flashover event appears on overhead line insulators [60].

Condition Assessment of Overhead Line Insulators

The effects of chemical reactions on overhead line insulators can be summarized as follows [62]:

- **Surface Contamination** [62] – [63]: Chemical pollutants, such as sulfur oxides (SO_x), nitrogen oxides (NO_x), and other acidic gases present in the atmosphere due to industrial emissions and vehicle exhaust, can deposit on the surface of insulators. These contaminants can form a layer of pollution on the insulator's surface, leading to reduced electrical performance. The detailed explanation is addressed in (section 1.6.2.1.2).
- **Hydrophobicity Reduction** [63]: Surface contamination can reduce the hydrophobicity of insulators. Hydrophobicity is the property that allows the insulator to repel water. When hydrophobicity is reduced, water can form a non-discrete path on the circumference of insulator, which increases localized electrical discharges and flashovers during rainy or humid conditions. An elaborate explanation is demonstrated in (section 1.6.2.1.1)
- **Corrosion** [61]: Chemical reactions between the insulator's material and environmental pollutants can lead to corrosion of the surface. Corrosion can weaken the insulator's structure and compromise its electrical insulation properties. The detailed explanation is addressed in (section 1.6.2.1.2).
- **Tracking and Erosion**: Chemical reactions on the insulator's surface can create conductive paths for leakage currents, known as "tracking." Tracking can lead to erosion of the insulator's surface and eventually result in electrical failure. The detailed explanation is addressed in (section 1.6.2.3.4).

Notably, over time, the cumulative effects of chemical reactions can cause a gradual degradation of the insulator's electrical performance, increasing the risk of power outages and compromising the reliability of the power transmission system.

1.4.6 Effect of Aging

The effects of aging on the insulation's performance are a crucial aspect. Prolonged aging can degrade insulator conditions, leading to overhead line insulator failure. It is noteworthy to mention that the effect of aging on polymeric insulators is much greater than that of non-polymeric insulators. Ageing is categorized into two categories: thermal aging and ultraviolet (UV) aging. A detailed discussion of the various types of aging is presented in the following sections.

1.4.6.1 Effect of Thermal Aging

Thermal aging refers to the process by which materials are exposed to elevated temperatures for an extended period. In the case of overhead line

insulators, they are often subjected to varying temperature conditions due to weather fluctuations. Over time, thermal aging can lead to physical and chemical changes in the material, potentially affecting its mechanical properties and electrical performance. Thermal aging refers to materials deteriorating due to elevated temperatures. In the case of overhead line insulators, usually made of polymeric materials, thermal aging can cause several adverse effects. These effects include mechanical properties [8], hydrophobicity properties [64], tracking and erosion [26], [65] of overhead line insulators' surface.

In [65], it was reported artificial thermal degradation experiments were performed on HTV silicone rubber (SiR) shed sample insulators to examine thermal deterioration properties. In addition, the aged HTV insulator samples were subjected to examine the status of physical degradation, which was investigated by following techniques such as FTIR processes, thermogravimetric (TG) analysis, and scanning electron microscopy (SEM) methods. In the first stage of the pyrolysis process, $Al(OH)_3$ flame retardant is dehydrated and decomposed, followed by polydimethylsiloxane (PDMS) molecule decomposition [65]. Gradually, crack size and number increase on sample surfaces as thermal aging time increases. Moreover, the thermally aged HTV SiR insulators accelerate the aging process significantly because the internal molecular bonding structure, such as, $Si - O - Si$ main chain, $Si - C$ side chain, and $O-H$ group, absorbed the peaks of UV rays.

1.4.6.2 Effect of Ultraviolet (UV) Aging

The term Ultraviolet (UV) Aging refers to the degradation of materials caused by prolonged exposure to UV radiation from the sunlight. For overhead line insulators installed outdoors, UV exposure is inevitable, and it can lead to surface degradation and changes in the insulator's material properties. Effects of UV aging on overhead line insulators: UV aging refers to the degradation of materials caused by prolonged exposure to ultraviolet (UV) radiation. For overhead line insulators, which are often installed outdoors, exposure to UV radiation can cause:

- **Polymer Degradation:** UV radiation breaks down the polymer material's molecular structure, decreasing its mechanical properties and durability.
- **Surface Degradation:** UV aging can cause surface cracks, oxidation, and erosion, leading to a reduction in the insulator's hydrophobicity and an increased risk of tracking and surface wetting.
- **Color Fading:** Many polymeric insulators have color additives to protect against UV radiation. However, prolonged exposure to UV rays can cause these colors to fade, indicating potential degradation.

Qiao *et al.* discovered that UV radiation can cause damage to the silicone rubber by breaking down its methyl side chain, which makes the material surface age [67]. As part of their research, they also investigated how oxygen

Condition Assessment of Overhead Line Insulators

in the atmosphere reacts with reactive compounds to yield hydrophilic $-OH$ particles and produce methane gases [67]. In addition, silicone rubber may degrade chemically due to acidic and alkaline conditions, as well as nitrogen oxides (NO_x). After absorbing moisture, NO_x is converted into nitric acid. The acid substance causes the $Si-O$ bonds in silicone rubber to break, turning them into $Si-OH$ bonds. The performance of silicone rubber composite insulators can be influenced by sunny weather and high electric fields [66] – [67]. Hedir *et al.* mentioned that Silicone rubber's performance is significantly affected by UV aging for prolonged exposure under various environmental conditions, which causes physical and chemical degradation [66].

1.5 Parameters to Determine the Condition of Overhead Line Insulators

Pollution severity is a widely used parameter to quantify contamination levels of overhead line insulators. It considers the type and quantity of contamination present on the insulator surface. There are various parameters to assess contamination levels, including: Equivalent Salt Deposit Density (ESDD), Non-soluble Salt Deposit Density (NSDD), Flashover Voltage (FOV), Puncture Voltage and Surface Leakage Current (SLC). An elaborate discussion of the parameters is discussed in the following sections.

1.5.1 Equivalent Salt Deposit Density (ESDD)

An effective way to monitor insulator pollution levels is Equivalent Salt Deposit Density (ESDD) [68]. In order to determine ESDD, it is necessary to estimate the equivalent quantities of NaCl deposited over the surface area of an insulator. In accordance with IEC 60507, the conductivity of the salt deposited has been determined [68]. Moreover, the measuring unit of ESDD is mg/cm^2 . The process of the ESDD method requires collecting pollutants from the surface of the insulator and mixing them in a specific volume of water to calculate the conductivity of the solutions at room temperature [68]. The elaborate discussion along with the mathematical expression of ESDD has been discussed in Chapter 2 (section 2.3).

1.5.2 Non-soluble Salt Deposit Density (NSDD)

It is another effective technique to evaluate contamination levels of insulators. The NSDD describes the amount of inert, non-soluble contaminants deposited on the surfaces of the insulators on a unit area [68, 69]. The calculation of NSDD is generally conducted similarly to ESDD measurement [68]. Maraaba *et al.* reported that the process of estimated amounts of non-soluble contaminants among the $NaCl$, KCl and Kaolin was present on the surface of overhead line insulators [69].

1.5.3 Electrical Parameters

To determining the surface contamination levels of overhead line insulators there are basic three electrical parameters are responsible to estimate the surface condition of the overhead line insulators. These parameters are flashover voltage, puncture voltage and surface leakage current (SLC). In the following sections, an elaborate discussion has been reported about electrical parameters.

1.5.3.1 Flashover Voltage

In essence, flashover occurs when electricity discharges over an insulator's surface [34]. Additionally, the air insulation around the insulator surface breaks down during flashover. The flashover voltage depends on several factors, including the type and material of the insulator. It also depends on the distance between conductive surfaces, humidity, temperature, and atmospheric pressure. It is designed to withstand specific flashover voltages to prevent damage and maintain surrounding environment safety.

1.5.3.2 Puncture Voltage

Puncture voltage typically refers to the voltage at which an insulating material breaks down and allows current to flow through it, resulting in electrical breakdown. When the voltage across an insulator reaches puncture voltage, it exceeds the material's dielectric strength. This causes it to lose its insulation properties and become conductive [70] – [71]. Consequently, the insulators become permanently damaged in this situation. It is noteworthy that insulator flashover voltage is lesser than puncture voltage [70] – [71]. Moreover, it is a critical parameter in determining the maximum voltage which insulators can withstand before failing and potentially causing electrical faults or hazards.

1.5.3.3 Surface Leakage Current (SLC)

It has been observed that the surface leakage current (SLC) of overhead line insulators flows under humid environmental conditions from the surface of the insulator towards the ground [60]. It is noteworthy to mention that the ground should be referred to as zero potential [60]. Moreover, the prolonged flow of surface leakage current (SLC) degrades the insulator's surface properties which can lead to a complete breakdown of power flow [60]. Therefore, it is imperative to monitor the surface leakage current of overhead line insulators to determine their condition. An elaborate discussion is reported in Chapter 1 (section 1.6.2.3.1).

In [57], Khattak *et al.* reported that two types of external causes (such as environmental and electrical factors) are responsible for the overall deterioration of SiR insulators. The different types of stresses and their overall effect on SiR insulators are summarized in Table 1.6.

Condition Assessment of Overhead Line Insulators

Table 1.6 Summary of various external factors and their effects on SiR Insulators [57].

Types of External Factors	Reasons for degradation of SiR Insulators	Effects on SiR		
		Molecular structure	Insulators	Change in Properties
Environmental Stresses	UV Radiation, Acid Rain, Temperature, Humidity, Snowfall, fog, Salt precipitation, dust particles accumulation, Wind flow, and ozone effects.	Depolymerization	Damage of flexibility	Degradation of Mechanical and Electrical properties
	Algae, Fungi, Micro-biological Pollutants	Loss of Low Molecular Weight (LMW), Depolymerization	Erosion increases, surface roughness, loss of elasticity, surface and volume cracking	Degradation of Mechanical and Electrical properties
Electrical Stresses	Partial Discharge, Corona, Leakage Current (LC), Dry Band Arcing, FOV	Loss of Low Molecular Weight (LMW),	Degradation of hydrophobicity property	Degradation of Electrical properties

1.6 Condition Assessment Techniques of Overhead Line Insulators

Any defects or surface deterioration may appear in any type of insulator after an extended period of service. This may ultimately threaten the stability of the power system. Overhead line insulators faults and degradation events are classified based on where defects occur. Three different analysis processes

are used to assess the degradation of overhead line insulators. Condition monitoring of overhead line insulators is the most effective way to deal with surface condition investigation of overhead line insulators. These are physical properties analysis, chemical analysis and electrical analysis [2, 8]. An elaborate study of the aforesaid events has been given in [72]. Notably, the impact of surface degradation due aforesaid factors has been observed predominantly on polymeric insulators rather than non-polymeric insulators.

1.6.1 Importance of Condition Assessment Techniques of Overhead Line Insulators

It has already been mentioned that surface deterioration increases the likelihood of insulator failures. Power lines transmit electricity over long distances and are supported by an insulator framework. Consequently, the insulators are situated in various geographical regions, each with distinct environmental conditions suitable for their operation. This can lead to various stress levels imposed on different line insulators by the environment, consequently affecting the likelihood of failure in each case. As a result, up to 70% of all line outages can be attributed to insulator failure [73]. All the insulators in the same location of the same transmission tower perform differently. Their performance may vary depending on the condition of their surfaces. If an insulator in any tower fails, the entire system will be shut down. The idea is to divide the transmission line into smaller parts to avoid power cuts caused by environmental, electrical and mechanical stresses. The power grid's reliability is at risk if any overhead line insulators fail. In this regard, it is essential to perform condition assessments of overhead line insulators in each section of transmission and distribution lines. Therefore, assessing the overhead line insulators' condition is extremely worthwhile.

Environmental or atmospheric conditions like humidity and temperature deeply impact overhead line insulators. Environmental conditions vary from country to country. Because of changing atmospheric conditions, the analysis of surface leakage current for a particular insulator can vary from location to location. So, there must be some techniques that can establish a relationship between surface contamination levels of overhead line insulators and any changes in the environment. In this regard, modern research is addressed with the help of Artificial Intelligence-based classifiers which are extremely useful for forecasting insulators' condition assessment [29], [73] – [75].

1.6.2 Types of Condition Assessment Techniques of Overhead Line Insulators

As mentioned previously, it is necessary to regularly assess the condition of overhead line insulators to ensure the system's safety and performance. Condition assessment of overhead line insulators is classified into three categories. The following sections discuss the three categories of condition assessment techniques in detail.

1.6.2.1 Analysis of Physical Properties

After exposure to the aforesaid factors, the physical properties of overhead line insulators can be investigated using (i) hydrophobicity and (ii) accumulation of pollutants on the insulator surface.

1.6.2.1.1 Hydrophobicity

Hydrophobicity is a physical characteristic of overhead line insulator's chemical structure. In comparison with non-polymeric insulators, SiR molecules inhibit water film formation on its surface because of their hydrophobic properties. As a result, the SiR insulators create water droplets on the surface instead of forming a continuous water film. This signature characteristic is called Water Repellence [2], [8], [10]. On the contrary, water molecules attract hydrophilic molecules [2]. Composite polymeric insulators like SiR are made of low hydrophilic properties-based materials; That is why they show superior performance. Moreover, SiR insulators can recover their lost hydrophobicity even after the aging event due to their durable material structure. The following factors such as hydrophobicity, carbonization, effects of arcing on insulator sheds, insulator design, penetration of the water molecule in the FRP rod, tracking and erosion resistance of SiR insulators assist to predict the longevity of performance. It is noteworthy that the most dangerous agent is water molecules that initially enter the SiR housing and then the FRP rod. After the molecules of water penetrate in FRP rod, the temperature rise, localized discharge and then arcing phenomena are started. Ultimately, this degrades the interface resistance between the FRP rod and the SiR housing and cause punctures of the insulators. It was reported in [72] that the brittle and decay-like fractures have all occurred due to interface failure and poor adhesive application between the FRP rod and SiR housing. In [76], it is reported that in 500 kV transmission line insulators, after the water enters the core of the composite insulators, either nitric acid is formed due to the surface discharge phenomenon or sulfuric acid is generated due to acid rain. This acidic reaction ultimately leads to Stress Corrosion Cracking (SCC) in the FRP rod. It is also reported that the SCC is formed due to three main factors: humidity, the impact of the electric field, and surface contamination of the SiR insulator's housing.

Hydrophobicity is determined by measuring the contact angle of deposited water droplets on the surface of the insulator. Four methods are used to calculate hydrophobicity. These are the contact angle (CA) measurements [49], sliding angle measurement [76], Swedish Transmission Research Institute Index (STRI-I) [76] and water-soaked test [77] – [78]. The static and dynamic contact angle measurement [8], [79] is the most popular technique for estimating hydrophobicity. Ethylene iodide or distilled water is applied to the surface of the SiR insulator to measure the contact angle [76], [80].

Static Contact Angle

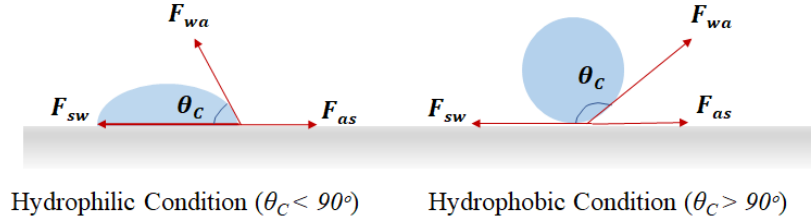


Fig. 1.6 A schematic representation of Contact Angle (CA) (a) Static Contact Angle, (b) Dynamic Contact Angle [80].

The contact angle (θ_C) depends on the three interfacial force factors. These interfacial forces exist between water and air (F_{wa}), solid and water (F_{sw}), air and solid (F_{as}) (i.e., shown in Fig. 1.6 (a) and 1.6 (b)). These three interfacial forces are represented by Young Dupre's mathematical expression [8]:

$$F_{as} = F_{sw} + F_{wa} \cos \theta_C \quad (1.1)$$

The contact angle (static) is measured with the assistance of the goniometer, magnifying instrument, or computerized photography [2], [8]. The static-contact angle measurement schematic representation is shown in Fig. 1.6 (a). Hydrophobicity is the dynamic property of any material. Therefore, the dynamic contact angle measurement is essential, but the procedure is more complex than the measurement of static-contact angle. The dynamic contact angle is measured either by advancing the slope (i.e., increasing the water droplet mass) or using a receding slope (i.e., decreasing the water drop volume). The schematic of the dynamic contact angle is shown in Fig. 1.6 (b).

If a water drop is placed on the slope of the polymeric material, then the advancing angle (θ_{adv}) is formed at its bottom. Similarly, a receding angle (θ_{rec}) is formed at the upper side. These two angles are essential for quantifying dynamic contact angles. A logarithmic relationship is found between the recovery time and the receding angle [79]. In [81], it has been reported that SiR insulators can be considered an excellent dielectric strength with good aging resistance if the value of the contact angle (CA) is close to 110° after hydrophobicity testing. The slope creates a sliding angle (θ_s) with the horizontal axis (as shown in Fig. 1.6 (b)) and its measurement is essential to determine hydrophobicity. As reported in [80], the sliding angle is directly proportional to the surface wetness. The measurement of contact angle is affected by various factors. These are droplet size, water droplets addition or subtraction rate, the interval between the tests and slope angle range [80]. The authors suggest that measurements should be made frequently and average results should be considered to achieve good precision. For testing, the droplet

Condition Assessment of Overhead Line Insulators

volume range should be from 5 μl to 150 μl [2]. The hydrophobicity of SiR insulators is inversely proportional to the soluble electrolytes of the contaminant surface. The contact angle (i.e., static or dynamic) measurement is more effective than other conventional methods such as Electron Spectroscopy for Chemical Analysis (ESCA) and the examination of Cross Over Voltage (COV) [81].

It has been reported in [79] that prolonged artificial UV aging reduces the hydrophobicity of SiR insulators and can lead to quick flashover. The surface accumulated water molecules get blocked by resistance at the interface between the FRP rod and the SiR insulator housing. The impact of prolonged aging can degrade the interfacial resistance between the SiR insulator housing and the FRP rod. Consequently, the hydrophilic (i.e., *-OH*) group appears on the surface of HTV-SiR insulators and reduces the hydrophobic condition [76] – [82]. This article reports a relationship among the four parameters: angle of contact, surface condition of the insulator, surface contamination and pollutants accumulations degree (ESDD). The relationship among the above parameters is presented in Table 1.7.

Table 1.7 Relationship among the Contact Angle, surface condition of the insulator, physical condition of the insulator and contamination level (ESDD).

Contact Angle	Physical Condition	Insulator's Surface Condition	Contamination Level (ESDD)
$\theta_c \geq 90^\circ$	Hydrophobic Condition	Less rough surface	Very Light or Light
$\theta_c < 90^\circ$	Hydrophilic Condition	Roughness increases	Heavy or Medium

1.6.2.1.2 Accumulation of Pollutants on the Insulators Surface

Environmental pollutants are the leading cause of corrosion of overhead line insulator surfaces. These contaminants come from a variety of sources. For example, salt is a polluting factor found in coastal and industrial areas. Similarly, manure, coal, and smog come from the fertilizer industry, harvesting fields, coal mills and automobile emissions. According to the literatures, high relative humidity, rising temperatures, accumulation of hydroxide ions on the surface, acid rain and thermal aging reduce SiR insulators' life than porcelain and glass insulators [83] – [84]. In addition, according to the reported works [84] – [85], aforesaid contaminants introduced the dry band arcing on the surface of SiR insulators. Subsequently, they can cause a complete flashover of SiR insulators in the worst environmental conditions [83] – [84].

In the coastal area, the soluble salts are mainly *NaCl* and *Na₂SO₄*. These salts are deposited on the insulator's surface and make a persistent conductive

path with the assistance of water molecules. Surface Leakage current (SLC) flows through this conductive path to the surface of the insulator. Finally, the constant flow of LC leads to the complete breakdown of the SiR insulators [85]. In addition, the degradation of the SiR insulators is similar in the tropical rainforest continents [85]. In the tropical rainforest areas, the pollutant is primarily Kaolinite ($AlSi_2O_5(OH)_4$) [85]. The performance of SiR insulators in desert areas has been analyzed under frequent sandstorms and temperature fluctuations [84], [86]. The authors have reported in their work [86] that due to an electric field, sand particles become charged and begin to discharge on the surface of SiR insulators. RTV-SiR and HTV-SiR insulators work well in coastal areas but also degrade due to high contamination [84]. The Equivalent Salt Deposit Density (ESDD) scheme [86] determines the contamination based on the average concentration of dissolved salt. The Non-Soluble Deposit Density (NSDD) [85] – [86] is another parameter for measuring surface contamination. As per the recent study, the SiR insulator surface contamination can be classified into five categories using ESDD values. The classification of contamination levels is shown in Table 1.8.

Table 1.8 A description of the different categories of contamination classes [85].

Types of Pollution	Sodium Chloride ($NaCl$) (gm)	Kaolin [$AlSi_2O_5(OH)_4$] (gm)	Distilled water (ml)	ESDD (mg/cm^2)
Very Light	0.05	15	20	0.0562
Light	0.25	15	20	0.1133
Moderate	0.41	15	20	0.1795
High	0.90	15	20	0.3733
Very High	1.70	15	20	0.6277

The procedure for preparing artificial contaminants in the laboratory is described below. According to IEC-60507, the slurry is prepared by mixing Kaolin, sodium chloride and distilled water for research [85]. The slurry of this artificial contaminant is applied as a layer on the insulating surface and dried for 24 hours. Thereafter, the intensity of the contamination is determined by the amount of salt available in the slurry. Table 1.9 shows changes in salinity levels and ESDD values of SiR insulators before and after UV aging [87]. The effect of contaminants on the surface of a SiR insulator depends on where the insulator is installed.

Condition Assessment of Overhead Line Insulators

Table 1.9 Pollution parameters before and after UV aging of SiR insulators [87].

SI. No.	Pollution Levels of SiR Insulator	Before UV aging		After UV aging	
		S _a (mg/cm ³)	ESDD (mg/cm ²)	S _a (mg/cm ³)	ESDD (mg/cm ²)
1	Low	0.2703	0.1976	0.4413	0.3227
2	Moderate	0.2445	0.1371	0.3626	0.1977
3	High	0.2575	0.2531	0.3526	0.3465

In addition, the algae, parasitic bacteria and fungi in rainforest areas may appear on the insulator surface [88] – [90]. Notably, the build-up of algae on the polymeric insulator's surface reduces the SiR insulator's hydrophobicity. The development of any organic layer on the surface of composite polymeric insulators can be reduced by applying flame-retardant fillers, e.g., Zine Borate [88]. The physical properties of the SiR insulators are investigated by visual inspection methods, such as cracks in the surface, surface irregularities, surface color change, surface erosion, and shade puncture [91]. In addition, the optical inspection method or scanning electron microscope (SEM) has been used to assess the physical degradation of SiR insulators [91].

1.6.2.2 Analysis of Chemical Properties

The significant changes in the chemical properties of SiR insulators as a result of aging effects are measured using the following techniques.

1.6.2.2.1 Fourier Transform Infrared (FT-IR) Spectroscopy

FT-IR spectroscopy technique is used to detect organic and inorganic substances in polymers. FT-IR spectroscopy is employed to obtain a range of wavelengths of electromagnetic radiation from solid, liquid and gaseous substances. The various chemical bonds present in the polymeric insulator material can also be analyzed by Fourier transform infrared (FT-IR) Spectroscopy. In addition, the Attenuated Total Internal Reflection (ATR) method detects increasing depolymerization on the surface of SiR insulators after aging [87], [92]. The chemical bonding of each substance and component type has a unique infrared (IR) signal absorption frequency. According to the process, if the ratio of the light energy falling on an object to the light energy transmitted through the object is zero, it means that the object has absorbed all the light energy. This ratio analysis determines the condition of the substances present in the insulator [93].

The depth of the insulator surface is obtained from the following Equation (2) i.e.,

$$\delta_p = \frac{\lambda}{2\sqrt{\hat{\rho}_c(\sin^2 \theta - (\hat{\rho}_s/\hat{\rho}_c)^2)^{1/2}} \quad (1.2)$$

Where, λ = wavelength (cm); $\hat{\rho}_c$ = crystal's refractive index (KRS5 = 2.38); $\hat{\rho}_s$ = Sample's Refractive index (SRI = 1.43); θ = angle of incident (45°); δ_p = penetration depth (μ -m). In the research works [8], the depth of the SiR surface was measured using an IR frequency and the range of the IR wavelengths was found to be 400 cm^{-1} to 4000 cm^{-1} . Gour *et al.* [23] reported that after the UV-A aging, the modifications in the chemical elements in the SiR polymers were observed. Similarly, Ethylene-Propylene-Diene Monomer (EPDM) has been studied by artificial weather exposure for 90 days, and changes in EPDM's mechanical properties, chemical properties, tensile strength and structural appearance have been observed using the FTIR spectroscopy method [92].

In [94], the investigation said that after 2000h, UV-B aging in HTV-SiR insulators, visible changes have been observed in the FT-IR spectrum in proportion to Si - CH₃, C - H bond. In [76], authors analyzed the changes in chemical structure after the aging of FRP rods of SiR insulators by FTIR method. The study's results suggest that the FRP rod's aging directly affects the number of waves within the chemical group. Here, changes in wave number have been identified from FTIR analysis.

1.6.2.2.2 Energy Dispersive X-Ray (EDX) Technique

The output of the EDX method is the spectrum that can identify the exact change in the chemical composition of any polymeric sample. It has been reported in [12] that due to the aging of SiR insulators, changes in the ratios of aluminum (Al) and silicon (Si) (filler material) have been satisfactorily evaluated with EDX analysis. Also, the results showed that the amount of low molecular weight (LMW) SiR polymer chains decreased due to the aging impact. Reynders *et al.* [2] reported in their article that the density of silicon molecules decreases to a depth of 100 nm from the surface of aged and contaminated SiR insulators. The physicochemical analysis is performed on aged SiR insulators to understand the surface morphology of the insulators [85]. The outcome of the EDX measurement depends on the surface depth of the SiR insulator. The thickness of the surface is measured by the increased voltage of the electron beam [12]. The penetration depth of the X-ray beam is calculated using the following formula [12].

$$D = 0.033 \left(e^{1.7} - e_c^{1.7} \right) \frac{A_w}{Z_n \rho_{Si}} \quad (1.3)$$

Where D is the penetration depth of the X-Ray beam, e is the beam of the electron energy (i.e., keV), e_c is the binding energy to excite the X-Ray line of activity, A_w is the atom's weight, Z_n is the atomic number, ρ_{Si} is the material's density. The article reported [94] that the SEM-EDX technique

Condition Assessment of Overhead Line Insulators

analyzed the changes in their chemical compositions after the aging of SiR insulators, and the test outcomes are shown in Table 1.10.

Table 1.10 Comparison study of SEM-EDX results [94].

Types of SiR Insulator Sample	Percentage of Chemical Components (%)		
	Si	C	O
Virgin	40.9	13.3	45.8
Aged	24.7	17.2	58.1

Similarly, the development of biological microorganisms on the surface of HV polymeric insulators can be effectively observed by EDX-based analysis [88] – [89].

1.6.2.2.3 X-Ray Diffraction (XRD) Technique

The XRD technique can analyze the polymeric materials' crystal structure [95]. The fundamental law behind the XRD method is Bragg's Diffraction Law. In the XRD event, X-rays fall on an element, then the intensity of the radiation emitted from the component and the scattered angle of the irradiated ray is measured. From these values, the material's crystal structure can be analyzed. The RTV-coated SiR polymers are physically corroded due to thermal aging and dry band arcing [56]. The detailed XRD analysis has been reported in [92], [95]. A comparison study was conducted by Verma *et al.* between two types of HTV-SiR insulators (i.e., HTV_{1S1} (fresh) and HTV_{2S2} (aged)) and they implemented artificial UV-C aging on two HTV-SiR variants [96]. After the XRD analysis plot, the result indicates that the samples became more crystalline after aging.

1.6.2.2.4 X-Ray Photoelectron Spectroscopy (XPS) Technique

The XPS method helps to measure the basic structure of the spectrum of photoelectrons emitted from the surface of an aged sample. A detailed discussion on the XPS measurement procedure has been reported in [3], [97] (shown in Table 1.11). It has been reported in [98] that with prolonged artificial aging, the concentration of the chemical elements of SiR insulators such as silicon (Si) and carbon (C) has been decreased. In contrast, the concentration of oxygen (O₂) has increased. Chakraborty *et al.* performed the aging test on three different specimens under three external conditions and the result of the XPS analysis is shown in Table 1.11 [3]. Moreover, from Table 1.11, it is concluded that the oxidation process occurs in the outer layer of the SiR insulator, increasing the concentration of oxygen elements.

Table 1.11 Results for HTV-SiR insulator samples after the aging test using XPS analysis under different conditions [97].

SI. No.	Samples	Percentage Composition (%)		
		Si	C	O
1	Not Polluted and no external stressed applied	23	53	24
2	Not Polluted but thermal stressed applied	19	45	35
3	Not Polluted but electro-thermal stressed applied	18	48	34

1.6.2.2.5 Secondary Ion Mass Spectroscopy (SIMS) Methodology

The method is utilized for analyzing the modification in the synthetic Structure of SiR protectors after aging like XPS analysis. The photoelectron effect plays an essential role in this process [99]. Secondary Ion Mass Spectroscopy (SIMS) is used to examine the emitted photoelectron's amount and energy from the elements of SiR insulators (i.e., excluding hydrogen) after aging. It is noted that each element has a unique bond energy value and that bond energy depends on the electron induction present in that element. This technique can also estimate the nature of the chemical bonds between the elements. In [99], Xilin *et al.* conducted an aging experiment on HTV-SiR samples and the chemical analysis of insulators' samples was performed using SIMS methodology. Test results showed that *Si*, *C* and *Al* molecules disappeared from the surface of the SiR insulator after the aging process. In addition, the aging process causes the *Si - O* bond to become fragile and as a result, the *Si* molecules begin to loosen rapidly. Similarly, the amount of *C* molecules decreases, and *CO₂* is released due to oxidation. The *Al* particles migrate from the surface of the insulator as they begin to react with acidic substances in the environment after aging, resulting in the formation of *Al₂O₃* particles.

1.6.2.2.6 Surface Roughness Methodology / Scanning Electron Microscopy (SEM) Technique

The morphology of the harshness of the surface of SiR insulators is analyzed by scanning electron microscope (SEM). Pollutants deposited on the surface of the SiR insulators also deteriorate the surface's chemical contents [13]. In [92], after artificial UV-C radiation, the changes in the SiR insulator were investigated by SEM spectroscopy between pure and aged samples. It is noteworthy that the surface degradation of the sample of aged SiR insulators was greater than that of the pure sample because oxidation occurred in aged

Condition Assessment of Overhead Line Insulators

SiR samples. Moreover, the Surface degradation of SiR insulator samples is higher in UV-C radiation than in other UV radiation [92]. The authors reported that the SEM technique was performed on the SiR samples at high vacuum mode to avoid charging [13]. Similarly, Chakraborty *et al.* reported that the gold sputtering method helped to eliminate the charging effects [3]. The findings revealed that the SiR insulators' sample was smooth, homogeneous, and had less porosity on the surface before UV aging. But the overall structural morphology has changed after aging. In addition, in [100], investigations have shown that any type of brittle fracture and decay-like fracture of the FRP rod of 500 kV composite insulator due to aging and corrosion-like fractures can be analyzed through the SEM method.

1.6.2.2.7 Gas Chromatography (GC) / Mass Spectroscopy Technique

The procedure of Gas chromatography (GC) is the technique for isolating chemical compounds in analytical chemistry. The Chemical compounds used to analyze in gas chromatography are those compounds that can evaporate without decomposition. This method also helps to determine the mass of molecules of various chemical elements of a gas. The GC method can analyze the impact of surface pollution levels on SiR insulators' LMW elements [101]. Gustavsson *et al.* [101] reported that the spot discharge on the SiR surface directly depends on LMW dimethyl-siloxanes. The GC method has been used in studies [7] to understand the properties of LMW molecules scattered from SiR insulator polymers due to contamination.

In [102], gas chromatography assessed the RTV-coated SiR insulator's surface erosion. The GC test was performed using two RTV-coated SiR insulators (i.e., aged sample and unaged sample). After the GC test, it was found that the aged sample had a continuous peak of LMW siloxane due to depolymerization. As a result of aging, these LMW siloxanes move away from the surface of the insulator, causing the RTV-coated SiR insulator surface to deteriorate.

1.6.2.2.8 Solvent Extraction (SE_x) Technique

Solvent Extraction (SE_x) is the widely used procedure to determine the chemical analysis of the aged SiR substance. SE_x method is conducted through four stages. Initially, the solvent enters the solid Structure; Then the dissolved substances are diffused into the solvent; Subsequently, the dissolved material is spread around the surface of the SiR insulator. Finally, the extracted solution is collected for analysis [7] – [8]. In this technique, the LMW components are extracted from the surface of the SiR insulator. A more accurate idea of surface erosion of the aged SiR insulator can be obtained using these extracted components in the FT-IR and GC methods [101, 102].

In [103], the post-aging properties of the surface of the HTV-SiR insulator were analyzed by the solvent extraction method. The HTV-SiR component comprises two groups of materials: HCR (High Compatible Rubber) and LSR

(Liquid Silicone Rubber). In this process, at room temperature, the sample was immersed in toluene for 96 hours. Afterward, the LMW particles were extracted once the solvent had evaporated entirely. The change in sample weight before and after evaporation measures LMW. After the SE_x technique, a comparative analysis of LMW between HCR and LSR has been shown in Table 1.12. Also, the aged surface of the SiR insulator sometimes contains negatively charged or positively charged particles. These particles can be detected by Cross-Over voltage (COV) analysis [104].

Table 1.12 Results of the Solvent Extraction method of HTV-SiR [104].

SI No.	HTV-SiR material Group	LMW (%)
1	HCR	0.0236
2	LSR	0.0396

1.6.2.2.9 Terahertz and Laser-Induced Spectroscopy Technique

The aging conditions of the composite insulators can be assessed after measuring dielectric properties by the terahertz technique. Research from the last decades revealed another diagnostic tool, Terahertz spectroscopy, which can predict material aging, potential defects in the insulators, etc. [105] – [106]. Terahertz spectroscopy is based on the Terahertz wave, which ranges from 0.1 THz to 10 THz (i.e., wavelengths range from 3 mm to 30 μm) [107]. Reasons behind the use of Terahertz spectroscopy are good resolution both in time and frequency domain than other Non-destructive Testing (NDT), easy to operate, suitable for complex test structural material, less ionizing effect, strong penetrability and that is why this spectroscopy can be used for aging assessment of SiR composite insulators [107]. Despite the advantages, only independent terahertz spectroscopy analysis is not suitable for minor errors due to its bipolar pulse and limited pulse width that creates overlapping of the signals [105]. Three types of artificially made defects, such as single air gap defect, inclusion defect and double-layer air gap defect, were investigated and their impacts on composite insulators were analyzed by terahertz spectroscopy with the combination of deconvolution method (to overcome the overlap), reported in [107]. The authors also suggested that these methods can be used for the internal defects of the composite insulators. Mei *et al.* reported in their article that the properties of five types of composite insulators (i.e., epoxy resin, epoxy glass fiber, XLPE, porcelain and HTV-SiR) were measured using terahertz spectroscopy and the broadband dielectric spectrometer (with the relatively low-frequency band (i.e., 1 Hz to 1 MHz) and a comparative analysis was carried out for both the techniques [107].

Nowadays, it is an area of concern for the researcher to diagnosis of degradation of the insulators remotely. For this purpose, Laser-Induced Breakdown Spectroscopy (LIBS) can be employed to estimate the

Condition Assessment of Overhead Line Insulators

degradation of the insulator electrically and chemically [108]. This spectroscopy has some advantages like non-contact analysis, high spatial resolution and multi-element analysis, and Qualitative and Quantitative Analysis can be carried out [108], [109]. The application of this spectroscopy includes detecting contaminants present in insulator surfaces and identifying structural morphology changes after aging. Therefore, early flashover of the insulator can be predicted by detecting accurate contamination on the insulator surface [109]. Laser-Induced Breakdown Spectroscopy (LIBS) was reported in [109]. Wang *et al.* investigated the spectral properties of extinct components of HTV-SiR insulators from its surface after aging and the change in temperature properties from plasma was also reported. That will help predict HTV-SiR insulators' service life [109]. Also, the spread of fungi and algae on the surface of SiR insulators is clearly understood by applying laser-made Florence spectroscopy [107], [109].

1.6.2.3 Analysis of Electrical Properties

Different electrical methods help to analyze the electrical properties of SiR insulators. These are (a) surface leakage current (b) partial discharge (c) corona discharge and (d) flashover voltage analysis. A detailed description of these aforesaid analyses is described in the following sections.

1.6.2.3.1 Surface Leakage Current Analysis

Surface Leakage Current (LC) investigation is a well-recognized strategy for identifying the differences within the electrical parameters of the overhead line insulators. The surface condition of the overhead line outdoor insulator has been responsible for the amount of LC flow [110]. It is noteworthy that due to high hydrophobicity, leakage currents become negligible in the early stages of aging. As the aging progresses, the hydrophobicity of the insulator decreases and the flow of leakage currents increases [110].

Mostly, overhead line insulators are installed in outdoor applications. The environmental impact on them is also severe. At the early stage of service of outdoor insulators, the insulator's surface behaves as non-conductive. Whenever the surface of the insulator becomes contaminated, it becomes conductive. As a development conductive path on the surface of insulators, the surface LC begins to flow, and the waveshape of the surface LC current is distorted as time progresses [111]. It has been observed that the deformation of LC is related to the surface condition, chemical property of the contaminant layer, environmental temperature, humidity, and acid rain [111]. The optimal approach to determine the level of contamination on an insulator is to employ a method that remains unaffected by external factors. To comprehend the lifespan of insulators, it is imperative to investigate and analyze the leakage current signals on the insulator's surface.

1.6.2.3.1.1 Factors for Estimating the Surface Degradation of Overhead Line Insulators

According to the various literatures [57], [60], [72], [110], it is noteworthy to mention that the factors responsible to estimate the surface degradation of overhead line insulators are: magnitude of the surface leakage current (SLC), ratio of 5th to 3rd harmonic components of SLC, estimation of total harmonics distortion (THD) and estimation of phase angle between SLC and input voltage profile. The detailed discussion on aforesaid factors which help to estimate the surface quality of overhead line insulators using SLC signals is illustrated below.

1.6.2.3.1.1.1 Amplitude of Surface Leakage Current

The insulator surface gradually becomes contaminated due to the deposition of dust and salt particles which are originating from different geographical locations [112] – [113]. When moisture is present in the air, surface leakage current initiates a flow around the exterior of the insulators. Analyzing the magnitude of the leakage currents provides significant insights into the performance of the insulator's surface. Notably, Surface leakage current proceeds through a sequence of three stages [114]. The first stage is called the security stage where the allowable limit of surface leakage is less than 50 mA. The second stage is the forecast stage where less than 150 mA of surface leakage current can flow through it. The last stage is a dangerous stage where more than 150 mA of surface leakage current can pass through the surface [114]. During the forecast and danger periods, the amount of leakage current is higher compared to the security period, and it can be easily noticed [114]. The duration of current leakage in these two stages is insufficient to provide adequate warning time. The security stage, which occurs prior to the flashover event, has a longer duration and can be observed in advance [114].

In addition, peak value of leakage currents can be used as an indicator to evaluate the state of insulator surfaces. Prior to the flashover event, the peak value indicated the highest intensity of leakage current [112] – [113]. The occurrence of this peak value of leakage current (LC) is associated with partial electrical discharge that occurs on an insulator's moistened surface. It is noteworthy that the maximum value of the surface leakage current varies proportionally with the growth of partial discharge on the surface of the insulator [114]. Moreover, under the influence of wet conditions, the magnitude of LC in Ethylene Propylene Diene Monomer (EPDM), glass and porcelain type insulators are significantly lower [110]. The flow of LC current in SiR insulators is higher in humid environments in comparison with dry environments [29]. The magnitude of the LC for both porcelain (I_p) and SiR insulators (I_{SiR}) depends on three environmental factors like illuminance, temperature, and relative humidity [115]. The comparative findings among the aforesaid factors are shown in Table 1.13.

Condition Assessment of Overhead Line Insulators

Table 1.13 Porcelain and SiR insulators Leakage Current's deviations with environmental constraints [115].

SI No.	Leakage Current (mA)	Illuminance (L)	Temperature (° C)	Relative Humidity (%)
1	I_p	-0.727	-0.853	0.885
2	I_{SiR}	-0.495	-0.614	0.671
3	I_p / I_{SiR}	0.106	0.199	-0.185

In addition, in Fig. 1.7, the LC waveform's magnitude variation for 11 kV-rated outdoor SiR insulators under five types of contamination levels (as per IEC 60507) is shown [29]. Pylarinos *et al.* showed that in their study, any progressive LC waveform could ultimately lead to the flashover of the SiR insulators [116].

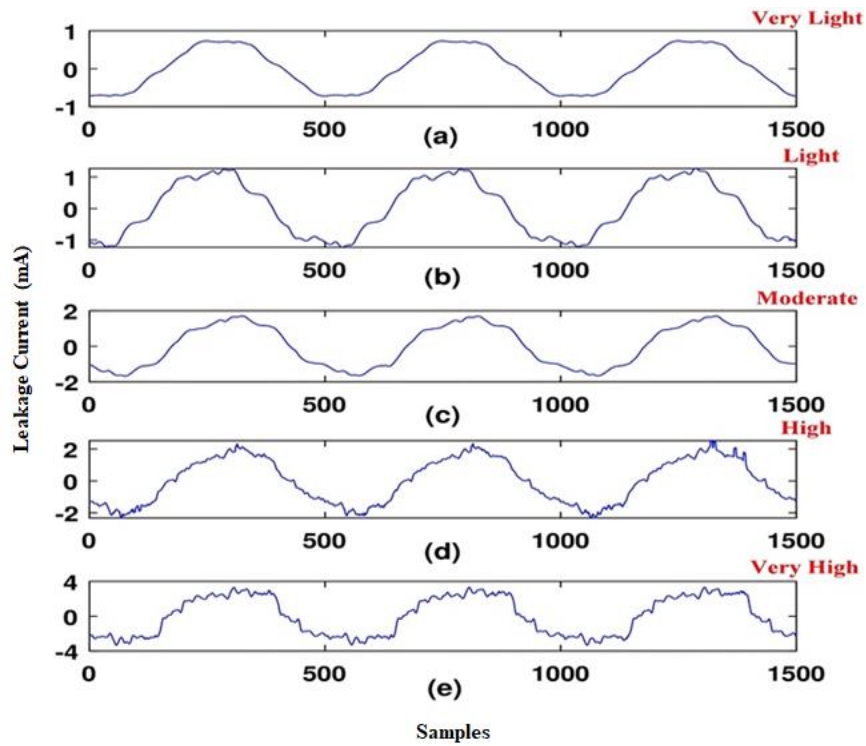


Fig. 1.7 The patterns of the LC waveform vary with the contamination levels: (a) Very Light, (b) Light, (c) Moderate, (d) High and (e) Extremely High contamination, respectively [29].

1.6.2.3.1.1.2 Ratio of 5th to 3rd Harmonics Components of Surface Leakage Current

Overhead line outdoor insulator's surface degradation can be inferred from the connection between the 5th and 3rd harmonic components of the surface leakage current [73]. In [117], reported that the amount of the fifth harmonic component in a clean insulator surface is greater than that of the third harmonic component of surface leakage current. Moreover, if the 5th harmonic component is larger than the 3rd harmonic component of the surface leakage current then, the insulator remains in a normal state, or at a low contamination level state [73], [117]. The contamination surface conditions of overhead line insulators are primarily determined by the third harmonic component's analysis. The increase of the third harmonic component in leakage currents is usually because of higher humidity and pollution levels. Moreover, the presence of moisture and impurities make it easier for electricity to flow through the surface of the insulator [117]. The presence of irregular resistance on the surface of the insulators causes the surface leakage current to exhibit a non-sinusoidal wave pattern that is distinct from a regular waveform [117]. The expansion of leakage current leads to the creation of dry bands on the insulator's surface, potentially resulting in partial discharges. Because of this, the shape of the leakage current waveform changes [117]. In this situation, the third harmonic component of the surface leakage current increases. The degradation of leakage current waveforms is a direct consequence of the escalation of partial discharge [117]. It was reported in literatures that the presence of odd harmonics in the LC signal distorts the nature of the signal, which is related to the poor condition of the surface of the SiR insulator [87], [89], [110]. Flashover is never observed in situations where the clean surface of overhead line insulators, provided that the 5th harmonic component exceeds the 3rd harmonic component by a magnitude of over 100%. Whenever the ratio decreases to less than 30%, a flashover occurs. Predicting the occurrence of a flashover holds immense significance using the 5th to 3rd harmonic ratio [117]. In [118], under humid conditions, the permeation of water molecules in the FRP rod and SiR interface has been studied through rotation wheel tests and analysis of surface LC flow. Also, the authors performed an FFT analysis on LC data to understand the development of the arc. The impact of arcing was analyzed by calculating the relative magnitudes of the 3rd and 5th harmonic components of LC. A comparative study among the three parameters from the initial period to the final period of aging is shown in Table 1.14.

Condition Assessment of Overhead Line Insulators

Table 1.14 Comparative Analysis of Leakage Current Flow, Power Dissipation and Surface Resistance of Aged SiR Insulators [118].

Sl. No.	Condition	Leakage Current	Power Dissipated	Surface Resistance
1	Initial Part of Aging Period	Low	Low	High
2	End of the Aging Period	High	High	Less / Low

1.6.2.3.1.1.3 Calculation of Total Harmonic Distortion (THD)

Analysis of distortion in leakage current can be achieved through Total Harmonic Distortion (THD) [73]. Mathematical equation (1.4) gives the THD expression as:

$$THD = \frac{\sqrt{\sum_{n=2}^{\infty} i_n^2}}{i_1} \quad (1.4)$$

Where, i_1 is fundamental component of the surface leakage current and i_n is n^{th} order harmonic component of the surface leakage current. Heavily corroded insulator housing drastically decreases electrical performance due to contaminant deposition [73]. In humid conditions, contamination layers on the surface of the insulators increase the current density which leads to an increase in leakage current to flow through the surface [73]. Consequently, a non-uniform voltage distribution appears on the surface of the insulators followed by localized dry bands. This causes a distorted waveform of leakage currents as shown in Fig. 1.7. The aforesaid phenomena can be analyzed by total harmonic distortions [73]. Additionally, with an increase in input voltages and humidity levels in the atmosphere, total harmonic distortion (THD) also rises [73]. The magnitude of leakage currents at higher humidity conditions is higher, as is the distortion of the waveforms, especially at the peak of the leakage current waveforms. In the presence of high moisture levels, insulators are prone to generating sparks due to the occurrence of a surface leakage current having a predominant odd harmonic pattern. When voltage levels are decreased, the distortion of the leakage current shape becomes almost symmetric. In Addition, overall distortion is greatly influenced by the fifth and seventh harmonic components [73]. In contrast, the third harmonic component becomes larger with the application of higher voltages [119]. Notably, THD rises in the presence of more humidity, increased voltage, and additional contamination, which plays an utmost importance during the LC study.

1.6.2.3.1.1.4 Calculation of Phase Angle

Understanding the insulator surface's condition can be achieved through the application of phase angles to analyze leakage currents and supply voltage [33]. If the surface is free from dirt or moisture, the leakage current serves as an indicator of the existence of an RC circuit [31]. Notably, if there are only minor electric current leakages, the angle between the supply voltage and LC will be nearly 72 degrees [31]. As a result, insulators that are dry on the exterior can function as high-resistance RC circuits, even in the presence of limited contamination layers. Less than 1 mA of current is able to be discharged as a result of this situation [31]. The presence of moisture and slight contamination in the vicinity of the insulator's surface causes a significant drop in the phase angle between LC and input voltage, i.e., nearly 29 degrees [31]. Also, a substantial rise in surface leakage current has been noticed. The reason for the increment in surface leakage current flow and localized surface discharge is because of the decrement in surface resistance of outdoor insulators in humid atmospheres. Notably, under that condition, the phase angle falls in the range of 6 to 16 degrees [31]. In a study, researchers found that under humid conditions and high surface contamination, the electrical behaviour of insulators is similar to that of a circuit with high resistance [31]. Therefore, according to phase angle inspection, wet and clear contaminated insulators can be clearly distinguished [31]. It is relevant to mention that the aging condition of any types of insulators can be analyzed by observing the actual displacement of the phase angle of LC and the nature of the LC.

1.6.2.3.2 Partial Discharge (PD) and Corona Analysis

It has been reported that the onset of partial discharge event is due to uneven voltage stress, production error, contamination intensity, humidity, dry band effect and accumulation of water droplets on the surface of SiR insulators. Compared with the HVDC system, the PD inception Electric field strength intensifies for the High Voltage AC (HVAC) system. The time duration of the PD event lies in-between nanoseconds to microseconds [120]. Using suitable micro or nano-fillers can enhance the electrical properties of SiR insulators, such as dielectric strength, tolerance to induction voltage, and preventing partial discharge (PD) [120].

Chandrasekar *et al.* reported in [120] that the surface degradation of SiR insulators could be determined by analyzing the nature of the partial discharge. In [121], the authors performed a PD test in the laboratory (i.e., according to IEC-60507 standards) on an 11 kV rated SiR insulator with variable ESDD values. The test consequences exhibited that the magnitude of PD raised with increasing values of ESDD, but during the experiment, the relative humidity value was unchanged. Ullah *et al.* [121] observed that the average PD value for artificial UV-aged HTV-SiR insulator samples increased with increasing applied voltage. Also, the authors reported a comparative PD analysis between the pure and aged (UV aged approx. 5000 h) HTV-SiR samples, and the results showed that surface degradation was

Condition Assessment of Overhead Line Insulators

more pronounced in the aged samples [121]. Similarly, the nature of the PD pulses can be measured by video apparatus [122], image strengthening UV videography [2], [8], and thermographic video recorder [2], [8], [9]. Sometimes PD can be detected using audio amplifiers [121] and communication devices [123]. In addition, the video thermography measurement helps to calculate the power loss from different types of surface discharges [124]. The arc resistance measurement is another methodology to analyze the SiR insulator's localized discharges [123]. It is reported [124] that an alternating electric field under the HVAC system predominates in the perimeter of the insulator and this helps to strengthen the PD phenomenon even faster. Physical degradation of the insulator begins when PD begins. The authors suggest that analyzing the PD event at the early stage of aging with the clean surface of the SiR insulators is very difficult. Another symptom of local discharge on the surface of the insulator is corona discharge. It is also worth noting that corona or surface discharge problems are more severe in HVAC systems than in HVDC [125]. Similarly, the other factors, relative humidity, temperature, deposited water droplet's size on the surface of SiR insulators, the diameter of conductors, and the surface area of SiR insulators [126], intensify corona discharge. At higher relative humidity, the frequency of corona events increases rapidly; corona emission power also increases. Lan *et al.* reported in their article [32] that RTV-SiR insulators had better corona resistance than HTV-SiR insulators. Extensive research has been conducted on the effect of electrical discharge on HTV-SiR insulators, and it has been found that adding nano/micro silica or ATH fillers can reduce the effect of electrical discharge on SiR insulators [126]. Studies have shown that the effect of the corona is first seen in water droplets that accumulate on the surface of the insulator [126]. Zhu *et al.* [127] reported in their article that the corona discharge phenomenon was investigated on HTV-SiR insulators by a laboratory-made parallel needle plate electrode system, and the changes in the Physico-chemical properties of the HTV-SiR insulators were reported in this work. After corona discharge, the hydrophilic state of the SiR insulator develops, resulting in erosion on the surface of the insulators [128]. It has been reported in [125] – [127] that any surface discharge phenomenon degrades the surface resistance of SiR insulators. The surface discharge is one of the most threatening agents that creates the depletion of the surface elements (i.e., up to 20 nm depth) [128]. Any long-term surface discharge permanently damages the SiR insulator's properties [128]. The chemical analysis of corona aged surface of SiR insulators can be analyzed using Nuclear Magnetic Resonance (NMR) detection, scanning electron microscopy (SEM), gas chromatography and FT-IR techniques [128]. It is clearly understood that the corona/surface discharge analysis depends on various uncontrollable factors.

1.6.2.3.3 Analysis of Flashover Voltage (FOV)

Flashover Voltage (FOV) analysis is the most common electrical diagnosis method to measure the aging state of SiR insulators. The power frequency pollution FOV test can be performed either at the AC or DC voltage level [106]. The insulator's power frequency pollution flashover test is greatly affected by the insulator's surface properties. Any electrical discharge on the surface of the overhead line insulator can ultimately lead to the flashover event. After the flashover event, insulators start losing their physical, chemical and electrical properties [79].

Khatun *et al.* reported in their article [130] that the value of FOV obtained after testing at AC-voltage levels was higher than that of DC-voltage levels and performed a comparative analysis of pollution FOV measurement in dry and wet type porcelain and SiR insulators. After the pollution FOV test, the result said that the SiR insulator performs well (i.e., 5% better) under a highly polluted climate than the porcelain insulator. Ahmadi-Jonidi *et al.* reported [79] that the surface of SiR deteriorates after artificial UV-aging and the long-term effects of artificial UV-aging lead to the complete breakdown of the SiR insulator. In [79], The authors performed three types of FOV tests on the effect of artificial UV exposure. The comparative analysis based on odd LC harmonic values is shown in Table 1.15.

There are two types of FOV testing methods used to analyze the electrical properties of SiR insulators such as the Rapid-Flashover Clean Fog (RFOCF) method and the Quick-Flashover Salt Fog (QFOSF) method [131]. It has been reported [129], [131] that salinity levels are directly correlated with the surface resistivity and aging condition of SiR insulators. Due to the high salinity level, a uniform conductive layer is formed on the surface of the SiR insulator. As a result, the dry band is created around the circumference of the insulators. After the dry band arcing, the $Si-CH_3$ and $C-H$ bonds of the SiR insulator become fragile. Also, the filler particles (i.e., mainly ATH) disappear from the surface after the dry band arcing, resulting in degradation of the hydrophobicity property. The combined effect of all types of surface discharge eventually leads to the FOV event [79]. Albano *et al.* investigated the dry band flashover phenomena on SiR insulators by the clean-fog test along with the Infrared image analysis and surface Leakage current measurement [132]. They highlighted some of the information that artificially contaminated and wet surfaces of SiR insulators are the leading cause of dry band formation. Also, they concluded that the rapid formation of dry bands might cause a flashover event.

Condition Assessment of Overhead Line Insulators

Table 1.15 Representation of odd LC harmonics in surface flashover before and after UV exposure [79].

Sl. No.	LC Types	Magnitude of LC (mA)					
		Test 1		Test 2		Test 3	
		Before UV	After UV	Before UV	After UV	Before UV	After UV
1	I _{max}	10.531	14.9	13.341	15.011	15.132	19.895
2	I _{1st}	1.638	2.05	3.278	2.784	2.543	5.183
3	I _{3rd}	0.872	0.931	1.575	1.335	1.232	2.592
4	I _{5th}	0.201	0.128	0.122	0.162	0.112	0.318
5	I _{7th}	0.0772	0.049	0.183	0.119	0.154	0.331
6	I _{9th}	0.033	0.003	0.014	0.022	0.040	0.049
7	I _{11th}	0.035	0.005	0.036	0.021	0.055	0.010
8	I _{13th}	0.011	0.017	0.026	0.017	0.005	0.053

1.6.2.3.4 Analysis of Erosion and Tracking Resistance

Erosion and tracking resistance are the two essential parameters for investigating the electrical characteristics of SiR insulators. These two tests can be used in SiR polymeric insulators as per IEC TR 62730:2012 standard [123]. The eroded SiR insulator means reducing the weight of the materials during the manufacturing process. On the other hand, the carbonization process helps to construct conductive paths on the surface of the insulator through electrical tracking. It has been observed that LC flows in the tracks, which causes insulation breakdown. The continuous surface discharges cause thermal degradation, leading to the erosion and tracking of SiR insulators. The comparative index and dry band arcing tests are the two well-known techniques used to analyze the tracking and erosion properties of SiR insulators [133]. Ghunem *et al.* [134] proposed an inclined-Plane Test (IPT) method that can measure the resistance of erosion and tracking of the SiR insulators. The standards of IEC-60587 and ASTM-D-2303 were followed during the IPT measurement [135]. Dutta *et al.* described the IPT method step by step in their article [136]. The minimum voltage for conducting the test should be more than 6 kV [135]. Schmidt *et al.* in [137] presented a comparative analysis among ATH, Silica and Melamine Cyanurate filler-based SiR samples for investigating the tracking and erosion resistance. They also reported that silica (i.e., 100 phr) and melamine cyanurate (i.e., 15 phr) filler-based SiR samples hold good tracking and erosion resistance. The findings of the aforesaid assessment are tabulated in Table 1.16.

Table 1.16 Comparative analysis of Tracking and Erosion properties of various SiR additives [137].

SiR additives in phr	Erosion Depth (nm)	Surface Hardness (Shore A)	Density (gm/cm ²)
Silica - 100	1.3	87	1.61
Silica - 25 and ATH - 75	2.1	88	1.58
Silica – 100 and Ammonium Polyphosphate – 30	3.5	89	1.91
Silica – 100 and Melamine Cyanurate - 15	0.9	87	1.62

Also, it has been found that samples made of melamine can extinguish electrical arcing. Frang *et al.* reported that Ureido-modified MQ silicone resin (DIPUPES-MQ) could perform better than Addition-cure Liquid Silicone Rubber (ALSR) because DIPUPES-MQ has boosted tracking and erosion resistance [133]. The aforesaid techniques are not applicable in low voltage applications [8] but are used to analyze the tracking and erosion properties as well as to analyze the impact of dry-band arcing on SiR insulators [134]. The fillers play a vital role in controlling erosion and tracking event in SiR insulators. Applying nano-scale fillers such as alumina makes SiR insulators better surface resistant to contaminant circumstances [124]. In [139], the authors investigated and concluded that SiR insulators are made with three types of economical fillers. These are Alumina Trihydrate (ATH), Aluminium Nitride (AlN) and Boron Nitride (BN) [22], [26] – [27]. A way to add more silicone bonds to the crosslinking fashion that improves the tracking and erosion resistance properties of SiR insulators [139].

Similarly, the nano doping of silica (SiO₂) is used in the SiR insulator to improve AC corona resistance, enhance the tracking resistance and decrease erosion [124] – [125]. Adding barium titanate as a filler to the RTV-SiR component may reduce erosion and increase tracking resistance [133]. Bian *et al.* observed that the SiR insulators could achieve higher tracking and corrosion resistance if the insulator material were fabricated by the electrospinning method [140]. In addition, the tracking and erosion resistance of SiR insulators can be improved by adding BN fillers with ATH components [141]. The effectiveness of inorganic fillers in SiR insulators can be evaluated based on thermal conductivity, thermal resistance, mechanical strength, electrical conductivity, hydrophobicity and electrical trace

Condition Assessment of Overhead Line Insulators

resistance. The detailed evaluation study on the effectiveness of inorganic fillers is tabulated in Table 1.17.

Table 1.17 Comparative analysis of various Inorganic Fillers of SiR Insulators [133] – [141].

SI. No.	Effective Properties	Change in the properties after application of Filler Elements
1	Electrical Conductivity	Improved by: Boron Nitride (BN), Graphite. Degrade by: Al ₂ O ₃ , CaCO ₃
2	Thermal Conductivity	Improved by: Boron Nitride (BN), ATH, SiO ₂ , Silicon Carbide, Al ₂ O ₃ , ZnO, BaTiO ₃ , TiO ₂ , Graphite
3	Hydrophobicity	Improved by: ATH, SiO ₂ , CaCO ₃ .
4	Mechanical Strength (Tensile Strength)	Improved by: ATH, SiO ₂ , TiO ₂ , ZnO, BaTiO ₃ , Carbon Black. Degrade by: Boron Nitride (BN), Silicon Carbide.
5	Electric Trace Resistance	Improved by: Al ₂ O ₃ , CaCO ₃ Degrade by: Boron Nitride (BN), Graphite.
6	Heat Resistance	Improved by: ATH, SiO ₂ , Al ₂ O ₃ , ZnO, BaTiO ₃ , Graphite, CaCO ₃

1.7 Scope of the Thesis

In this thesis, various data analysis models of leakage current have been implemented for forecasting the condition of in-service overhead line insulators. The thesis model is segregated into three sections: data acquisition, feature extraction from the acquired data and feature classification from the available feature sets to identify the contamination class of overhead line insulators. In this thesis work, different signal processing models such as mathematical morphology, hyperbolic Stockwell transforms, and cross-hyperbolic Stockwell transforms have been used to identify the condition of overhead line insulators of any dimension, which will help to avoid premature failure of the insulator and power. This thesis is organized as follows:

Chapter 1: Chapter 1 of the thesis discusses ongoing research into various condition assessment methods for overhead line insulators. Moreover, this chapter highlights the proposed research problem related to overhead line insulator surface degradation.

Chapter 2: Chapter 2 describes the operation of the overall experimental setup used in this work. In addition, the process of constructing a synthetic sample preparation as per IEC standards and the process of data acquisition are elaborately demonstrated in this chapter.

Chapter 3: In Chapter 3, mathematical morphology and machine learning-based Random Forest classifiers are employed to identify suitable features from the raw surface leakage current data. It is noteworthy that surface leakage currents provide useful information about the surface health of porcelain insulators. In addition, the aforesaid methods optimized acquired features using a filter algorithm. This proposed model can precisely detect different surface contamination levels of overhead line porcelain insulators using a non-stationary surface leakage current signal.

Chapter 4: Chapter 4 represents hyperbolic Stockwell transform-aided time-frequency domain surface leakage current analysis to predict the surface contamination of overhead line Silicone Rubber (SiR) insulators. In this framework, the time domain surface leakage current is transformed into a time-frequency domain image using Hyperbolic Stockwell Transform (HSWT). Moreover, the most suitable features are extracted from the aforesaid model and fed to four machine-learning classifiers to identify the surface contamination class of SiR insulators. In terms of determining the insulator's condition, the proposed method shows satisfactory results.

Chapter 5: Chapter 5 presents a cross-spectrum-aided deep learning framework to predict Silicone Rubber (SiR) insulators' surface contamination. In this framework, the surface leakage current (SLC) of SiR insulators at different surface contaminations has been cross-correlated in a time-frequency plane with a reference signal to identify non-stationary

changes with respect to surface contamination. In this regard, the cross hyperbolic Stockwell transform technique has been implemented on SLC to convert the time domain information into time-frequency domain images. In addition, CNN-based deep learning algorithms have been used in this chapter to extract the most optimal information from the cross-time-frequency spectrum of SLC, which can automatically predict SiR insulators' contamination severity. The effectiveness of the proposed model has been verified on SiR insulator samples of different dimensions.

Chapter 6: This chapter summaries an overview of the thesis work, which includes a discussion of the research gaps, findings, and comparisons of the proposed research model with existing research. Moreover, the author addresses possible research opportunities and developments in the condition assessment study of overhead line insulators.

1.8 Originality of the Thesis

To the best of the author's knowledge, the following are original contributions to the present work:

Modern power system networks are concerned about the potential dangers posed by overhead lines and outdoor insulators. In polluted insulators, the leakage current that flows on the surface increases quickly when there is moisture. Ultimately, it will trigger a discharge in a dry band, subsequently resulting in a flashover incident. It is necessary to clean and repair insulators that are dirty consistently. Researchers have suggested different ways to check the condition of the surface of the overhead line insulators, like measuring phase angle, partial discharge analysis, and analyzing the impact of the odd harmonic on leakage current signature due to contamination. The success of these techniques is contingent upon the voltage being employed. Therefore, it is important to have the precise information about voltage in order to use those techniques. Determining the actual state of an insulator can be challenging due to the fluctuation of input voltage during testing.

In light of this, it is recommended to employ a technique that can identify the pollution level on insulators, without considering the voltage applied. This is why studying the surface leakage current signature is the best approach for analyzing the insulators' life span. Based on the information mentioned above, the following developments in this thesis work are:

- A method has been suggested to develop Mathematical Morphology aided Random Forest classifier-based model to analyze surface leakage current signals and determine the pollution levels on overhead line insulators.
- Development of machine learning classifiers based a time-frequency domain model for estimating the contamination severity of insulators using surface leakage current signatures.

- Development of a cross-spectrum aided deep learning and transfer learning-based CNN model for prediction of contamination severity automatically employing surface leakage current signals of overhead line insulators.

Chapter 2

Experimental Setup for Surface Leakage Current Signal Acquisition and Procedure of Artificially Contaminated Sample Preparation

2.1 Introduction

Most overhead line insulators are employed for outdoor applications, due to which pollutants accumulate on the surface of outdoor insulators. It is noteworthy that incremental surface contamination reduces surface insulation resistance. As a result, the surface conductivity of overhead line insulators also changes. It has been reported in various research articles [31], [142] – [143] that the outer surface of overhead line insulators is mainly affected by different climatic conditions like fog, raindrops, dew, sea salt, sand, dust, soil, and air pollution. In coastal areas, predominant environmental contaminants such as sand, dirt, and soluble salt ($NaCl$) accumulate on the surface of overhead line insulators. In rainforest regions, the pollutant is mainly Kaolin ($Al_2Si_2O_5(OH)_4$) that accumulates on the surface of overhead line insulators.

The clean surface of overhead line insulators cannot form a conductive path with water particles in humid conditions because the water particles are deposited on the clean surface as a droplet instead of making a water film (as shown in Fig. 2.1).

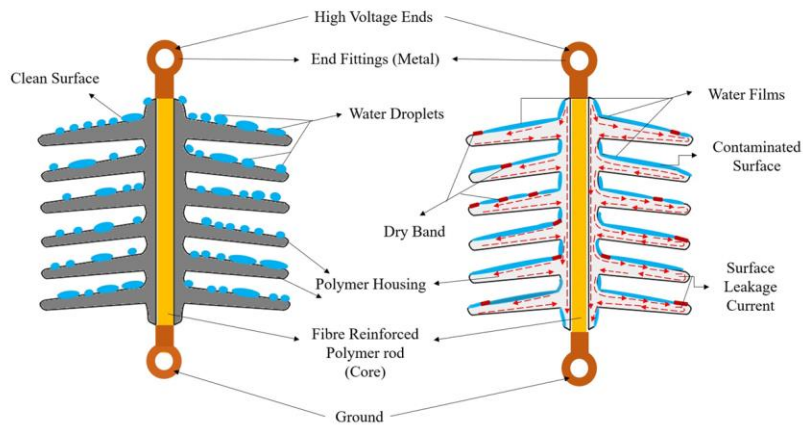


Fig. 2.1 Images of deposited water droplets on the surface of overhead line insulators [13].

On the other hand, accumulated pollutants degrade the surface insulating property of overhead line insulators. Soluble pollutants can easily mix with molecules of water and then develop conduction paths on the surface of overhead line insulators. It was noticed that at the junction of the water

Experimental setup for surface leakage current signature acquisition and procedure of artificially contaminated sample preparation

droplets, air, and overhead lines insulators' surface the electric field severity is highest [7], [145]. In addition, the deformation in the shape of the water droplets is more prominent towards the applied electric field. The surface leakage current flows through the contaminated housing of overhead line insulators. The amplitude of the surface leakage current relies mainly on the dissolved pollutants. It is worth noting that higher levels of contamination increase the leakage current flow at the insulators' surface. The surface temperature of the overhead line insulator is also increased due to the joule-heating effect. As a result, the water molecules evaporate from the wet surface, causing dry bands to form, followed by dry band discharge phenomena on the surface of the overhead line insulators noticed. Due to the dry band effect, the voltage is not uniformly distributed across the surface of the insulator. Subsequently, this dry band discharge phenomenon causes erosion as well as tracking phenomena on the surface of outdoor insulators. Ultimately, flashover events occur in overhead line insulators for the reasons mentioned above, leading to the failure of overhead line insulators. Therefore, scheduled condition monitoring of overhead line insulators for an uninterrupted power supply is essential.

According to the published literature [31], [124], [142] – [143], the surface leakage current signal is a dynamic parameter because it varies with changes in pollution intensity. It is noteworthy that surface leakage current measurements are more consistent and effective than traditional methods such as equivalent salt deposit density or ESDD [7], [142] – [143]. The disadvantages of ESDD are time-consuming and laborious procedures. In addition, ESDD is practically not feasible.

Another important parameter to detect outdoor insulators' surface contamination severity is by the odd harmonic component analysis of the surface leakage current signal. In [144], to identify the degree of surface contamination of outdoor insulators, the ratio proportion of the 3rd and 5th harmonic components of the SLC was used as an indicator. However, the surface leakage current analysis using odd harmonic analysis has several limitations; These are:

- (i) Perturbation appears in the surface leakage current signature because of supply voltage fluctuations and impact of odd harmonics, which may lead to inaccurate information about the surface contamination assessment [144], [146].
- (ii) However, on a clean surface, the nature of leakage current through overhead line insulators is almost static. But on contaminated surfaces, the nature of surface leakage currents becomes highly distorted, and their profile has a partial arc which is not able to provide precise information about the contamination level by using the odd harmonics ratio method [144]. It has been found that, ratio analysis of 3rd to 5th harmonic signals is mostly favourable for stationary signals [144].

Another condition assessment indicator is Fast Fourier Transform (FFT) which utilities for analysing the harmonic profile in stationary signals [146]. In this regards, FFT analysis is unable to provide precise information after analysing odd harmonics components from the surface leakage current signal.

Surface leakage current signal measurement and analysis is the better approach for determining outdoor insulators' surface contamination due to the aforementioned facts.

2.2 Experimental Procedure

The experimental procedure for the condition assessment study of outdoor insulators has been divided into two segments in this work using surface leakage current signals: (i) preparation of samples and (ii) data acquisition setup for the measurement of surface leakage current (SLC) signal. A detailed discussion is described in section 2.2.1.

2.2.1 Preparation of Samples

Measuring surface leakage current from overhead line insulators currently in service is challenging. Similarly, surface contamination of outdoor insulators is also tough to detect by seeing them. For this reason, The Solid Layer Method (SLM) is used in the laboratory to prepare a variety of artificially contaminated samples [145], [146]. In the presented work, some overhead line insulators were collected from the power substation to prepare artificial contaminated samples in the laboratory. Basically, two types of overhead line insulators were employed in this work, these are Silicone Rubber (SiR) insulators and porcelain insulators disc. The technical specifications of overhead line insulator samples collected from power substations are illustrated in Table 2.1.

Table 2.1 Technical properties of both SiR and Porcelain disc insulators.

	Parameters	Technical Details
SiR Insulator	Housing Material	Silicone Rubber (SiR)
	Rated Voltage	11 kV _{rms}
	Total Creepage Distance	320 mm
	No of Disc	3
	Disc Diameter	124 mm
	Sectional Length	250 mm
	Weight	730 g
	Rated Voltage	33 kV _{rms}
	Total Creepage Distance	900 mm
	No of Disc	8
	Disc Diameter	124 mm
	Sectional Length	400 mm
	Weight	1024 g

Experimental setup for surface leakage current signature acquisition and procedure of artificially contaminated sample preparation

Porcelain Insulator	Housing Material	Porcelain
	Rated Voltage	11 kV _{rms}
	Total Creepage Distance	338 mm
	No of Disc	1
	Disc Diameter	257 mm
	Axial Height	145 mm
	Weight	4298 g

Generally, in the SLM method, overhead line insulators are artificially contaminated by providing a coating on their housing or surface. Distilled water, *NaCl* or *KCl* salt and kaolin ($Al_2Si_2O_5(OH)_4$) were used to prepare a slurry. Kaolin serves as a non-conductive component and *NaCl* salt acts as a conductive component in the chemical composition of slurry. Then, the surface of the overhead line insulators was painted with laboratory made slurry and they were left in the open air to dry at room temperature for 24 hours. Images of artificially contaminated samples of SiR and porcelain insulators are shown in Fig 2.2.



Fig. 2.2 Images of different types of contaminated overhead line insulators.

In addition, during the preparation of artificially contaminated samples, the room temperature was varied from 28°C to 32°C. It is noteworthy, the samples were washed by employing isopropyl alcohol and deionized water before preparation of the artificially contaminated samples. In order to get rid of the dirt that accumulated on the surface of overhead line insulators needed to be cleaned the surface first. In [70], it was reported that both *NaCl* and *KCl* salts are key components of natural contamination. In this work, *NaCl* was used in the slurry preparation. The amount of *NaCl* salt in the slurry has an

effect on the artificial contamination layer's conductivity. Thus, by varying the amount of $NaCl$ salt, the severity of artificial contamination was varied [70], [145]. It is pertinent to mention here that artificial contaminated insulators samples were prepared according to the IEC 60507 standard for experimental purposes [149]. The schematic of the artificial contamination preparation of overhead line insulators is shown in Fig. 2.3.



Fig. 2.3 Flowchart of artificial surface contamination process using solid layer method.

2.2.2 Experimental Setup for Data Acquisition of Surface Leakage Current (SLC)

An experimental arrangement was established to obtain information on the leakage current on several contaminated specimens' surfaces. The laboratory setup consists of a 3-ph, 50 Hz, 500 V/250 kV, 150 kVA testing transformer from which the high voltage is supplied to the test specimens. The Schematic diagram and actual hardware setup are illustrated in the Fig. 2.4 (a) as well as Fig. 2.4 (b).

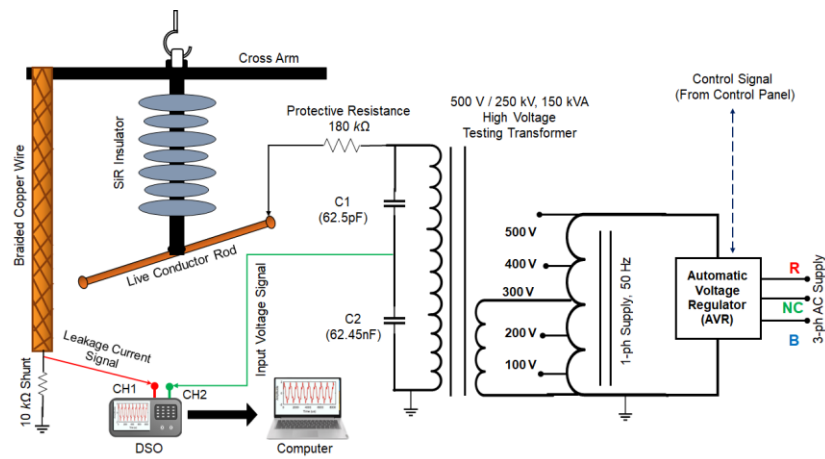


Fig 2.4 (a) Schematic diagram of Surface Leakage Current (SLC) data acquisition system.

Experimental setup for surface leakage current signature acquisition and procedure of artificially contaminated sample preparation



Fig. 2.4 (b) Actual Hardware setup for Surface Leakage Current (SLC) measuring system.

2.2.2.1 Major Components used in the Experimental Setup

This section discusses the significant hardware components used for surface leakage current measurement in the experimental setup. The major components are discussed below.

- **High Voltage (HV) Power Supply Arrangement**

An experimental setup was developed in the laboratory to measure surface leakage current data from contaminated overhead line insulator samples.



Fig. 2.5 (a) High Voltage on-load Voltage Regulator (VR).

A HV power arrangement of 3-phase, 50 Hz, 500 V/250 kV, 150 kVA provides the main power for the experiential setup. The HV power supply arrangement includes an on-load Voltage Regulator (VR), Auto-transformer and High Voltage Testing Transformer. Fig 2.5 (a), (b) and (c) show the high-voltage on-load Voltage Regulator (VR), Auto-transformer and HV testing transformer, respectively.



Fig. 2.5 (b) High Voltage Auto-transformer.



Fig. 2.5 (c) High Voltage Testing Transformer.

- **High Voltage Potential Divider**

This part of the experimental setup is also known as measuring unit. In this experimental setup high voltage potential divide was used to

Experimental setup for surface leakage current signature acquisition and procedure of artificially contaminated sample preparation

measure the system voltage in reduced level. According to Fig 2.4 (a), C_1 is a high-voltage capacitor with a rating of 62.5 pF. The image of C_1 is shown in Fig. 2.6. C_2 has been installed inside the control panel, and its value is 62.45 nF.



Fig. 2.6 High Voltage Potential Divider.

- **Control Room's Control Panel**

The input voltage is controlled through a control panel inside the control room. In the control panel, input voltage increments and decrements are maintained by push-button switches, as shown in Fig. 2.7 (a) and (b).



Fig. 2.7 (a) Image of Actual Control Panel.

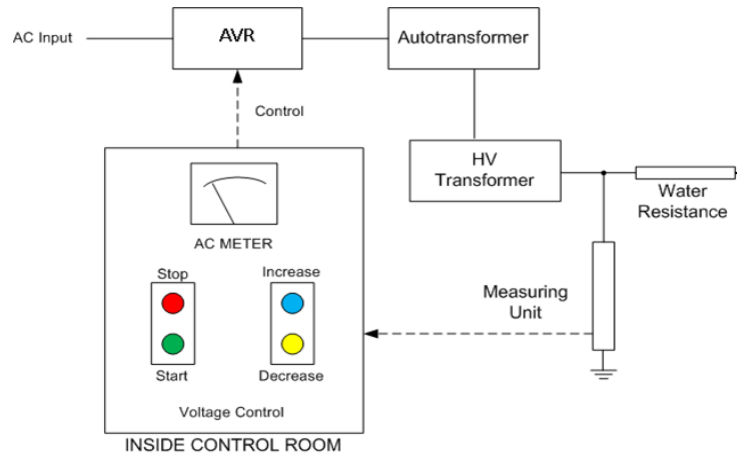


Fig. 2.7 (b) Schematic diagram of Actual Control Panel.

Also, the start and stop of power are controlled by dedicated “Start” and “Stop” push button switches. Various meters like voltmeter, Ammeter, energy meter and digital multimeter are also used to monitor different input parameters.

- **Water Resistance**

A $180\text{ k}\Omega$ protective resistor named water resistance (as shown in Fig. 2.8) has been connected in series to the experimental setup's high-voltage terminal. This arrangement provides short-circuit protection for the entire HV circuit. It contains distilled water which offers maximum resistance during normal operating conditions.



Fig. 2.8 Image of the Water Resistance.

- **Current Shunt and Digital Storage Oscilloscope (DSO)**

The path of surface leakage current is from the high-voltage terminal through the overhead line insulator's surface via the cross-arm towards the ground. A $10\text{ k}\Omega$ current shunt was used to obtain SLC

Experimental setup for surface leakage current signature acquisition and procedure of artificially contaminated sample preparation

signals. A current shunt connected to a protective circuit bypasses the DSO from inrush current flow during a flashover. The schematic and actual image of the current shunt is shown in Fig. 2.9 (a).

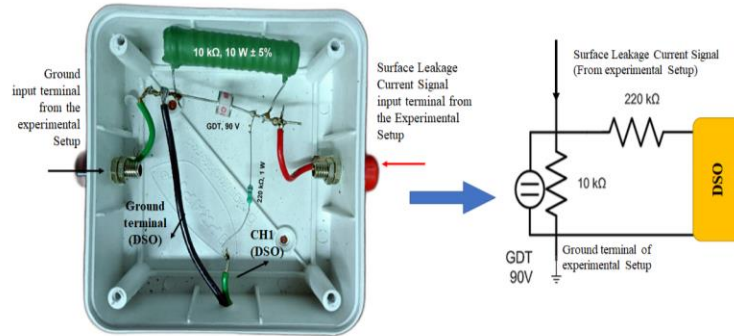


Fig. 2.9 (a) Pictures of Protective Current Shunt Circuit.

Similarly, a capacitor-based voltage divider was used to record the output voltage signature after the voltage level was stepped down in the laboratory. The voltage profile was monitored on a Digital Storage Oscilloscope (DSO), and data was recorded using a USB device.

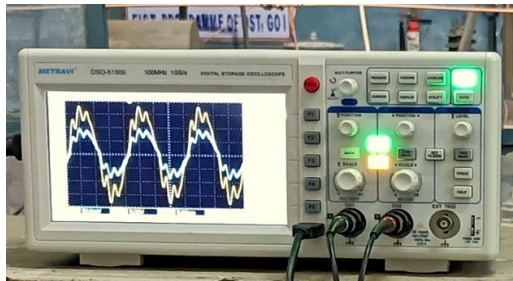


Fig. 2.9 (b) Image of Digital Storage Oscilloscope (DSO) during the SLC experiment.

Notably, the testing transformer's output characteristics are maintained by the standard described in [145], [148]. The output voltage signature was recorded using a Digital Storage Oscilloscope (DSO) after the stepped-down voltage level in the laboratory using a capacitor-based voltage divider as stated above. As illustrated in Fig. 2.4 (a) and Fig. 2.8, to protect the entire HV circuit from a short circuit, a 180 kΩ protective resistor has been connected in series to the experimental setup's high-voltage terminal. This protective resistance is called water resistance because it contains distilled water which provides maximum resistance during normal operating condition. The path of the surface leakage current is basically from the high-

voltage terminal through the surface of the overhead line insulator towards the ground. A 10 k Ω current shunt has been used to acquire the raw SLC data using DSO. In addition, a protective circuit is connected with a 10 k Ω current shunt to bypass the DSO from inrush current flow during flashover events. The components connected inside the protective circuit are illustrated in Table 2.2 and Fig 2.9 (a).

Table 2.2 Technical specification and function of current shunt protective device.

Connected Elements	Qty.	Specifications	Functions
Measuring Resistor	1	10 k Ω , 10 W \pm 5%	For measuring the Surface Leakage Current of the overhead line insulators.
Gas Discharge Tube (GDT)	1	90 V, 2 A	Limits the voltage level and protect the DSO from the over voltage event occurs.
Protective Resistor	1	220 k Ω , 1 W \pm 5%	To protect the DSO

From the above-mentioned setup, the surface leakage current of different levels of contaminated overhead line insulators was acquired by DSO and the sampling frequency of 50 kHz was maintained during data acquisition. During the SLC data acquisition process, transients were present in the early part of the SLC data. That part can generate analysis errors; For that reason, the initial portion of the SLC data was discarded and only the steady state portion of the SLC signal was considered for data analysis purposes. Aging, as well as high levels of contamination, play an essential role in changing the SLC profile of overhead line insulators. Therefore, field-aged overhead line insulator samples were used for data acquisition. Also, artificial contaminated slurries were prepared in the laboratory using the solid layer method on the surface of overhead line insulators. Finally, SLC signals for each pollutant class were measured for data analysis.

It is worth noting that during the SLC current measurement of each sample, the ambient temperature was also monitored. Also, each sample was repeatedly used for measuring SLC at different temperatures for precise data analysis.

2.2.2.2 Extraction of Surface Leakage Current (SLC) Signals and Input Voltage

Using the data-acquisition setup, as shown in Fig. 2.4 (a) and Fig. 2.4 (b), surface leakage current (SLC) signals were recorded for different pollutant classes. In this work, a total of 1500 SLC signals (300 signals per pollution level) were acquired at ambient temperature for five distinct contamination

Experimental setup for surface leakage current signature acquisition and procedure of artificially contaminated sample preparation

classes. According to the IEC 60815 standard, the contamination classes are very light, light, moderate, high and very high pollution [70], [147]. A detailed discussion regarding contamination categories, has been done in the following section. Fig. 2.10 (a) represents the surface leakage current (SLC) waveforms for five distinct contamination classes of overhead line insulators. With increasing surface contamination level of overhead line insulators, significant change on stationary behaviour is observed in the leakage current signature. It is worth noting that the SLC waveform at very low contamination contains less distortion than the SLC profile at very high contamination. The SLC signals were captured via DSO and then transferred to the computer via a USB device. To make a prediction regarding the contamination category of the overhead line insulator's samples, the recorded SLC data were employed for analysis. It is noteworthy that the system voltage profile for each contamination class was also monitored through DSO. In Fig. 2.6 (b), the waveforms of input voltage of each contamination category are illustrated.

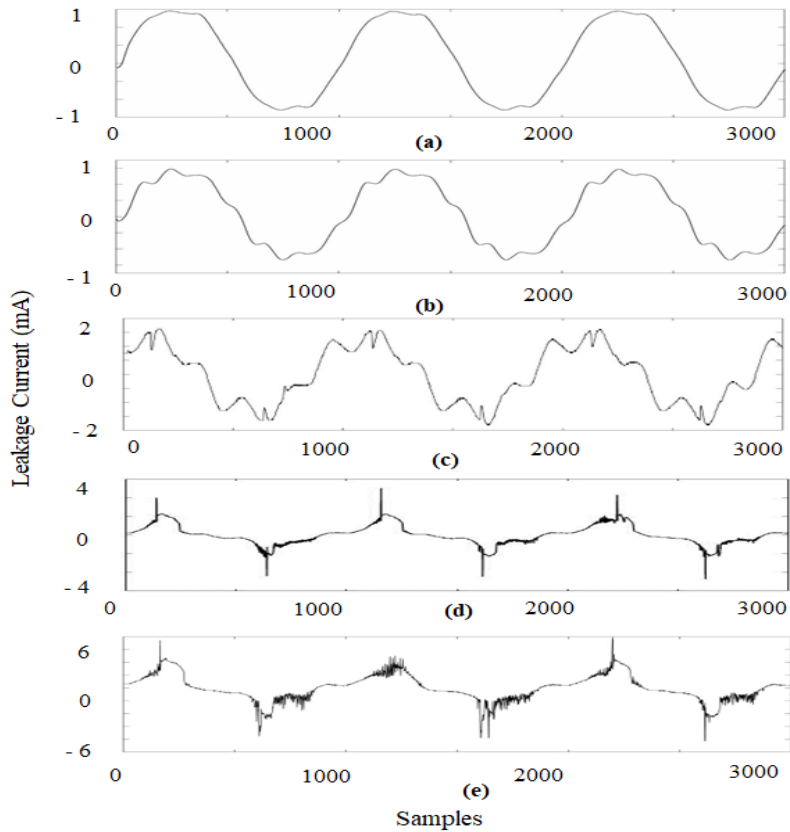


Fig. 2.10 (a) Waveform of acquired Surface Leakage Current (SLC) signals of five different classes of contamination such as (a) Very Light, (b) Light, (c) Moderate, (d) High and (e) Very High contamination.

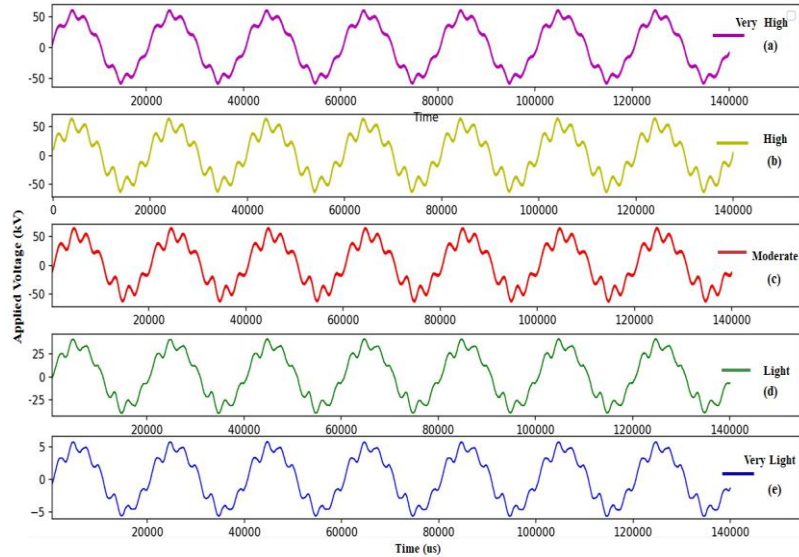


Fig. 2.10 (b) Waveform of input voltage profile of five different classes of contamination such as (a) Very High, (b) High, (c) Moderate, (d) Light and (e) Very Light contamination.

2.3 Estimation of Equivalent Salt Deposit Density (ESDD)

As stated in this chapter, the amount of $NaCl$ in artificially contaminated layers directly influences the surface conductivity of overhead line insulators. The Contamination level can be quantified using Equivalent Salt Deposit Density (ESDD) [7], [145]. For this reason, ESDD was measured after acquiring of SLC signals from various artificially contaminated samples. The authors followed the procedure illustrated in the IEC 60815 standard for estimating ESDD values from various artificially contaminated specimens [70], [147]. For this objective, the artificially contaminated coating was collected from the surface of different samples (as shown in Fig. 2.2). The collected coatings were then dissolved into the 100 ml distilled water and stirred for 1-2 minutes for better mixing. After that, at room temperature, the conductivity of the mixture was determined using the HANNA conductivity meter (HI-98188, EC/TDS/NaCl/Resistivity meter), as shown in Fig. 2.11.

Experimental setup for surface leakage current signature acquisition and procedure of artificially contaminated sample preparation



Fig. 2.11 Conductivity Meter (HANNA).

Then, the measured conductivity values were converted at 20°C temperature's equivalent value using the following expression for each sample [7], [145].

$$\sigma_{20} = \sigma_{\theta} [1 - p(\theta_i - 20)] \quad (2.1)$$

Where, σ_{20} is mean volume conductivity at 20°C (S/m), σ_{θ} is mean volume conductivity at θ_i °C (S/m), θ_i is ambient temperature, and p is a factor that changes with the solution's temperature. The mathematical formulation of factor p has been expressed in following equation [7], [144] – [145].

$$p = [(-3.2 \times 10^{-8} \times \theta_i^3) + (1.032 \times 10^{-5} \times \theta_i^2) - (8.272 \times 10^{-4} \times \theta_i) + (3.544 \times 10^{-2})] \quad (2.2)$$

Next, the salinity (S_a) of the coating layer of the insulator sample were evaluated using the given equation [7], [144] – [145]:

$$S_a = [5.7 \times \sigma_{20}]^{1.03} = [5.7 \times \sigma_{20} \times 10^{-4}]^{1.03} \quad (2.3)$$

Based on the aforesaid equation (2.3), The following formula was used to estimate the Equivalent Salt Deposit Density, or ESDD (mg/cm²) [145]:

$$ESDD = \left(\frac{S_a \times V}{A_a} \right) \quad (2.4)$$

Where, V = volume of the solution (cm³), A_a = area of the contaminated insulator (cm²) and S_a = salinity of the coating of the overhead line insulators (S/m). In this study, several surface contamination samples of overhead line insulators were created by adjusting the *NaCl* and Kaolin concentration ratio. It has been reported that the range of ESDD values varied from 0 to 0.4 for different classes of contamination [145], [146]. According to the calculated value of ESDD, the five different contamination classes have been

segmented. In Table 2.3, the range of ESDD values corresponding to different surface contamination severity has been shown.

Table 2.3 Classification of contamination level based on ESDD range and amount of *NaCl* salt.

Level of Contamination	Amount of <i>NaCl</i> (gm)	ESDD Range (mg/cm ²)	Contamination Class
CL-1	0.05	0 – 0.08	Very light (VL)
CL-2	0.25	0.08 – 0.16	Light (L)
CL-3	0.42	0.16 – 0.24	Medium (M)
CL-4	0.91	0.24 – 0.32	High (H)
CL-5	1.74	> 0.32	Very High (VH)

2.4 Conclusion

In this chapter, surface leakage current signals for five types of contaminated classes of overhead line insulators were acquired using a developed hardware model. The important points of this chapter are summarized as follows:

- The hardware developed was a simulated model of the overhead line and it is an effective and fast data acquisition system.
- The method for the preparation of artificially contaminated samples is simple. During sample preparation, IEC 60815 standards were followed.
- According to IEC 60507 standards, leakage current measurement was performed. The raw data acquired from the hardware setup was stored in excel format for further investigation.

The proposed experimental setup helps to record the surface leakage current, which provides essential knowledge about the health status of overhead line insulators. During the SLC measurement, the system voltage profile was monitored. It is noteworthy that significant changes in the SLC waveform were observed due to the increase in surface contamination levels. But in the input voltage profile, no such change was observed. The SLC signals can be used to exactly identify the contamination classes of outdoor insulators. This analytical review can further assess the life expectancy of the overhead line insulators. In this regard, a detailed discussion has been carried out in the following chapters.

Chapter 3

Mathematical Morphology Aided Random Forest Classifier Based Contamination Level Prediction of Overhead Transmission Line Insulator

3.1 Introduction

Overhead line insulators are an essential part of transmission and distribution lines. They provide mechanical support and insulation of overhead transmission lines. Overhead line insulators are contaminated mainly due to geographical location. Environmental pollutants contaminate the surface of any overhead line insulator. Mainly, Sodium chloride ($NaCl$) and kaolin ($Al Si_2O_5(OH)_4$) damage the housing of overhead line insulators in coastal and tropical rainforest areas, respectively. Apart from the mentioned factors, other factors such as fog, rain, ocean sand, dust, soil and air pollution mainly erode the outer perimeter of the overhead line insulators. Primarily, the mixture of water droplets and contaminants changes the surface conductivity of the overhead insulators. As a result, surface leakage current (SLC) begins to flow, from which a non-uniform voltage distribution appears throughout the insulator surface. Localized dry bands appear on the insulator's surface because of the SLC's exponential growth. As a result, the above-mentioned cumulative effects may lead to flashover and a complete breakdown of overhead line insulators [31], [142] – [143]. Therefore, the measurement of surface leakage current (SLC), as well as the analysis of the SLC data, is the essential parameter to investigate the surface condition of overhead line insulators. To analyze the nonlinearity of SLC signals, mathematical morphology is the most suitable tool in comparison to other time domain analyses like Fourier transforms (FT), Short Time Fourier Transform (STFT), Wavelet Transforms (WT) and harmonic analysis [144] – [145], [150]. The cause of the nonlinearity that affects the SLC signal's signature cannot be determined directly by aforesaid time domain techniques. In contrast, Mathematical morphology is the most effective and efficient tool [153] – [154]. It can help to detect small changes in the SLC signal due to overhead line insulators' surface contamination. Because of the above reasons, the mathematical morphology tool was used in this study.

In this work, 11 kV_{rms} rated porcelain insulator discs were used to investigate the surface conditions. In this regard, the SLC signal was acquired using a hardware setup for different contamination classes. Chapter 2 (section 2.2.1) provides a detailed discussion regarding the experimental setup. The same setup was used to acquire the SLC data from different samples, in this work. The acquired data was further utilized for analyzing the surface condition of the porcelain insulator disc. According to the artificial contamination guidelines i.e., IEC 60507, five different contamination classes

were artificially prepared in the laboratory and corresponding surface leakage current was measured for each contamination class [7], [124]. After all leakage current data were acquired, these data were fed to a mathematical morphology tool to extract the most significant features. The insignificant features were eliminated using a proposed filter algorithm from the acquired feature matrix. Then, the sorted features were further utilized to detect the surface contamination stages of porcelain insulators using a machine learning classifier (i.e., Random Forest (RF)). In addition, the precision level of the classifier was reported. A detailed explanation of the proposed methodology has been discussed in the following sections.

3.2 Classification of Artificial Surface Contamination of Porcelain Insulators

In this work, the disc of porcelain insulators was employed to assess the severity of the contamination of overhead line insulators. The development of distinct artificial surface contamination samples in accordance with IEC 60507 standards is the primary requirement [7]. It is noteworthy that collecting in-field outdoor insulators with various surface contamination severity is challenging. Therefore, the artificial contamination method makes it relatively simple to develop surface-contamination of outdoor insulators in the laboratory. For this reason, a few outdoor porcelain disc insulator specimens were used to measure the SLC. An 11 kV_{rms} rated porcelain insulator disc was used in this study to investigate the insulator's housing condition. In chapter 1, Table 1.3 illustrates the detailed technical properties of 11kV porcelain insulator disc.

In this work, the solid layer method (SLM) has been utilized to contaminate the exterior of the outdoor insulators sample [145] – [146]. It is possible to create an artificial contaminated layer over the surface of an outdoor insulator sample using the SLM. To prepare the slurry in SLM, kaolin ($AlSi_2O_5(OH)_4$), salt, and distilled water were utilized. It is notable, the mixture of salt and Kaolin ($AlSi_2O_5(OH)_4$) is utilized as conductive and non-conductive materials in this slurry, respectively. In this study, samples of overhead line insulators were coated at room temperature and allowed to dry for at least 24 hours. It was reported that natural contamination is primarily caused by salts like $NaCl$ and KCl [146]. Because of this, $NaCl$ is selected as the primary component for preparing artificially contaminated slurry and the $NaCl$'s quality directly controls the conductivity of the contaminated slurry [7]. Fig. 3.1 shows a picture of a porcelain disc insulator sample artificially contaminated for SLC experimentation. Based on the range of equivalent salt deposited density or ESDD and the amount of $NaCl$ are utilized in artificial contamination samples to categorize the degree of contamination, in this work [7], [146]. The proportional change in ESDD value, along with $NaCl$ quality, is used to classify outdoor insulators' surface contamination level. The detailed description has already been illustrated in Table 2.3 (in Chapter 2, section 2.3). Moreover, in Chapter 2 (section 2.2.1), the procedure for making artificial surface contamination is briefly discussed.



Fig. 3.1 Photography of artificially surface contaminated and uncontaminated porcelain insulators.

3.3 Surface Leakage Current Signals Acquisition Setup

A laboratory experimental setup was built to record surface leakage current data from various contaminated samples. The high voltage is supplied to test specimens by a transformer with the following specifications: 1- ϕ , 50 Hz, 500 V / 250 kV, and 150 kVA. The real hardware configuration schematic diagram has already been reported in Chapter 2 (i.e., Section 2.2.2, Fig. 2.4 (a) and 2.4 (b)). In compliance with the standard [148], the testing transformer's output characteristics have been maintained. By stepping down the voltage through a capacitive voltage divider, the output voltage has been recorded on a digital oscilloscope (DSO). In order to prevent high current flow during an accidental fault, Between the test sample and the terminal of the high voltage experimental transformer, there is a protective resistance of 180 k Ω . Using a digital oscilloscope (DSO), it is possible to measure the leakage current flowing through the sample via 10 k Ω (i.e., Chapter 2, section 2.2.2, Fig. 2.4 (a) and 2.4 (b)). In [145], [150], the procedure of surface leakage current data acquisition for each artificial contamination samples are briefly discussed.

3.3.1 Effect of Contamination Severity on Surface Leakage Current Signal

In this work, the surface leakage current (SLC) was acquired from the experimental setup for each class of contaminated samples. In the process of acquiring SLC data, the sampling frequency was maintained 50 kHz. The measured SLC data was stored using DSO and then the data was transferred to the computer via USB device. The complete ESDD calculation steps are presented in the previous chapter 2 (i.e., section 2.2.2.2).

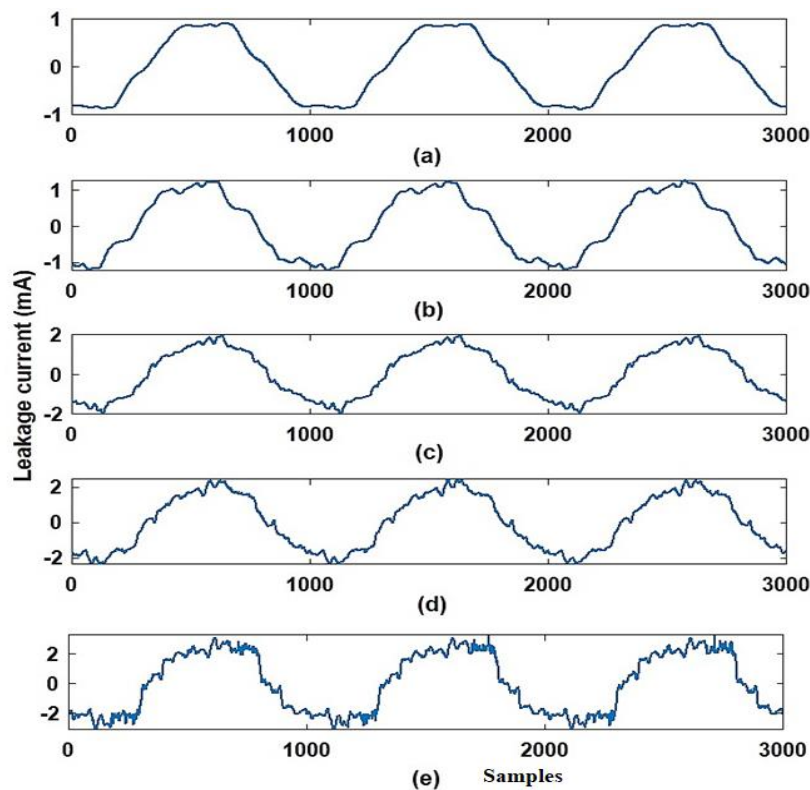


Fig 3.2 The waveform of the acquired Surface Leakage Current (SLC) signals representing five distinct categories of contamination, including (a) Very Light, (b) Light, (c) Moderate, (d) High, and (e) Extremely High.

It is found that the nature of the SLC waveforms is also distorted due to high pollution levels. For each contamination level of this present work, 600 samples were recorded from the leakage current signal and a total of 3000 leakage current signals samples were acquired. For each category of contamination, the waveforms of SLC are illustrated in Fig 3.2.

3.4 Features Extraction from Surface Leakage Current Signal

After achieving surface leakage current data, complete data has been analyzed on the MATLAB platform. In this work, an advanced frequency signal conditioning method, i.e., mathematical morphology (MM), was used to extract features from the leakage current signal of the surface. The MM function can provide satisfactory consequences regarding the power system, sound filtering and real-time signal processing.

3.4.1 Fundamental Concept of Mathematical Morphology

Mathematical Morphology (MM) is a set theory-based time domain analysis. It is preferred for nonlinear time signal analysis. Serra and Matheron have first introduced the MM technique [151], [154]. MM is advanced signal processing tool. It solely performs within the time domain signal. In addition, it is utilized for image as well as time domain signal de-noising. It is noteworthy that with the help of mathematical morphology, the complex input signal can be split into various sub-signals, including different physical significance. From there most suitable features are achieved. An essential aspect of the morphological filter is the Structural Element (SE) function, which regulates the shape of the input time domain signal as well as eliminates the noise from the input signal [153]. The signal's characteristics determine whether the SE is discrete or continuous. Structure Element (SE) dimensions and shapes are determined by the input signal's sampling frequency and geometrical characteristics [151], [155]. In addition, this SE assists to drag features from the input signal. In this case, linear SE is an appropriate selection to pull out essential features from SLC signals of overhead line insulators.

3.4.2 Extracted Features after Mathematical Morphology Operation

It is possible to perform several mathematical operations in mathematical morphology, including the four basic morphological operators for single-dimensional signals: dilation, erosion, opening, and closing. The definitions of the above-mentioned terminology and the mathematical expression are described as follow:

Let, the 1D time domain input signal is $p(j)$ with the dimension of the signal is $P = (0, 1, 2, \dots, j-1)$. The Structure Element (SE) $s(k)$ is discrete and linear and expressed as $S = (0, 1, 2, \dots, k-1)$, where $(j > k)$ and j and k are represented as integer. Therefore, the expression of Dilation $D(j)$ of input signal $p(j)$ by SE $s(k)$ can be written as:

$$D(j) = [p \oplus s](j) = \max \left\{ \begin{array}{l} p(j-k) - s(k) \\ [0 \leq (j-k) \leq j, k \geq 0] \end{array} \right\} \quad (3.1)$$

Similarly, the Erosion $E(j)$ of the given input signal $p(j)$ by SE $s(k)$ can be defined as:

$$E(j) = [p \ominus s](j) = \min \left\{ \begin{array}{l} p(j+k) - s(k) \\ [0 \leq (j+k) \leq j, k \geq 0] \end{array} \right\} \quad (3.2)$$

Generally, dilation makes any sharp deviation in the signal's boundary bigger, whereas erosion makes a signal's outline smaller [153]. In addition, sharp edges are converted into smooth boundary by opening operation. Similarly, narrow gaps present in any signal are filled up by closing operation. The opening operation of any input signal $O(j)$ can be identified as an increase in decaying signals. In contrast, the closing operation of any input signal $C(j)$ can be described as shrinking of the stretch signal. The mathematical expression of opening operation of the input signal $p(j)$ by $s(k)$ is illustrated as:

$$O(j) = (p \circ s)(j) = [(p \ominus s) \oplus s](j) \quad (3.3)$$

Similarly, the mathematical expression of closing operation of the input signal $p(j)$ by $s(k)$ is:

$$C(j) = (p \bullet s)(j) = [(p \oplus s) \ominus s](j) \quad (3.4)$$

Apart from this, two hybrid functions have been presented in this work employing the MM operator. These are the *Dilation Erosion Difference* $\partial X_{DE}(j)$ and the *Opening Closing Difference* $\partial Y_{OC}(j)$ operators. The opening-closing difference operator derives from the discrepancy between opening and closing signals, whereas the dilation-erosion difference operator is the dissimilarity between dilated and eroded signals. The mathematical equations of the above-mentioned terminology are presented below.

$$\partial X_{DE}(j) = [p \oplus s](j) - [p \ominus s](j) \quad (3.5)$$

$$\partial Y_{OC}(j) = [p \circ s](j) - [p \bullet s](j) \quad (3.6)$$

A total of 20 features have been extracted using the proposed MM operator. In the feature extraction process, SE has been utilized to extract the most significant features from the input SLC of overhead line insulators. It is important to note that the selected dimensions SE are perfectly suited for analyzing a leakage current signal in the 1D time domain. The current study uses $s(k) = [1 \ 0 \ 1]$ as the structure element (SE). As shown in Table 3.1, the name of extracted MM features (F_1 to F_{20}).

Table 3.1 Features Description.

Name of Features	Description
F_1	Variance of $D(j)$
F_2	Variance of $E(j)$
F_3	Variance of $O(j)$
F_4	Variance of $C(j)$
F_5	Variance of $\delta X_{DE}(j)$
F_6	Variance of $\delta X_{OC}(j)$
F_7	Kurtosis of $D(j)$
F_8	Kurtosis of $E(j)$
F_9	Kurtosis of $O(j)$
F_{10}	Kurtosis of $C(j)$
F_{11}	Kurtosis of $\delta X_{DE}(j)$
F_{12}	Kurtosis of $\delta X_{OC}(j)$
F_{13}	Skewness of $D(j)$
F_{14}	Skewness of $E(j)$
F_{15}	Skewness of $O(j)$
F_{16}	Skewness of $C(j)$
F_{17}	Skewness of $\delta X_{DE}(j)$
F_{18}	Skewness of $\delta X_{OC}(j)$
F_{19}	Average of dilated signal $D_{avg}(j)$
F_{20}	Average of eroded signal $E_{avg}(j)$

3.5 Procedure of Features Classification

A forecast for the lifespan of overhead line insulators relies heavily on the classification of features. Features selection is the prior function of feature classification. After MM operation, features must be filtered to obtain accurate outcomes. A feature classification procedure can be divided into two categories. First, feature reduction using the filter method and, second, prediction of contamination classes using a machine learning classifier. The detailed description of the aforesaid methods is described in the following sections.

3.5.1 Feature Selection using Filter Method

In this work, five different classes of contaminated porcelain insulators samples were used for the SLC data acquisition. After using the MM operation, 20 numbers of features were achieved and those features carried

vital information regarding contamination classes. The size of the acquired features matrix is (20×25) . Acquired features are illustrated in the Table 3.2. Moreover, the acquired feature matrix is displayed in a compact arrangement in the following Table 3.2.

Table 3.2 Acquired Features after Mathematical Morphology operation.

Contamination Classes	Acquired Features				
	F_1	F_2	F_3	--	F_{20}
Very Light	1.003	-1.003	1.525	--	101.483
	0.993	-1.013	1.525	--	101.587
	---	---	---	--	---
Light	1.004	-1.008	1.516	--	89.109
	1.007	-1.006	1.511	--	88.952
	---	---	---	--	---
Moderate	1.008	-1.006	1.521	--	96.788
	1.007	-1.007	1.531	--	96.501
	---	---	---	--	---
High	1.005	-1.006	1.417	--	107.946
	1.004	-1.007	1.440	--	-0.7884
	---	---	---	--	---
Very High	1.091	-0.930	1.376	--	140.498
	1.059	-0.960	1.500	--	136.197
	---	---	---	--	---

The proposed filter method is utilized in this work for feature reduction and selection purposes. Using this method, the most significant features were selected and undesirable and constant features were eliminated. This method is used to increase feature sorting precision. The Python software platform was employed to perform the entire filter method. The steps of filter method are discussed below.

In the first phase of the filter method, constant features are removed from the available features matrix. Three primary conditions help to eliminate constant features. Only features that meet the following conditions are used in the next stage. The conditions are:

- All features that had constant value were eliminated.
- It removed those features whose variance marginal value was below 0.01.
- A constant value feature was removed from two consecutive features in the available features set.

A cross-correlation operation on the residual features was performed in the subsequent stage to assist in identifying significant features and eliminating undesirable ones. After the cross-correlation operation, the acquired features

were allotted to different groups according to their similarity. It is noteworthy that this grouping operation helps to improve the features' classification accuracy. As a result, the computational burden on the classifier model can be reduced. To remove undesirable features, a marginal value of the cross-correlation was assigned in this work, i.e., greater than and equal to 0.9. Apart from this, only features that properly pass the marginal value of the cross-correlation were chosen. The outcome of the conditional loop (as shown in Fig. 3.3) provides suitable features for both true and false conditions. After the loop conditions were satisfied, the obtained features were again tested with the help of the three aforementioned conditions. This was done to eliminate unwanted features from the residue. Significantly, after examining the various conditions for feature extraction in the filter method, the residue features were fed to a machine-learning classifier. The flowchart of the filter method is illustrated in the Fig. 3.3. It is noteworthy that the Random Forest (RF) classifier was used for the purpose of features classification. The following section discusses the details of the feature classification process using RF classifier.

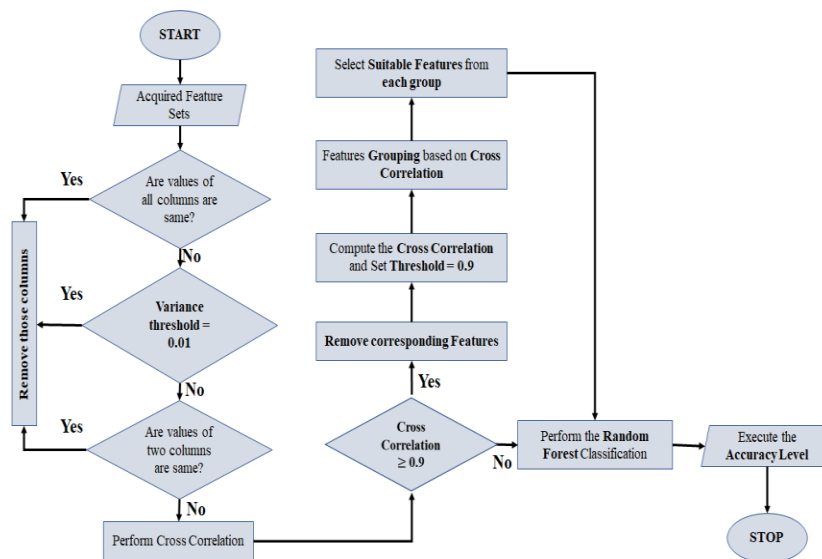


Fig. 3.3 Infographics of the Filter Method.

3.5.2 Features Classification using Random Forest (RF) Classifier

In this study, features were extracted by a mathematical morphology tool from raw SLC data. After that, the extracted features were sent to a filter model to select suitable features. After picking significant features, the sorted features were fed to a well-known machine learning classifier (i.e., Random Forest (RF)) for feature classification. To identify significant contamination

classes on overhead line insulators, classification features are used. It is noteworthy to mention that the overall acquired dataset has been divided into two parts: the training data set and the testing dataset. In this case, 75 % of the overall data was determined for training and the remaining 25 % was used for testing. A broad discussion about the working strategy of random forest (RF) classifier is stated below.

3.5.2.1 Working Strategy of Random Forest (RF) Classifier

A machine learning classifier for classification algorithm called random forest (RF) was developed by Briemen [156]. An enormous number of independent decision tree classifiers work together in RF. All these decision tree classifiers combined voted to make the final decision in RF [156] – [158]. The working procedure of the RF classifier is categorized into three stages. The detailed procedure of an RF-based classifier is described below.

Initially, according to the available input dataset, several numbers of decision trees are created. The number of decision trees varies according to the input dataset. The training operation is performed on individual decision trees. From this process, each of the decision trees can work as base classifiers. It is important to mention here each base classifiers have been trained using random sample with repetition during the training period. In order to obtain optimal training results, repetition of the random data is controlled, so that it contributes roughly one-third of the training dataset. The random data that are supplied to each base classifier are referred to as *in-bag data* and the preceding process is referred to as *bagging*. Notably, roughly $\frac{2}{3}$ of the training data have been used to teach each base classifier. It has been observed that the training precision of the created decision tree can be validated using the remaining data, called *out-of-bag* data [156] – [158].

In the next stage, Once the *in-bag* dataset has been finalized, decision tree construction begins. During the construction of the decision tree, a feature (attribute) is chosen at the root node. The training data is then divided into subsets for each attribute's possible value [157]. This creates a branch for each feature's possible value. A split feature resulted in an increase in information, which was then used to select the root node. In this regard, root nodes have been defined as features that provide maximum information gain [157]. As per the operation of RF, the information gain (I_{gn}) helps to divide the training dataset (T_s) into various subsets (T_{S_i}). The mathematical expression of information gain (I_{gn}) is represented as [157]:

$$I_{gn} = - \sum_{i=1} \left| \frac{T_{S_i}}{T_s} \right| \times E_n(T_{S_i}) \quad (3.7)$$

Where, the entropy of the training sub-dataset (T_{S_i}) is expressed as [157]:

$$E_n(T_{S_i}) = -\sum_{j=1}^{n_s} S_{p_{j\pm}} \log_2(S_{p_{j\pm}}) \quad (3.8)$$

Assume that n_s denotes the number of sleep stages and $(S_{p_{j\pm}})$ denotes the number of the j^{th} sleep stage in the training subset (T_{S_i}). In the case of positive I_{gn} , the node has divided, otherwise it remains unchanged and becomes a leaf node [157]. Features are collected based on the highest information gain's value (I_{gn}) of residual features. Until features are chosen, the splitting process continues [157] – [158]. It is noteworthy to mention that the splitting function continues until all features are chosen [157].

Finally, in the final round, all trees were grouped and a vote was taken based on the decisions made by all trees. In addition, the final decision is considered based on the maximum number of votes [156] – [158]. The schematic diagram of the random forest (RF) operation is depicted in Fig. 3.4.

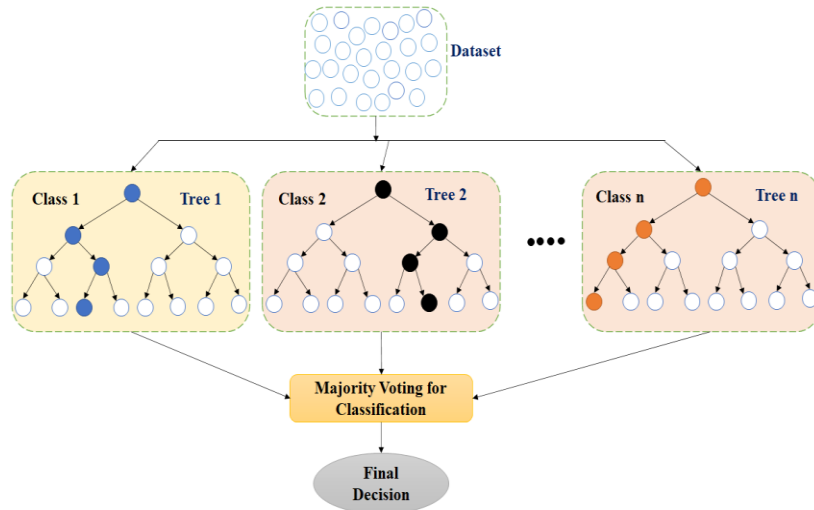


Fig. 3.4 Schematic of Random Forest Classifier.

3.6 Results and Discussions

In this work, in-service overhead line insulators have been selected to determine their contamination level using surface leakage current data. According to the IEC standard (i.e., IEC 60507), artificially contaminated surfaces of insulating samples in the laboratory were prepared. With the help of the laboratory-made simulated transmission line model, the surface leakage current data was measured. The stored SLC data was further analyzed in the software platform. Therefore, the acquired data was tested using

mathematical morphology to extract the significant features and 20 features were extracted from this method. It is noteworthy that feature selection was performed with the help of the filter method. At the end of the filter method, achieved optimal features were fed to one machine learning classifier (i.e., random forest) and from there, contamination classes were identified.

In this work, features were selected using various method combinations and each feature class precision level was tested via an RF classifier. The combination of the feature classes is shown in Table 3.3. According to Table 3.3 reports four types of feature classification combinations based on the available extracted features set. The accuracy of every stage of the feature classification process was tested using an RF classifier and is reported in Table 3.3. Some noticeable outcomes have been observed in this stage, which has been reported below.

- By using only mathematical morphology operation model was able to execute 20 numbers of unique features set. The related accuracy measurement has been reported in the Table 3.3 by using classification technique.
- After removing redundant features, the most optimal features were achieved using feature removal without the correlation method. After this stage, a total of 11 sets of features were extracted.
- It is significant to mention that only three sets of features were achieved using the cross-correlation and redundant feature-removal operation (as reported in Table 3.3).
- Lastly, with the help of cross-correlation and grouping operations on the residual features, five sets of features were executed at the end of the filter method.

As shown in Table 3.3, the corresponding accuracy is reported at every step of the classification procedure.

Table 3.3 Result of Filter Methodology.

Classifier	Accuracy (%)			
	Random Forest	Extracted features from Mathematical Morphology operation (20 sets of features)	Removing the constant features and without Correlation (11 sets of features)	After performing Cross-correlation and without grouping (3 sets of features)
	95	95	95.3	95.6

3.7 Conclusion

Initially, the porcelain insulator disc surface was created to be artificially contaminated as per the IEC standard. Then, the leakage current (LC) was measured and recorded in the laboratory with an experimental setup. Subsequently, the recorded surface LC data was used to extract features using a mathematical morphology technique and filter model. Notably, the most appropriate features were selected using the filter method. The extracted features were further fed to a machine learning classifier for porcelain insulator contamination class prediction with extracted features. For the feature classification, a random forest classifier was used in this work. Corresponding accuracy for predicting contamination using classification techniques is also reported in this chapter. In this chapter, the following conclusions have been drawn as follows:

- There are several advantages to the proposed framework, including its simplicity, speed, accuracy, and robustness.
- The proposed framework achieves acceptable accuracy under different combination of features classes. In addition, the accuracy level was tested individually for each class of feature set.
- The filter method helps reduce the unnecessary features from the large feature set. It is an efficient and uncomplicated technique. In addition, it is referred to as the feature reduction method. The outcomes of the filter method provide optimal features for feature classification, which boost the classification accuracy.
- There is no impact on the classification performance of the suggested framework if voltage fluctuations are within an acceptable range.

It is essential to mention that this proposed methodology will help identify the overhead line insulators' surface contamination using the SLC analysis to avoid the failure of the overhead line insulators.

Using this proposed filter model and Mathematical Morphology operation, acquiring features from the SLC signal is cumbersome and time-consuming. Apart from this, with the help of mathematical morphological signal processing filter features were extracted from SLC signals. The operation of the mathematical morphological technique depends on structural element dimensions. Assigning structural elements depends on the input signal signature, which is the trickiest. In addition, the proposed model's success rate was examined with only one machine learning classifier (i.e., Random Forest). Testing the model's performance by one classifier may not provide a precise prediction of surface contamination of overhead line insulators. Due to the aforesaid limitations, a joint time-frequency signal processing framework has been implemented on the SLC signals and a detailed discussion has been reported in the next chapter. In addition, different types of machine-learning classifiers have been used to test the new framework's precision level.

Chapter 4

Condition Assessment of Overhead Line Silicone Rubber Insulators by Employing Surface Leakage Current Signal and Hyperbolic Stockwell Window Transform

4.1 Introduction

In *Chapter 3*, a proposed framework was developed with the help of a mathematical morphological signal processing filter. It is a nonlinear signal transformation technique used in feature extraction from surface leakage current signals. The basis of this technique depends on structural element dimensions. However, the main drawback of this technique is that its performance changes with the characteristics of the input signal, since the structural element's dimension solely depends on the input signal's nature. Apart from this, assigning new structural elements to update the input dataset is cumbersome and time-consuming. In the previous chapter, the proposed framework's performance was tested only with a random forest classifier, which may not be able to provide a precise prediction to identify the degree of surface contamination of overhead line insulators. Therefore, it is essential to compare the proposed model's performance with other classifiers to predict the contamination class of overhead line insulators with the utmost accuracy.

In this proposed framework, the Silicone Rubber (SiR) insulator samples were taken for surface leakage current measurement. It is noteworthy to mention that in the recent scenario, Silicone Rubber (SiR) insulators play essential roles in reliable power flow from power generation to the consumer end. It has to be mentioned here that one of the significant reasons behind power outages is the breakdown of overhead transmission line insulators [159] – [160]. These overhead line insulators have been preferred over ceramic and glass insulators for the last two decades because of their lightweight, self-restoring hydrophobicity properties, better pollution performance etc [161] – [162]. Despite the benefits mentioned above, the surface of SiR insulators is more affected by environmental pollutants than ceramic insulators. Due to the impurity mixing in the SiR insulator housing, it experiences uneven voltage distribution and thermal imbalance on the SiR insulators' surface. The flashover event is also noticed, followed by their complete breakdown. It is entirely undesirable from the power system and countries' economic perspectives. It is noteworthy to mention that due to the rapid growth of the contamination level on the surface of overhead line insulators, frequent failure of insulators has been observed. That is why it is challenging and necessary for engineers to investigate the overhead line insulators' condition regularly.

To monitor the surface condition of SiR insulators, different parameters such as equivalent salt deposit density (ESDD), air pollution condition, and surface leakage current monitoring have been advised over the years [68]. It is noteworthy that calculating ESDD can provide a closer view of the surface condition of the SiR insulator. However, the applicability of ESDD process is not feasible due to the time-consuming process and facing some practical constraints [31], [150]. Thus, surface leakage current analysis has been widely accepted as a convenient and reliable technique for the assessment of overhead line insulators' surface condition [144] – [146], [150]. As stated in [144], the third and fifth harmonic content ratio of the surface leakage current can be a marker of the insulator surface condition. The major limitation of the aforesaid techniques is that they depend on the input voltage signature. It has also been found that the change in supply voltage profiles due to the fluctuating load demands [160]. In addition, regular monitoring of voltage from high voltage side is very problematic and costly.

It has been revealed in [145] – [146] that, the deviation of the surface contamination level is the main cause behind the nonlinearity of the surface leakage current's signature [145] – [146]. It is noteworthy to mention that the SLC signature is not stationary in nature. Non-stationary is incorporated into the SLC profile due to artificial surface contamination of overhead line insulators. Besides that, the distortion levels in the SLC's signature are higher at a higher level of surface contamination. Notably, few observable sharp impulse peaks appear at irregular intervals in the SLC waveforms, as shown in Fig. 4.1. They are predominant at higher contamination levels in comparison with lower levels of surface contamination. The reason for appearing the irregular patterns on the SLC waveform is due to the surface discharge phenomenon. Notably, the surface discharge happens because of surface contamination and the continuous flow of the SLC on the surface of overhead line insulators. For this reason, the irregular partial arc incorporates non-stationary in time-varying SLC signals [143]. Therefore, the Fast Fourier transform (FFT) analysis is ineffective for determining the non-stationary profile of the time-varying input signals. Moreover, FFT analysis allows examining the harmonic profile of stationary signals [146]. In this regard, FFT analysis cannot provide precise information after analyzing odd harmonic components from leakage current signals of overhead line insulators [144]. Apart from this, non-stationary signals do not adhere to the linearity assumption, as they can exhibit interactions and coupling between different frequency components that violate the principles of superposition. A non-stationary signal, such as SLC signals from overhead line insulators, may generate new frequency components due to the interaction between the original signals and noise signals. FFT analysis may not accurately capture these additional frequency components, leading to inaccurate frequency domain representations of the input signals [165].

Additionally, the FFT may not adequately resolve non-stationary SLC signals with rapidly changing frequency components concerning the surface contamination variation or fine-scale details of the SLC signals, leading to a loss of information. Due to surface discharge and surface contamination, SLC signals can produce complex frequency spectra with a mixture of harmonics,

Condition Assessment of Overhead Line Silicone Rubber Insulators by employing Surface Leakage Current Signal and Hyperbolic Stockwell Window Transform

subharmonics, and other components. Therefore, it is challenging to interpret using traditional FFT techniques to identify the complex frequency spectra of SLC signals. Due to the limitations, the non-stationary signal processing tool, i.e., mathematical morphology, has been applied to the time-varying non-linear SLC signals to extract the relevant features. Moreover, using mathematical morphology, complex and non-linear time-varying SLC signals can be split into various sub-signals, including their different physical significance [153]. This signal processing tool can easily identify irregular changes in the waveform of SLC signals due to the surface contamination of overhead line insulators. In contrast, the operation of the mathematical morphological technique depends on structural element dimensions. Besides that, assigning structural elements depends on the signature of input signal, which is the trickiest. Therefore, only the time domain analysis methods are not effective in investigating the surface status of the overhead line insulators.

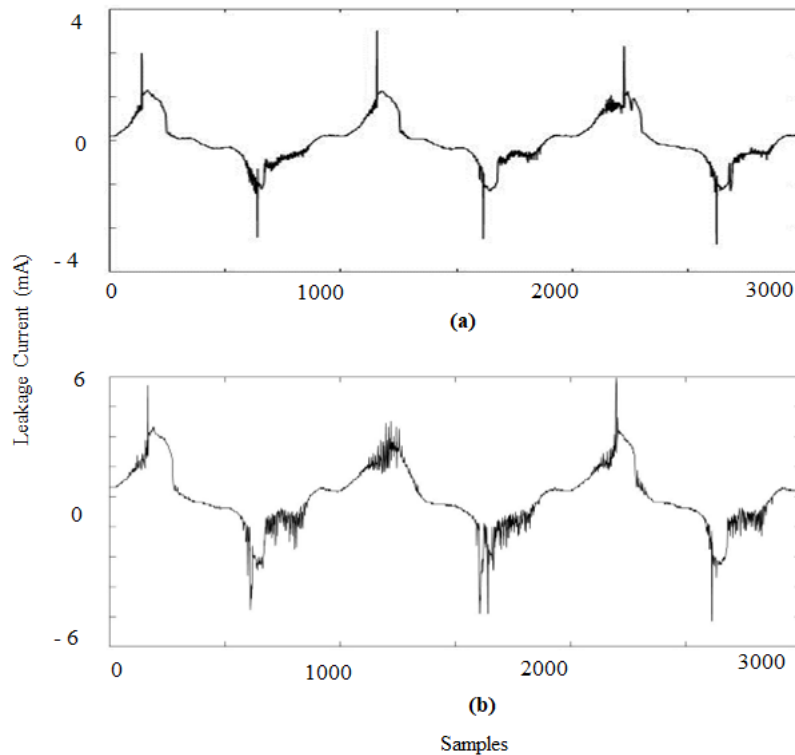


Fig. 4.1 Waveforms of surface leakage current signal for (a) High and (b) Extremely high contamination level.

With the help of SLC signal analysis in the time-frequency domain, overhead line insulators can be monitored more effectively. For the last two decades, the Stockwell Transform (ST) is very well known for analysing the

non-stationary signals in the time-frequency domain [165] – [170]. The advantage of the Stockwell transforms over the Short Time Fourier transform (STFT) and Wavelet Transform (WT) is mainly the determination of the phase information at each frequency and shows better performance with the presence of noise [165] – [170]. There have been many studies demonstrating the effectiveness of the Stockwell transform in biomedical engineering for EEG signal processing [166] – [167], power quality detection [168], gearbox fault analysis [169], and power transformer fault analysis [170], but this method has not been extensively studied in the context of SLCs until now. Stockwell Transform (ST) has been used to analyze the SLC signal of SiR insulators at different contamination levels in this work. Additionally, a Hyperbolic Gaussian window has been applied to improve the time-frequency resolution of the Stockwell Transform. Hyperbolic windows provide better resolution for the high and low-frequency components of non-linear signals, in comparison with classical Gaussian windows. That is why, to analyze non-linear SLC signals with different contamination levels, the hyperbolic window Stockwell transform is more appropriate.

This study aimed to investigate the SLC signals obtained from an 11 kV silicon rubber (SiR) insulator with different degrees of surface contamination. By employing the Hyperbolic Stockwell transforms (HST) technique in the time-frequency domain, these signals were analyzed. A special kind of 2D features matrix namely the Hyperbolic Stockwell (HS) matrix, was created using a combination of magnitude and frequency analysis. This was done by analyzing the SLC signals. In order to separate the magnitude spectrum from the phase spectrum, HS matrix (i.e., complex time-frequency matrix) has been segmented into two parts. Based on the phase and magnitude spectrum, 15 numbers of HST features have been extracted. After that, a total of 5 significant HST features were chosen through the Least Absolute Shrinkage and Selection Operator (LASSO) feature selection method. Finally, four machine-learning classifiers are chosen to predict the contamination degree of overhead line insulators based on these relevant HST features. The proposed framework shows better classification accuracy than previously reported in existing standard time-frequency analyses.

4.2 Artificial Contamination of SiR Insulator

4.2.1 Preparation of Samples

In this paper, a commercially available 11 kV SiR insulators were used for experimental purposes. Technical specifications of SiR insulator are already illustrated in Table 1.2 in chapter 1 (section 1.3.1). To contaminate the surface of SiR insulator, solid layer method (reported on IEC 60507) was adopted in this work [171]. In the solid layer method, the insulator surface is coated with a slurry prepared with the help of kaolin, salt (*NaCl*) and distilled water [150], [145] – [146], [172]. It should be mentioned here that the contamination severity can be varied through varying the quantity of salt. A detailed explanation of preparing artificially contaminated samples is discussed in

chapter 2 (section 2.2.1). Photographs of artificially contaminated (surface) samples of SiR insulators are depicted in Fig 4.2.



Fig 4.2. Image of artificially contaminated SiR insulator (11 kV).

4.2.2 Description of Contamination Classes

In this study, insulators surface contamination severity was evaluated by ESDD or equivalent salt deposit density method. For this purpose, the steps were followed as per the IEC 60815 standard [70]. In this work, it has been noticed that the ESDD quality range varies from 0 - 0.5 mg/cm². According to the ESDD range and quantity of *NaCl* salt, the surface contamination of SiR insulators has been divided into five classes. The contamination classes are: Very Light (CL-1), Light (CL-2), Medium (CL-3), High (CL-4) and Very High (CL-5). In Chapter 2 (section 2.3), an elaborated discussion on the calculation of the ESDD method has been demonstrated. Similarly, according to the ESDD value, the five pollution classifications are shown in Table 2.3 in chapter 2.

4.3 Acquisition of Surface Leakage Current (SLC) Signal

To accruing SLC data, a setup was developed for the experiment in the laboratory from the several artificially contaminated samples at room temperature. Again, the SLC data of different contamination categories was acquired employing an experimental setup mentioned in Chapter 2 (Section: 2.2.2). To measure SLC data, the IEC 60507 standard was followed and the experimental setup's schematic diagram is presented in Chapter 2 at Section 2.2.2 in Fig. 2.4 (a) and Fig. 2.4 (b) [144] – [146], [150]. The data was acquired and stored on a USB device via a Digital Storage Oscilloscope (DSO). Following that, the obtained data was transferred to a computer to be analyzed. Using this setup, SLC signals from SiR insulators were recorded at three different voltage levels (i.e., 10 kV, 11 kV, and 12 kV). Through DSO, the profiles of different system voltages (i.e., 10 kV, 11 kV, and 12 kV) were also measured during leakage current measurements. The waveforms of the

supply voltages are already illustrated in Chapter 2 (Section: 2.2.2.2, Fig. 2.10 (b)).

4.4 Features Extraction using Hyperbolic Stockwell Transform (HST)

4.4.1 Fundamentals of Hyperbolic Stockwell Transform (HST)

Hyperbolic Stockwell Transform (HST) is an enhanced version of Stockwell Transform (ST). The S-transform can be used to analyze the non-linear behaviour of real-time signals. Before ST, the Fourier transform (FT) was used as a very popular signal-processing tool. But in the present situation, the Fourier transform has several limitations. The main drawback of FT is that it cannot provide any information on spectral components of the entire time series. The FT cannot detect the time distribution for the influences of different frequencies, which affects the performance during signal processing of non-linear signals. Moreover, the Short Time Fourier Transform (STFT) is also not compatible with non-linear signals because the width of the window of STFT is fixed, and the output of the STFT gets affected due to the presence of noise signal [165]. For that reason, the time-frequency analysis such that S-transform and HST are preferred.

Stockwell Transform (ST) and Hyperbolic Stockwell Transform (HST) have frequency dependent time-frequency domain's resolution. A hyperbolic Gaussian window is implemented for time-frequency analysis in place of the conventional Gaussian window of the ST [172]. Due to its suitability for analyzing SLC signals of different contamination levels, the hyperbolic window Stockwell transform provides better flexibility than the classical Gaussian window at both low and high frequencies [168]. While maintaining a direct correlation with the Wavelet Transform (WT) and Short Time Fourier Transform (STFT), the classical Stockwell Transform (ST) delivers frequency-dependent signal resolution [165] – [166], [168]. The mathematical expression of the classical Stockwell Transform (ST) is represented as follows [166], [168] – [169], [188]:

$$S_{SLC}(\sigma, f_s) = \int_{-\infty}^{+\infty} p(t) w_{sw}(\sigma - t, f_s) e^{-2\pi i f_s t} dt \quad (4.1)$$

In the aforesaid equation (4.1), Classical Stockwell Transformation (ST) is represented as $S_{SLC}(\sigma, f_s)$, $p(t)$ is the time varying surface leakage current signal and Gaussian Window function of ST is represented $w_{sw}(\sigma - t, f_s)$.

Moreover, the Gaussian window function $w_{sw}(\sigma - t, f_s)$ can be further expressed as [168] – [169]:

$$w_{sw}(\sigma - t, f_s) = \frac{f_s}{\sqrt{2\pi}} e^{-\frac{f_s^2(\sigma-t)^2}{2}} \quad (4.2)$$

Condition Assessment of Overhead Line Silicone Rubber Insulators by employing Surface Leakage Current Signal and Hyperbolic Stockwell Window Transform

In equation (4.1 and 4.2), the Gaussian window parameter is σ , which can control the position of the window [165]. The resolution of a time event can normally be improved with a narrow gaussian window in classical stockwell transforms [166]. Frequency resolution is poor when the time domain window is thin, but it improves its resolution in the frequency domain when the time domain window is narrowed. An alternate solution is introduced a sharper front taper and a slower back taper in the Gaussian window to compensate the window's resolution. It is possible to improve event initiation time resolution by using this asymmetric window. The window function of the Hyperbolic Stockwell Transform (HST) is scalable and frequency dependent that is different from the conventional Gaussian window of ST [170]. In addition, the hyperbolic window is flexible with frequency variation. It is noteworthy that the hyperbolic window becomes an asymmetric window at low frequencies. In contrast, this hyperbolic window has a symmetric Gaussian window at high frequencies. The symmetrical window provides good frequency resolution at high frequencies and the hyperbolic window's asymmetry is advantageous for analyzing the phenomenon very far in the time-frequency domain [166]. With its inherent flexibility in the window function, HST is more valuable than classical ST when predicting contamination degrees from SLC signatures. The mathematical representation of the hyperbolic window is shown below [172]:

$$w_H = \frac{2f_s}{\sqrt{2\pi(\rho_H^F + \rho_H^B)}} e^{-\frac{f_s^2 [C_H(\sigma-t, (\rho_H^F, \rho_H^B, \beta_H))]^2}{2}} \quad (4.3)$$

In equation (4.3), the mathematical expression of hyperbola C_H is represented as:

$$C_H = \left[\frac{\rho_H^F + \rho_H^B}{2\rho_H^F \times \rho_H^B} \right] (\sigma - t - \xi^H) + \left[\frac{\rho_H^F + \rho_H^B}{2\rho_H^F \times \rho_H^B} \right] \sqrt{(\sigma - t - \xi^H)^2 + \beta_H^2} \quad (4.4)$$

The following parameters can control the shape of the hyperbola: (i) positive curvature parameters β_H , (ii) front tapper ρ_H^F and (iii) back tapper ρ_H^B .

Apart from this, the translation factor ξ^H helps to make sure that the peak of the hyperbola always arises at: $(\sigma - t) = 0$. Mathematical expression of translation factor ξ^H is given below:

$$\xi^H = \sqrt{\frac{(\rho_H^F - \rho_H^B)^2}{4\rho_H^F \times \rho_H^B}} \times \beta_H \quad (4.5)$$

It should be mention here that, the nature of the non-stationary surface leakage current signal was discrete, and due to this fact, discrete HST was selected in this work. Mathematical expression of the hyperbolic window S-transform is as follows [168]:

$$H_S(m, l) = \sum_{l=0}^{N-1} p_{SLC}(l+m) w_{AH}(l, m) e^{i2\pi lj} \quad (4.6)$$

In the above equation (4.6), SLC signal's shifted form of discrete Fourier Transform (FT) is represented as $p_{SLC}(l+m)$ and asymmetric hyperbolic window's FT is denoted $w_{AH}(l, m)$. In this work, HST provides the output of a two-dimensional complex hyperbolic stockwell (HS) matrix. The HS matrix contains two components such as the amplitude and phase spectrum of HS matrix. In equation (4.7), expression of HS matrix is given below:

$$H_S(m, l) = M_{m,l} \times e^{\psi_{m,l}} \quad (4.7)$$

In the matrix, columns correspond to sample points for the signal, whereas rows represent frequency.

4.4.2 Tuning of Hyperbolic Stockwell Window Parameters

The selection of the precise window parameter is essential to enhance the characteristics of SLC signals with HST. SLC signals are nonstationary with different contamination levels, so setting a fixed window parameter for a different type of SLC signals is technically inappropriate. As a result, grid search optimization was used in this work to select the front taper, back taper, as well as the positive curvature parameter value for the HST window function.

Grid Search Optimization (GSO) is a technique used in machine learning and optimization to catch the best combination of hyperparameters for a model. Those parameters are fixed before the training of the model, like learning rate, regularization strength, and number of hidden layers. Grid Search Optimization (GSO) involves specifying a grid of possible hyperparameter values and training the model for each combination of hyperparameters in the grid. The model performance is assessed using a validation set or cross-validation. The combination of hyperparameters that give the most satisfactory performance is chosen as the optimal set. The main advantage of grid search optimization is that, it is simple and easy to implement.

However, the drawback of grid search optimization is that it can be computationally expensive, especially when the number of hyperparameters and the size of the grid are large. The flowchart that outlines the steps involved in performing grid search optimization is presented in Fig 4.3. For the most optimized HST window parameters, three basic hyperparameters were used in Grid Search Optimization (GSO). These three hyperparameters are the front taper (ρ_H^F), back taper (ρ_H^B) and positive curvature (β_H) of the window, which are assigned as P, Q and R, respectively. A notable aspect is that the parameters were tuned using HS matrix ($H_S(m, l)$) Energy Concentration (EC) measurements [167].

Condition Assessment of Overhead Line Silicone Rubber Insulators by employing Surface Leakage Current Signal and Hyperbolic Stockwell Window Transform

In this work, the optimal range of front taper (ρ_H^F) and back taper (ρ_H^B) was identified by GSO as $0 < \rho_H^F < \rho_H^B < 1$. Similarly, the finest range of positive curvature value for HST window was assigned by GSO as $300 < \beta_H < 500$. Consideration has been given to the HS matrix, which yields maximum energy concentration. Notably, the front and back taper values have been kept low for narrowing the window width. In addition, higher values of positive curvature parameters can accelerate the transition from asymmetric to symmetric windows.

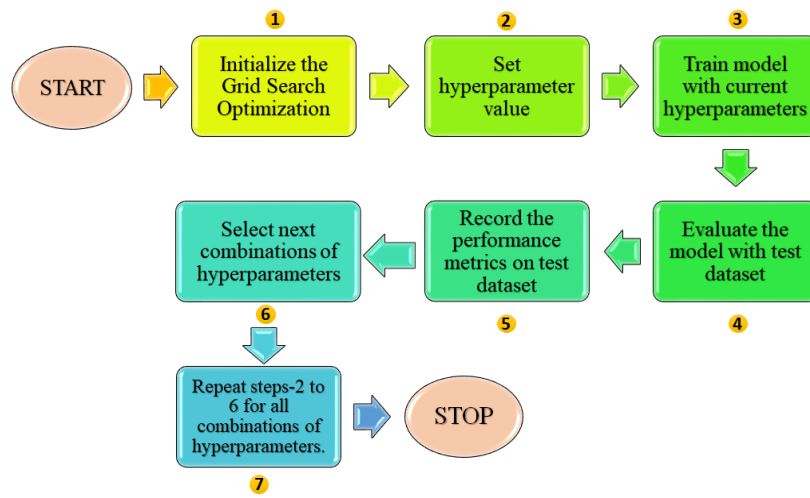


Fig 4.3. Outline of Grid Search Optimization.

4.4.3 Time-Frequency Domain's Extracted HST Features

A magnitude and phase spectrum of the HS matrix was used to extract 17 time-frequency statistical features. These features will also be referred to as the HST features set. Table 4.1 illustrates the aforementioned features in detail. All obtained 17 features were used to identify the contamination class of SiR insulator using four machine learning classifiers. The details of the feature classification process have been described in section 4.5.

Table 4.1. Features extracted from the HS matrix.

Features	Features Description
<i>F-1</i>	Maximum value of magnitude spectrum $M_{m,l}$ of HS matrix.
<i>F-2</i>	Mean value of the column corresponds to max value of magnitude spectrum $M_{m,l}$ of HS matrix.
<i>F-3</i>	Power of the column corresponding to max value of magnitude spectrum $M_{m,l}$ of HS matrix.
<i>F-4</i>	Standard Deviation of the column corresponding to max value of magnitude spectrum $M_{m,l}$ of HS matrix.
<i>F-5</i>	Skewness of the column corresponding to max value of magnitude spectrum $M_{m,l}$ of HS matrix.
<i>F-6</i>	Kurtosis of the column corresponding to max value of magnitude spectrum $M_{m,l}$ of HS matrix.
<i>F-7</i>	Mean value of the row corresponds to max value of magnitude spectrum $M_{m,l}$ of HS matrix.
<i>F-8</i>	Power of the row corresponding to max value of magnitude spectrum $M_{m,l}$ of HS matrix.
<i>F-9</i>	Standard Deviation of the row corresponding to max value of magnitude spectrum $M_{m,l}$ of HS matrix.
<i>F-10</i>	Skewness of the row corresponding to max value of magnitude spectrum $M_{m,l}$ of HS matrix.
<i>F-11</i>	Kurtosis of the row corresponding to max value of magnitude spectrum $M_{m,l}$ of HS matrix.
<i>F-12</i>	Mean value of the column corresponds to max value of phase spectrum $e^{\psi_{m,l}}$ of HS matrix.
<i>F-13</i>	Power of the column corresponds to max value of phase spectrum $e^{\psi_{m,l}}$ of HS matrix.
<i>F-14</i>	Standard Deviation of the column corresponds to max value of phase spectrum $e^{\psi_{m,l}}$ of HS matrix.
<i>F-15</i>	Mean of the row corresponds to max value of phase spectrum $e^{\psi_{m,l}}$ of HS matrix.
<i>F-16</i>	Power of the row corresponds to max value of phase spectrum $e^{\psi_{m,l}}$ of HS matrix.
<i>F-17</i>	Standard Deviation of the row corresponds to max value of phase spectrum $e^{\psi_{m,l}}$ of HS matrix.

4.5 Machine Learning Classifiers

This work used four machine learning classifiers to estimate contamination levels employing time-frequency HST features of SLC signals. A concise discussion of the classifiers mentioned above is given in section 4.5.1.

4.5.1 Support Vector Machine (SVM)

In binary classification, support vector machines are widely used as classifiers [174] – [175]. Support vector machine (SVM) (a classic machine learning algorithm) was proposed by Vapnik *et al.* [174]. The structural risk problem can be reduced by SVM algorithm. Apart from this, it uses statistical theory during the implementation of classification process. SVM classifiers are designed to maximize the margin between two data points by finding an optimal hyperplane [174], [181] – [183].

The present work uses multiclass SVM classification tools to detect the multi-classes of HST features acquired in the feature extraction process. Using the one-against-all approach (OAA), the author employed multiclass SVM in this work. It is noteworthy that selecting the appropriate kernel function can help to enhance the effectiveness of SVM operation. Several kernel functions, like linear, polynomial, and radial basis functions (RBF), were employed to performance testing of the SVM classifier [175].

In the reported work the training dataset that is provided is: $S_T = \{x_z, c_z\}_{z=1}^{n_T}$, where the sample of the training dataset is $x_z \in \mathbb{R}^{n_T}$, class label is denoted here as: $c_z \in \{+1, -1\}$, and the training datum's number is denoted as: n_T . To segregate the whole training dataset into positive and negative classes, an appropriate hyperplane is selected in the SVM process. The mathematical illustration of the hyperplane is presented below as [181]:

$$h_p(x) = w_{hp} \cdot x + b_{hp} \quad (4.8)$$

In equation 4.8, w_{hp} refers as the weight vector and b_{hp} indicates bias terms of hyperplane equation. Therefore, the condition for optimal hyperplane can be defined as [181]:

$$\min_{w_{hp}, b_{hp}} C(w_{hp}, b_{hp}) = \frac{1}{2} w_{hp}^t w_{hp} \quad (4.9)$$

subjected to $y_z (w_{hp}^t x_z + b_{hp}) \geq 1, z = 1, 2, \dots, n_T$. A soft classification formula is obtained in equation (4.9), in which some misclassifications are penalized.

$$\min_{w_{hp}, b_{hp}} \frac{1}{2} w_{hp}^t w_{hp} + C_{pen} \sum_{z=1}^{n_T} \zeta_z \quad (4.10)$$

subjected to $y_z(w_{hp}^t x_z + b_{hp}) \geq 1 - \zeta_z, \zeta_z \geq 0 \quad z = 1, 2, \dots, n_T$. In the equation (4.10), C_{pen} denotes the cost penalty factor whereas the slack variable denotes as ζ_z . It should be mentioned here that, to balance the complexity of the model and nullify the model's training error, the cost penalty factor has been employed [181].

In this work, the classification problem is nonlinear, so a nonlinear mapping function $\varphi_s(x)$ is used to plot original data space \mathbb{R}^{n_r} into high-dimensional feature space. It is noteworthy that the nature of the dataset is inseparable. The nonlinear classification problem becomes linear after applying the aforesaid steps. Apart from this, determining the inner product's $\varphi_s^t(x)\varphi_s(x)$ performance in the feature space is difficult. In this regard, an appropriate kernel function has been used and it plays a pivotal role in classification process. The mathematical expression of the kernel operation is shown below [181]:

$$K_s(x_i, x_j) = \varphi_s^t(x_i)\varphi_s(x_j) \quad (4.11)$$

A kernel function can be regarded as a linear, polynomial, or radial basis function (RBF) [182], depending on the application. SVM classification is mainly performed with radial basis functions with Gaussian forms. In this study, the radial basis (RBF) kernel function with Gaussian form has been utilized and it can be mathematically expressed as [182]:

$$K_s(x_i, x_j) = \exp\left(\frac{\|x_i^t - x_j\|}{2 \times \delta_s^2}\right) \quad (4.12)$$

The Kernel function parameter is denoted in the above equation (4.12) as δ_s . The δ_s reflects the distribution features of the training data sample [174]. Although the present work is a multiclass problem, SVM classification is usually used for binary classification. For multi-class classification, ensemble SVM topology was adopted to address that concern. As reported in [183], the one-against-all (OAA) approach is the method for multiclass classification. A topology of five SVM classifiers was applied to identify five different classes of contamination severity. The schematic of an ensemble SVM is shown in Fig 4.4.

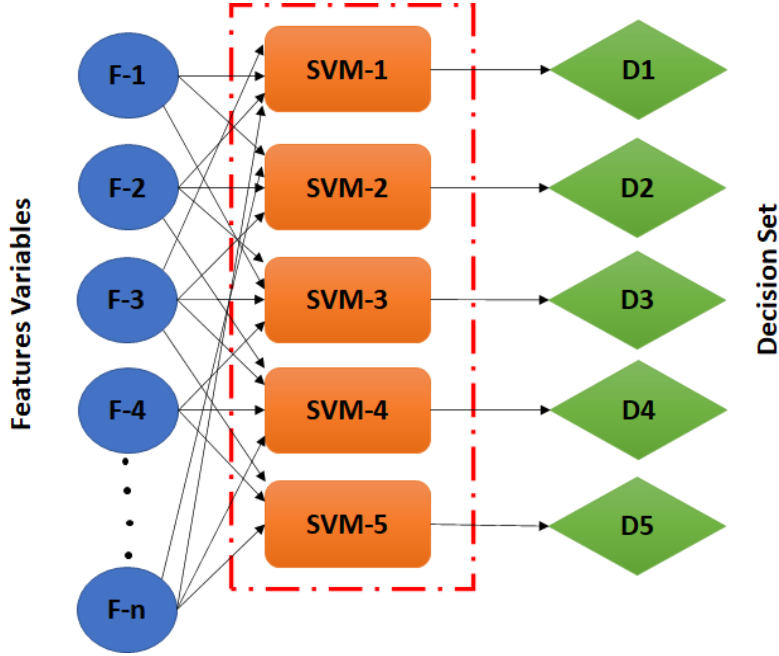


Fig. 4.4. Schematic diagram of Multiclass SVM construction.

4.5.2 *k*-Nearest Neighbor (*k*-NN)

An instance-based classifier such as the *k*-Nearest Neighbor (*k*-NN) classifier categorizes test samples based on their distance from the training dataset [184] – [186]. It is a well-known supervised classifier, widely utilized in the area of power engineering, bio-medical engineering problem. On the other hand, it classifies test points based on their distance to training data points which comprises least computational complexity [176]. The number of nearest neighbor's ' k_E ' and can influence the performance of classifier.

In the present work, the training dataset that is provided is: $S_T = \{x_z, c_z\}_{z=1}^{n_T}$, where the sample of the training dataset is $x_z \in \mathbb{R}^{n_r}$, class label is denoted here as: $c_z \in \{+1, -1\}$, and the training datum's number is denoted as: n_T . After that, the unlabeled testing data is represented as x_T , The distance between every training datum is calculated by the *k*-NN classifier. Additionally, the Euclidean distance (k_E) has been taken into consideration, which is mathematically expressed as follows [176]:

$$k_E = dis(x_z, x_T) = \|x_z - x_T\|^2 \quad (4.13)$$

The classifier chooses k_E number of nearest instances based on the distance that is computed, i.e., $[x_{z_1}, x_{z_2}, \dots, x_{z_k}]$ and the related class label, i.e.,

$\left[c_{z_1} c_{z_2} \dots c_{z_k} \right]$. A significant part of k-NN classification performance is affected by the number of instances or the k-value.

4.5.3 Gaussian Naïve Bayes (GNB)

GNB, also known as Gaussian Naïve Bayes, is an effective tool for classifying data using the Bayes theorem [185] – [186]. In GNB, a probabilistic model has been designed based on the features and classification that can be accomplished using the decision rule of the probabilistic model [149]. The GNB classifier operates efficiently on small training datasets, as well as it takes less computational time to perform the classification. In addition, the GNB classifier suits high-dimensional datasets because each feature and variable were independently calculated [185]. In this work, GNB classifier has been implemented where gaussian probability density function has been adopted for the probabilistic model.

The feature variable set is F and the class variable set is D in this work. Based on the given model, the Bayes theorem was applied to predict the class label. This mathematical model can be represented as follows [185]:

$$\rho(D | F) = \frac{\rho(F | D)\rho(D)}{\rho(F)} \quad (4.14)$$

Where, $F = \{f_1, f_2, \dots, f_n\}$ and $D = \{D_1, D_2, \dots, D_n\}$. It is noteworthy that the characteristics of features set variables are conditionally independent. Bayes' theorem allows computing the probability of feature attributes at a class label D_j as follows [149, 185]:

$$\rho(D_j | f_1, \dots, f_n) = \frac{\rho(f_1 | D_j)\rho(f_2 | D_j) \dots \rho(f_n | D_j)}{\rho(f_1)\rho(f_2) \dots \rho(f_n)} \quad (4.15)$$

It can be further mathematically represented as [185]:

$$\rho(D_j | f_1, \dots, f_n) = \frac{\rho(D_j) \prod_{i=1}^n \rho(f_i | D_j)}{\rho(f_1)\rho(f_2) \dots \rho(f_n)} \quad (4.16)$$

Equation (4.16) can be neglected since its denominator remains unchanged in the case of the input feature variables. The following formula can be used to express equation (4.16):

$$\rho(D_j | f_1, \dots, f_n) \propto \rho(D_j) \prod_{i=1}^n \rho(f_i | D_j) \quad (4.17)$$

So, to estimate the class label, GNB classifier identifies the class which have maximum probability according to [185],

$$Y_z = \arg \max_{k \in [\rho_1, \rho_2, \dots, \rho_k]} \left(\rho(D_j) \prod_{i=1}^n \rho(f_i | D_j) \right) \quad (4.18)$$

In a Gaussian Nave Bayes classifier, feature values at a particular class label are supposed to follow a Gaussian distribution or normal distribution [185]. By using the Gaussian probability density function [185], it is expected that, for probability calculation of a feature characteristic f_i at each class level D_j .

$$\rho(f_i | D_j) = \frac{1}{\sqrt{2\pi\sigma_{D_j}^2}} \exp \left(-\frac{(f_i - \mu_{D_j})^2}{2\sigma_{D_j}^2} \right) \quad (4.19)$$

The standard deviation and mean for every feature variable of input are symbolized for each given class D_j as σ_{D_j} and μ_{D_j} respectively. GNB classifier stores mean and standard deviation for each input variable in each class. Equation (4.18), can therefore predict the input feature variable's f_i class label.

4.5.4 Random Forest (RF)

The application of Random Forest or RF classifier (an ensemble classifier) to many practical classification problems is very popular. The RF classifier consists of several relatively uncorrelated decision-tree classifiers [149]. Each decision-tree classifier randomly selects feature from the training dataset using the CART algorithm [171], [174] – [176]. Every decision-tree estimates the output, and the ultimate estimation is constructed on majority voting [156], [176] – [178], [187]. Detailed description of the aforesaid RF classifiers was discussed in chapter 3 (Section: 3.5.2.1).

4.6 Results and Discussion

4.6.1 Variation of Surface Leakage Current (SLC) Signal for Various Contamination Levels

In this study, 400 SLC signals (80 signals has been considered for each contamination level) has been recorded to predict the contamination level of polymeric insulator. The SLC signals were assimilated with a sampling frequency of 25 kHz. Those recorded SLC signals of SiR insulator at various contamination level have been presented in Fig. 4.5.

From Fig. 4.5, it can be observed that SLC signal becomes distorted with increase in the contamination level. Hence, using Hyperbolic Stockwell Transform (HST), the SLC signals were evaluated in time-frequency domain. Prior to that, hyperbolic window parameter of HST for a particular SLC signal has been tuned using grid search optimization.

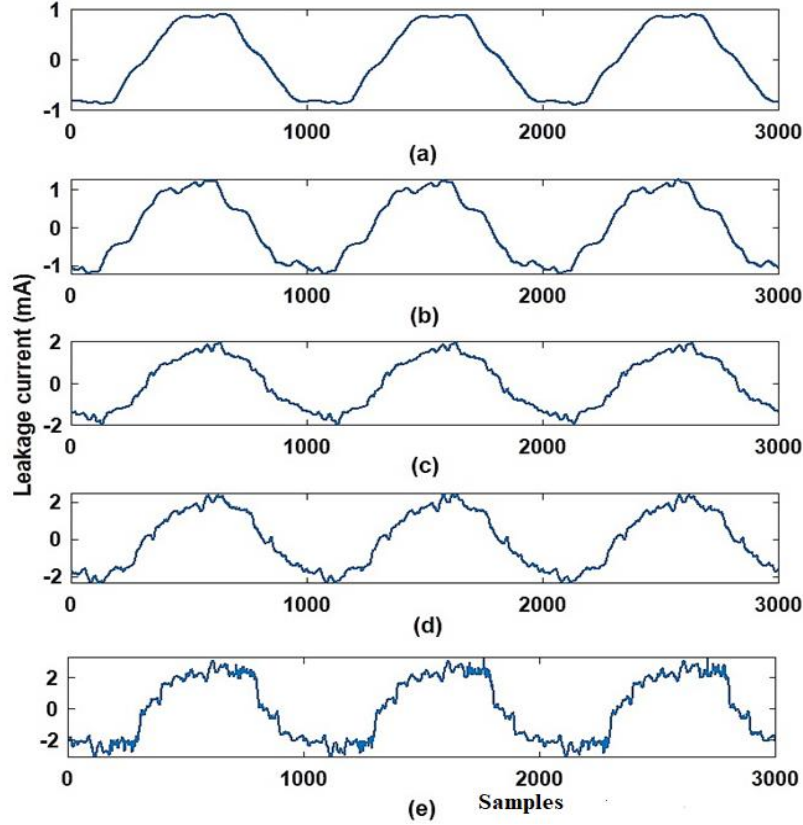


Fig. 4.5. SLC waveform of SiR insulator for class: (a) CL-1 (b) CL-2 (c) CL-3 (d) CL-4 and (e) CL-5.

4.6.2 Analysis of Selected HST Features

When the hyperbolic window stockwell transform was applied to an acquired SLC signal, it returned a 2-D complex HST matrix. The size of the HST matrix is 750×1500 . Fig 4.6 shows a magnitude contour plot of surface leakage current signal converted into HST matrix for light, moderate, and heavy contamination levels. An important aspect of any classification approach is features selection, since it can improve classification accuracy and reduce computational burden. Using the magnitude and phase spectrum of HST matrix, 17 time-frequency HST features were extracted. In this work, for features' selection the extracted HST features of SLC signal were further analyzed through the Least Absolute Shrinkage and Selection Operator (LASSO). LASSO is regarded as an embedded properties selector. LASSO regularization procedure was recommended by Tibshirani [179, 180].

Again, LASSO can augment any classifier model's interpretability, this is due to the fact that it can remove inapt features those are not related to the

response variables. As a result, the model's overfitting issue and computational time gets reduced [179].

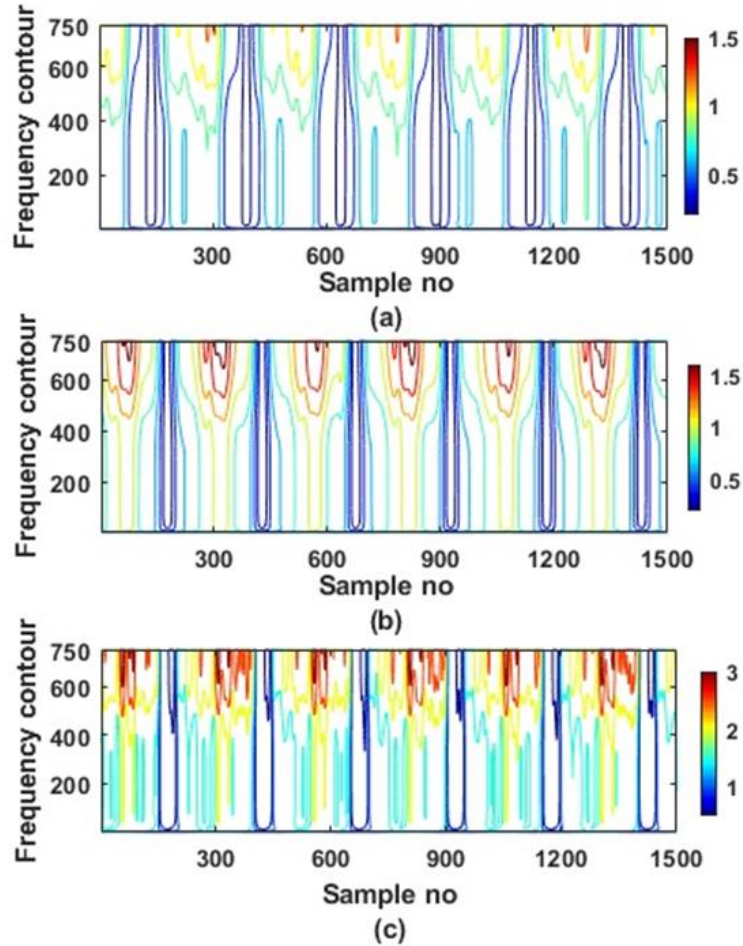


Fig. 4.6 Magnitude contour plots of SLC converted Hyperbolic Stockwell (HS) matrix for class (a) CL-2 (ρ_H^F , ρ_H^B and $\beta_H = 0.11, 0.23$ and 307) (b) CL-3 (ρ_H^F , ρ_H^B and $\beta_H = 0.11, 0.21$ and 324.5) and (c) CL-5 (ρ_H^F , ρ_H^B and $\beta_H = 0.12, 0.23$ and 321.5)

By using the penalty function, a sparse weight matrix is generated to discover the optimal feature [180]. The mathematical expression of LASSO function is defined as [179]:

$$\xi^{lasso} = \arg_{\xi} \min \left[\frac{1}{2} \sum_{i=1}^{n_l} (yt_i - \xi_0 - \sum_{j=1}^{m_l} f_{ij} \xi_j)^2 + \lambda_l \sum_{j=1}^{m_l} |\xi_j| \right] \quad (4.20)$$

The above equation can be rewrite as [30]:

$$\xi^{lasso} = \arg_{\xi} \min \sum_{i=1}^{n_l} \left[yt_i - \xi_0 - \sum_{j=1}^{m_l} f_{ij} \xi_j \right]^2 \quad (4.21)$$

Where, the threshold limit is denoted by $\sum_{j=1}^{m_l} |\xi_j| \leq t_h$.

Additionally, f_{ij} is the j^{th} property of i^{th} datum defined over $j = (1, 2, \dots, n_l)$ and $i = (1, 2, \dots, m_l)$. Whereas, yt_i denotes the marked value of i^{th} datum and ξ_j indicates the regression coefficient of j^{th} property. In addition, the lambda parameter $[\lambda_l \geq 0]$ is the coefficient of LASSO regularization that controls shrinkage of all coefficients [179].

This technique requires a threshold value less than or equal to the absolute addition of coefficients of regressions i.e., $\sum_{j=1}^{m_l} |\xi_j| \leq t_h$. Using the lambda

parameter $[\lambda_l \geq 0]$, the coefficients of regressions with lesser values are reduced to zero in feature space. i.e., $\xi_j(\lambda_l) = 0$. It is notable that inapt characteristics are removed from the model when the coefficient of a feature variable reaches zero. There is an inverse relationship between the threshold value and the lambda parameter, which means that the number of coefficients shrinks toward zero at higher values of lambda. The LASSO method performs better on input feature variables that are highly correlated; this allows LASSO to choose only one variable as a sampling point by shrinking the others to zero. In this approach, it is noteworthy to mention that the value of the lambda parameter was chosen as 0.15.

Apart from this, the LASSO function (ξ^{lasso}) selects 5 relevant feature variables out of 17 (as shown in Table 4.2) and decreases the coefficient of regression from the rest to zero. As a result, the classification cannot include feature variables with zero regression coefficients. Table 4.2 shows the output of LASSO feature selection, where true indicates selected feature variables, while false indicates eliminated feature variables. This operation is applicable to each class of contamination based on SLC data.

Condition Assessment of Overhead Line Silicone Rubber Insulators by employing Surface Leakage Current Signal and Hyperbolic Stockwell Window Transform

Table 4.2. Selection of true features by LASSO from the HST features.

Features	Decision
<i>F-1</i>	False
<i>F-2</i>	True
<i>F-3</i>	True
<i>F-4</i>	False
<i>F-5</i>	False
<i>F-6</i>	False
<i>F-7</i>	True
<i>F-8</i>	False
<i>F-9</i>	True
<i>F-10</i>	False
<i>F-11</i>	False
<i>F-12</i>	False
<i>F-13</i>	False
<i>F-14</i>	True
<i>F-15</i>	False
<i>F-16</i>	False
<i>F-17</i>	False

In this present work, five features namely F-2, F-3, F-7, F-9 and F-14 have been chosen through LASSO. The aforesaid five features were further analyzed through a box-whisker plot. Fig. 4.7, shows a box-whisker plot of selected features. These plots reveal significant variances between the median and quartiles (upper and lower) for selected features at five contamination levels. As a result, the following five features were used for the classification approach.

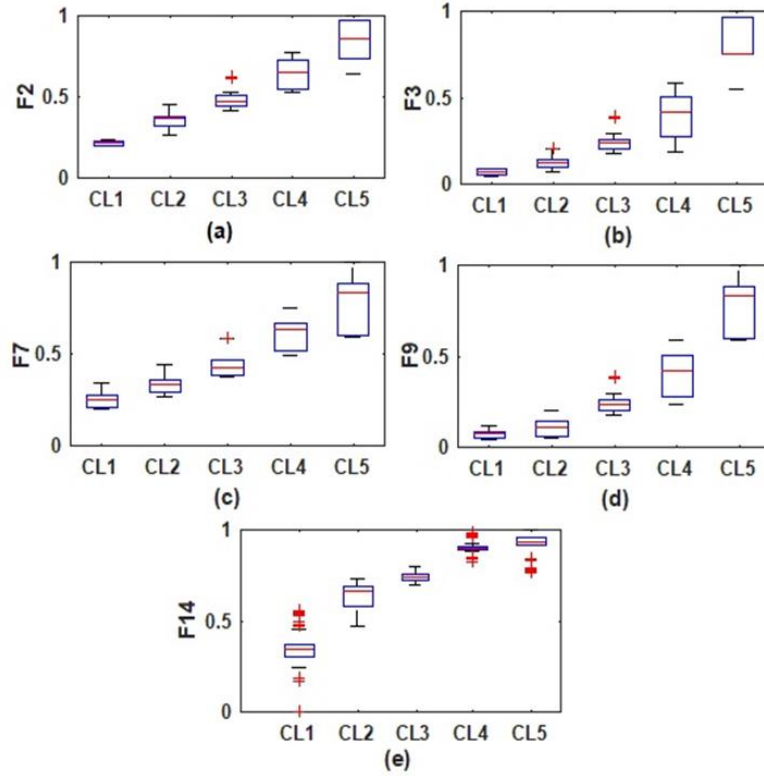


Fig. 4.7 Box-whisker plot of time-frequency HST features of SLC signal: (a) F-2 (b) F-3 (c) F-7 (d) F-9 (e) F-14

4.6.3 Performance Analysis of Machine Learning Classifiers

As mentioned earlier, four machine learning classifiers were used in the present work to assess the performance of time-frequency HST features. This paper implemented a 10-fold cross validation technique to attain reliable performance hence overfitting can be avoided. For training testing purposes, extracted HST features have been divided into 10 parts at a ratio of 9:1. The performance of the classifiers was evaluated through three parameters namely accuracy, sensitivity and specificity. The description of the aforesaid parameters has been expressed as follows:

$$Accuracy(\%) = \frac{(TP + TN)}{(TP + FP + TN + FN)} \times 100 \quad (4.22)$$

Condition Assessment of Overhead Line Silicone Rubber Insulators by employing Surface Leakage Current Signal and Hyperbolic Stockwell Window Transform

$$Sensitivity(\%) = \frac{TP}{(TP + FP)} \times 100 \quad (4.23)$$

$$Specificity(\%) = \frac{FP}{(TN + FP)} \times 100 \quad (4.24)$$

The terms TP, TN, FP, and FN in 4.23 and 4.24 are indicated as correct positive prediction, accurate negative prediction, wrong positive prediction, and wrong negative prediction, respectively. Accordingly, the aforementioned evaluation indices can be extracted considering the confusion matrix. The outline of the suggested framework is presented in Fig. 4.8.

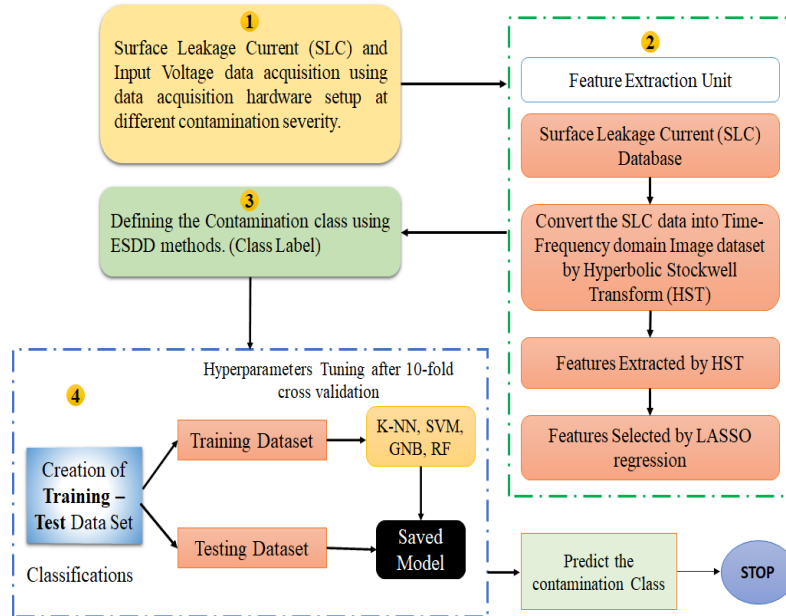


Fig. 4.8 Outline of the recommended model for contamination class predictions for overhead line SiR insulators.

Considering the confusion matrix, the aforementioned parameters have been extracted based on various classifiers. The mean values and standard deviation of those classification parameters for four different classifiers have been represented in Table 4.3. From Table 4.3, it has been noticed that, the performance of Random Forest or RF classifier is better than Support Vector Machine or SVM (with Radial Basis kernel function (RBF)), k-Nearest Neighbor or k-NN (k = 6) and GNB. Again, it can be stated that, the classification performance has been found to be better for RF classifiers than

Gaussian Naïve Bayes or GNB and SVM (with a linear kernel function). Further, it should be mentioned here that, the hyper-parameters for the RF classifier (i.e., number of trees) and the k-NN (i.e., kernel function) have been optimized using the grid search optimization method. It has been noticed that, all classification parameters show a low standard deviation value, which indicates robustness of HST features.

Table 4.3. Classifiers performance by the proposed method.

Classifiers	Accuracy (%)	Sensitivity (%)	Specificity (%)
Gaussian Naïve Bayes	95.56 ± 0.73	95.74 ± 0.64	98.87 ± 0.19
k-Nearest Neighbor (k = 6)	97.42 ± 0.46	97.39 ± 0.49	99.32 ± 0.13
Support Vector Machine (Linear)	96.32 ± 0.55	96.44 ± 0.58	99.08 ± 0.12
Support Vector Machine (Polynomial)	97.09 ± 0.63	97.12 ± 0.66	99.21 ± 0.14
Support Vector Machine (Radial Basis Function (RBF))	97.89 ± 0.39	97.84 ± 0.36	99.49 ± 0.09
Random Forest (no. of trees = 200)	98.08 ± 0.32	98.13 ± 0.36	99.57 ± 0.10

4.6.4 Comparative Study on Other Time-frequency Methods

To get a superior idea about the feasibility of the recommended method, the comparison of its performance was carried out with time-frequency-based transform methods. Using the classical stockwell transform (ST), short time Fourier transform (STFT), and continuous wavelet transform (CWT), the recorded SLC signals of SiR insulator was analyzed in the time-frequency domain. It should be mentioned here that for continuous wavelet transform, the Morlet mother wavelet was adopted. However, for the STFT, a hammer window with 75% overlap was used to analyze SLC signals in the time frequency domain. SLC signal performance was evaluated by extracting seventeen features from the magnitude and phase spectrum of the time-frequency ST, WT and STFT matrix of the SLC signal (i.e., elaborately described in section 4.4.3). The extracted time-frequency ST, WT and STFT features were further evaluated through LASSO and the selected features have been fed to a classifier. Table 4.4 indicates that time-frequency HST

Condition Assessment of Overhead Line Silicone Rubber Insulators by employing Surface Leakage Current Signal and Hyperbolic Stockwell Window Transform

features are more effective than other time-frequency features, which is indicative of the proposed method's effectiveness.

Table 4.4. Comparative Performance analysis with other time-frequency methods.

Time-Frequency Method	Classifier	Accuracy (%)
STFT	k-NN	93.79 ± 1.41
	SVM (RBF)	93.83 ± 1.08
	RF	94.72 ± 0.83
WT	k-NN	94.49 ± 0.94
	SVM (RBF)	95.31 ± 0.68
	RF	95.56 ± 0.64
ST	k-NN	95.82 ± 0.66
	SVM (RBF)	96.09 ± 0.55
	RF	96.53 ± 0.42
HST	k-NN	97.42 ± 0.46
	SVM (RBF)	97.89 ± 0.39
	RF	98.08 ± 0.32

Further, the comparison of the performance of the recommended method has also been carried out with a conventional method. Based on Table 4.5, the superior action of the recommended method has been observed than the existing method. Therefore, it can be stated that, the application of the suggested technique for the condition assessment of SiR insulators results in more reliable method than the existing methods. An analysis is done by comparing the existing methods with the recommended method as illustrated in Table 4.5.

Table 4.5 Comparative analysis with existing methods.

Paper	Methods	Name of the Classifier/s	Accuracy (%)
[150]	Autocorrelation	Rough Set Classifier	90.7
[146]	Short Time Modified Hilbert Transform	Sparse Classifier	95.0
Proposed Work	Hyperbolic Stockwell Transform	k-NN	97.42 ± 0.46
		SVM (RBF)	97.89 ± 0.39
		RF	98.08 ± 0.32

4.7 Conclusion

This article presents a novel framework for estimating contamination levels in SiR insulators using Surface Leakage Current (SLC) signals. In another way to study of SLC signals in the time-frequency domain, a hyperbolic window has been used instead of the conventional gaussian window. Besides, the parameters of the hyperbolic window have been further optimized using grid search optimization techniques for the maximization of the measurement of energy concentration of time-frequency matrix. From the SLC signal converted into a complex time-frequency Hyperbolic Stockwell (HS) matrix, five time-frequency features have been selected which are highly linked with the SiR insulator's contamination level. Based on the classification results, it has been observed that all the classifiers have returned satisfactory performance. Among them, RF classifiers have provided the most effective performance. The proposed method has the following advantages.

- Classification performance of the suggested framework is not influenced by variation in voltage levels.
- A framework is proposed that is adaptive to SLC signal signatures.
- Proposed framework is independent of the insulator's dimension.
- In terms of analyzing time and frequency, the proposed strategy demonstrates superior performance in comparison to techniques such as the Stockwell Transform, Short-Time Fourier Transform, and Continuous Wavelet Transform.
- Proposed method shows improved performance than other existing classifier-based methods of insulator condition monitoring through SLC analysis.

Therefore, it can be concluded that the proposed Hyperbolic Stockwell Transform (HST) based feature extraction technique can be executed for the assessment of the overhead line SiR insulator's condition. The proposed framework's main limitation is the time required for predicting the surface contamination level of overhead line insulators using SLC signals.

In addition, the proposed framework's classification process is a supervised learning approach, which is cumbersome. The generated features matrix from the HST method is then needed to arrange input and output variables for supervised feature classification. Based on the training data, the learning algorithm of classifiers makes predictions iteratively. The algorithm will be stopped once it reaches an acceptable performance level. Due to its iterative process, the proposed model is inconvenient for real-time data processing. Due to the aforesaid limitations, a proposed unsupervised classification model has been developed with deep learning techniques. A detailed discussion of the proposed framework is reported in the next chapter.

Chapter 5

Time-frequency Domain Analysis of Leakage Current Signal of Overhead line Polymeric Insulator by Cross Hyperbolic Stockwell Transform Aided Fine-tuned Convolutional Neural Network Technique

5.1 Introduction

In *Chapter 4*, the proposed model has been implemented based on Surface Leakage Current (SLC) signals analysis. The proposed framework achieved satisfactory outcomes. Furthermore, the time domain SLC signal was transformed into time-frequency domain image data via the Hyperbolic Stockwell Transform (HST) technique. In the HST method, firstly, the features were extracted. Then, overhead line insulator surface contamination was identified using extracted features fed into various machine-learning classifiers manually. Therefore, manual feature extraction and features classification are highly unpredictable and time-consuming. Aforesaid hand-crafted methods may lose features during the process, resulting in undesirable outcomes. Considering the aforesaid drawbacks, this chapter presents a framework, in which features are extracted using a Cross-Hyperbolic Stockwell transform (XHST). Thereafter, the selection and classification of optimal features were achieved automatically with the help of a fine-tuned convolution neural network technique. Thus, in this proposed framework, automated processes eliminate the computational burden. This proposed method monitors overhead line insulators' surface conditions faster and more efficiently.

It has already been mentioned in previous chapters that environmental pollutants can degrade the SiR insulator's surface under moist conditions. Different climate conditions significantly impact the surface condition of SiR insulators as well as affect SiR insulators' performance when used in outdoor applications. The surface of the SiR insulators is eroded due to the following environmental factors: fog, raindrops, dew, sea salt, sand, dust, soil and air contamination [7], [189] – [191]. Surfaces of overhead line insulators are contaminated with water particles and environmental pollutants, creating conductive paths. These paths aid the flow of leakage current on overhead line insulators. In [191], it was reported that an irregular distribution of electric fields stimulates surface leakage current (SLC) and a variation in current density was observed on the surface of SiR insulators. Consequently, dry bands were developed at various locations on the SiR Insulator's surface. It is noteworthy to mention that these dry bands are treated as open circuits across the SiR insulator surface [7], [191] – [192]. As a result, the SLC flow

is hindered by these dry bands, which in turn causes deterioration in the SiR insulator's surface property through the Joule heating effect. Additionally, the intensity of the electric field at the boundaries of dry bands is high, leading to overhead line insulators breakdown. These factors, therefore, cause undesirable power outages on transmission and distribution lines. For this reason, monitoring the SiR insulator surface regularly is essential to ensure its longevity. Therefore, analysis of surface leakage current signals is an effective way in studying overhead line insulators' surface conditions. The previous two chapters proposed methodologies to predict surface contamination severity based on SLC signal processing. To acquire SLC signals, a shunt device is required to connect directly in contact with SiR insulators under test which is demonstrated elaborately in Chapter 2 (section 2.2.2 and section 2.2.2.1) [70], [149].

At highly contaminated conditions, the leakage current signature becomes highly distorted, non-stationary, and contains partial arcs. It can be significant for overhead line insulators to perform poorly when they are heavily contaminated. ESDD (Equivalent Salt Deposit Density) is used to determine how heavily the surface of the insulator has been contaminated [70]. However, this approach has some drawbacks, such as a time-consuming and complex calculation approach. Therefore, to keep track of how badly overhead line insulators are contaminated, researchers have presented several approaches [193] – [195]. Among them, the well-known method is surface leakage current (SLC) signal analysis [70], [144], [193]. According to [150], the degree of SiR insulator surface contamination influences the signature of the SLC signal. A standard method for determining the state of the overhead line insulator is to estimate the phase difference between the SLC and source voltage [193]. However, the aforesaid approach depends on the input voltage. It is noteworthy that measuring the input voltage on the high-voltage side is costly [144]. In [144], using odd harmonic components of SLC signals, the degree of surface contamination of overhead line insulators can be estimated. In this regard, the SLC signal's odd harmonic components have been extracted using the Fast Fourier transform (FFT). It should be mentioned here that the SLC becomes non-stationary and distorted as contamination severity increases. It has been noted that FFT analysis cannot detect the source of signal distortion, such as the effect of harmonics on a signal, or surface contamination or external noise. For this reason, FFT implementation is not suitable for non-linear signal analysis. Furthermore, aliasing and signal leakage adversely affect FFT analysis outcomes and may result in inaccurate results. That is why stationary signals can only be processed using FFT analysis.

For identifying contamination severity, SLC signals have been tested through Short Time Hilbert Transform (STHT) [150], statistical analysis [194], autocorrelation [146], recurrence plots [195] and Hyperbolic Stockwell Transform (HST) [7]. However, in previous research, contamination indicators or features had been manually extracted from SLC signals [196]. In addition, these manual feature extraction methods are highly unpredictable

and may require deep signal processing knowledge. Hand-crafted methods may lose features during the process, resulting in undesirable outcomes.

According to the aforesaid observations, studying the nonlinear dynamics of surface leakage current (SLC) signals with respect to surface contamination severity can be effectively achieved by analysis of SLC in a joint time-frequency plane. In this work, the authors acquired SLC data in the laboratory environment using the data acquisition setup for different contamination classes of SiR insulator samples. The Cross Hyperbolic Stockwell Transform (XHST) was utilized for feature extraction into the time-frequency domain. In this regard, the acquired time-domain SLC signals were converted into joint time-frequency domain image data. After that, the acquired feature matrix was utilized for automated feature classification. Notably, the SLC signals of various contamination levels were cross-correlated with an uncontaminated surface leakage current signal using XHST. The XHST window parameters were fine-tuned by Bayesian Optimization (BO) to get more precise results in the T-F domain. Afterwards, transfer learning with a fine-tuning strategy was implemented on a pre-trained CNN model (i.e., VGGNet-16) for automatic feature classification and contamination class prediction. The proposed schematic is suitable for any dimension of overhead line insulators. Thus, the proposed framework can automatically sense the prior state of any failure of overhead line insulators due to contamination.

5.2 Basic Concept of Hyperbolic Stockwell Transform (HST)

The Hyperbolic Stockwell Transform (HST) is a signal processing tool used for analyzing time-frequency information in a signal. In mathematical terms, the XHST is a modified version of the Stockwell Transform (ST), a variant of the classical Fourier Transform. In addition, due to the static window shape, ST cannot give consistent results for non-linear SLC signals. In order to overcome these limitations, the Hyperbolic Stockwell Transform (HST) has been introduced to replace the Stockwell Transform (ST). That is why, the conventional Gaussian window of ST has been replaced by a hyperbolic window for better time-frequency resolution. The detailed explanation of the aforesaid techniques is elaborately explained in Chapter 4 (Section 4.4.1).

In Stockwell Transform (ST), the fixed-shaped Gaussian Window ($g_w(t)$) function can be expressed as [197]:

$$ST_{(\tau, f_a)} = \int_{-\infty}^{+\infty} g_w(t) \left[\frac{|f_a|}{\sqrt{2\pi}} \times e^{\left(-\frac{f_a^2 (\tau-t)^2}{2} \right)} \times e^{(-2\pi i f_a t)} \right] dt \quad (5.1)$$

In the above expression (1), the fixed-shaped Gaussian Window ($g_w(t)$) is denoted as:

$$g_w((t-\tau), f_a) = \frac{|f_a|}{\sqrt{2\pi}} \times e^{\left(-\frac{f_a^2(\tau-t)^2}{2}\right)} \quad (5.2)$$

The standard deviation is $\sigma = 1/|f_a|$ inversely proportional to the translational parameter (τ) and system frequency (f_a). ST is capable of processing high-frequency as well as low-frequency signals with high resolution [197].

In addition, due to the static window shape, Stockwell Transform (ST) cannot give consistent results for non-linear SLC signals. In [95], [100] – [101], provide additional information about the Stockwell transform (ST). That is why a modified version of the Stockwell Transform, that is, the Hyperbolic Stockwell Transform (HST) [198] – [199], has been introduced to overcome the aforesaid limitations. The window function of HST is hyperbolic and it is a frequency-dependent function [200]. The main reason for choosing HST is because it shows an asymmetrical nature of low-frequency signals and symmetrical nature during high-frequency signals. HST is flexible because it can satisfactorily manage both types of frequency components [167], [200]. The parameters of the window can be adjusted to modify the shape of the window [167], [200]. Advantage of HST is that it gives precise results in the high-frequency and low-frequency domains compared with conventional Stockwell Transform (ST) [167], [200]. The HST function can mathematically express by as [167]:

$$HST_{(\tau, f_a)} = \int_{-\infty}^{+\infty} m(t) \left[\frac{2|f_a|}{\sqrt{2\pi}(\omega^f + \omega^b)} \times e^{\left[\frac{-f_a^2[R((\tau-t), \{\omega^f, \omega^b, \delta^2\})]^2}{2}\right]} \times e^{-2\pi jft} \right] dt \quad (5.3)$$

Where ω^f is the forward taper parameter, ω^b is the back taper parameter δ is the window shape controlling parameter, and R is the hyperbola function. The mathematical expression of the hyperbola function is expressed in equation (5.4) [167]:

$$R(\tau-t, \{\omega^f, \omega^b, \delta^2\}) = \left[\frac{\omega^f + \omega^b}{2\omega^f \omega^b} \right] (\tau-t-\psi) + \left[\frac{\omega^f - \omega^b}{2\omega^f \omega^b} \right] \sqrt{(\tau-t-\psi)^2 + \delta^2} \quad (5.4)$$

In equation (5.4), translational factor = ψ ; this translational factor can be used to maintain a specific peak of the hyperbolic window at $(\tau-t) = 0$, and that can be expressed in the following equation (5.5):

$$\psi = \sqrt{\frac{(\omega^f - \omega^b)^2 \delta^2}{4\omega^f \omega^b}} \quad (5.5)$$

5.2.1 Window Parameter Tuning of Hyperbolic Stockwell Transform (HST)

According to equation (5.3), it has been noticed that three boundary conditions have controlled the shape of the hyperbolic window, i.e., ω^f , ω^b and δ . Also, the aforesaid parameters are able to alter the resolution of a Time-Frequency (T-F) spectrum. Therefore, analyzing SLC signals with a fixed value of window parameters (ω^f , ω^b and δ) is technically incorrect. In previous studies, the parameters of hyperbolic window have been determined by the grid search optimization technique [196]. However, this parameter tuning method usually takes much longer to converge. The Bayesian optimization (BO) technique has been applied in this work to tune the hyperbolic window (HW) parameters.

In this paper, the reason for applying BO to fine-tune the HST window parameter is that it converges quickly for fewer iterations, and its effectiveness is not affected by the window parameter. The paper's detailed theoretical background of Bayesian Optimization can be found [167], [200]. The maximum Energy Concentration Measurement ($ECM_{(\omega^f, \omega^b, \delta)} \Big|_{\max}$) value in the T-F plane has been used as a cost function to find the optimal value of hyperbolic window parameters (ω^f , ω^b and δ). The mathematical expression of the cost function is given in the equation (5.6):

$$ECM_{(\omega^f, \omega^b, \delta)} \Big|_{\max} = \frac{1}{\int_{-\infty}^{+\infty} \int_{-\infty}^{+\infty} |\overline{HST}_{\omega^f, \omega^b, \delta}(t, f_a)| dt df_a} \quad (5.6)$$

In equation (5.6), the normalized form of the $|\overline{HST}_{\omega^f, \omega^b, \delta}(t, f_a)|$ is defined as shown in equation (5.7).

$$|\overline{HST}_{\omega^f, \omega^b, \delta}(t, f_a)| = \frac{HST_{\omega^f, \omega^b, \delta}(t, f_a)}{\sqrt{\int_{-\infty}^{+\infty} \int_{-\infty}^{+\infty} |\overline{HST}_{\omega^f, \omega^b, \delta}(t, f_a)|^2 dt df_a}} \quad (5.7)$$

Where the range of HW tuning parameters is taken, e.g., $\omega^f \leq 0.5, \omega^b \leq 1.5$ and $\delta \leq \frac{1}{f_a}$.

5.2.2 Effect of Contamination Severity on Surface Leakage Current Signal

In this study, the Cross Hyperbolic Stockwell Transform (XHST) method was used to analyze non-stationary signals in a joint time-frequency frame. In order to measure the correlation between two signals, an XHST method can be applied to a joint time-frequency plane. Accordingly, XHST provides additional information than conventional time-frequency techniques. The second advantage of XHST is the reduction of non-correlated and arbitrary noise in any two cross-correlated time signals. In other words, a cross-spectrum created by two signals disturbed by random and uncorrelated noise will not reflect their influence on outcomes [208] – [209]. Since arbitrary noise and non-correlated noise have low cross-correlation, there is no significant cross-correlation between them. In the combined time-frequency domain, the correlation between two signals can be measured using the XHST method. In this method, the degree of similarity between the two signals is illustrated in terms of strength by the intensity of the color bars.

It is noteworthy to mention that a higher correlation degree signifies an enhanced link between the two cross-correlated signals. Moreover, in the XHST technique, the output image is associated with regions in which weakly correlated signals exhibit maximum common power. This work analyses the non-linear dynamics of the SLC with contamination level through the Cross Hyperbolic Stockwell transform. In XHST, the time-frequency HST spectrum of the SLC signal is cross-correlated with a reference SLC signal. The 2D spectrum is presented as a complex 2D matrix (T). Where $T = H \times S$, H = frequency component of SLC signals and S = sample points of the SLC signals. Next, the T-matrix of SLC signals is cross-correlated with a reference SLC signal.

In this task, the SLC signal recorded for the uncontaminated SiR insulator has been considered a reference signal. The mathematical formula of XHST can be expressed as [167], [201]:

$$XHST^{i_{SLC}i_R}(jR, \frac{n}{NR}) = \left[T^{i_{SLC}}(jR, \frac{n}{NR}) \right] \times \left[T^{i_R}(jR, \frac{n}{NR}) \right]^* \quad (5.8)$$

In equation (5.8), the SLC signal of the contaminated SiR insulator is represented as i_{SLC} , and the SLC signal of the clean surface is represented as the reference signal i_R . The complex conjugate form of T-matrix for reference signal is presented in equation (5.8): $\left[T^{i_R}(jR, \frac{n}{NR}) \right]^*$.

Time-frequency Domain Analysis of Leakage current Signal of Overhead line Polymeric Insulator by Cross Hyperbolic Stockwell Transform using Fine-tuned Convolutional Neural Network Technique

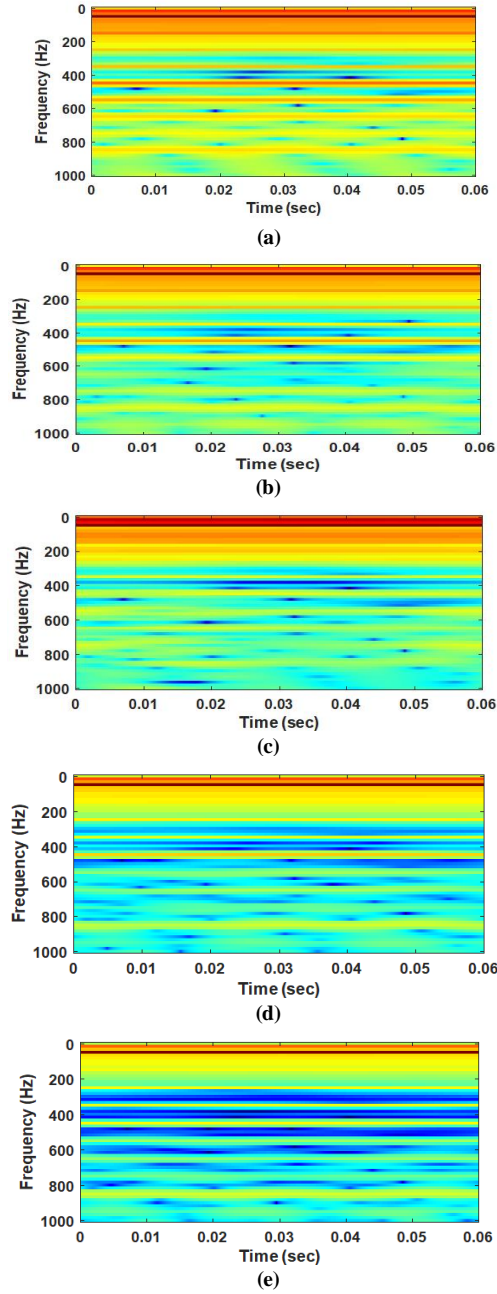


Fig. 5.1 XHST spectrum images of surface leakage current correspond to (a) Very Light (VL) (b) Light (L) (c) Moderate (M) (d) High (H) and (e) Very High (VH) surface contamination severity.

In order to obtain the time-frequency XHST spectrum, it is technically incorrect to analyze the SLC signal with a fixed value of window parameters, i.e., (ω^f , ω^b and δ). Considering this fact, the window parameters have been optimized according to the process mentioned in [29], [196]. Compared to conventional Hyperbolic Stockwell Transform, the XHST technique has some distinct advantages, such as XHST can find similarities or dissimilarities between two signals. Besides that, the random noise does not affect the time-frequency spectrums obtained through the XHST method [167], [201]. In Fig. 5.1, contamination classes of Very Light (VL), Moderate (M), and Very High (VH) have been illustrated in the cross-time-frequency spectrum of SLC signals obtained through the XHST method.

5.3 Convolution Neural Network (CNN) Based Approach

During the traditional feature extraction and classification process, quantitative and qualitative analysis are necessary for decision-making. Conventional feature classification techniques are handcrafted and time-consuming [29], [196] – [197]. In contrast, the deep learning technology used in the CNN model can automatically extract deep features and can identify the most significant features. In recent years, Convolution neural network (CNN) has gained popularity in image classification, object detection, feature extraction and many other applications [202] – [204]. It uses convolution operation to learn spatial features in an image adaptively and automatically. The CNN learns and extracts significant features through multilayered insights inspired by the natural brain's learning process. It is preferred for discriminating various classes of input images. In contrast to a separate feature extraction tool, CNN-based classification frameworks do not require a separate feature extraction tool [202] – [207].

Therefore, it replaces tedious and unsophisticated manual feature extraction. The components of a CNN architecture typically include the *input layer*, *convolution layer*, *pooling layer*, *fully connected layer* and *output layer*. Notably, the *convolution layer*, *pooling layer*, and *fully connected layer* serve as the main functional layers of the CNN model. The first two layers are responsible for feature extraction, whereas the last layer maps the learned features for classification purposes [199]. Finally, the SoftMax layer provides the probabilistic values with the help of a trained model and predicting the contamination class from the input dataset (i.e., images) is possible. A brief overview of CNN's architecture is presented below.

- **Convolutional Layer:** Kernels are the basic building blocks of the CNN architecture. These kernels are used as filter blocks to process the input images. During image processing, the kernels organize themselves individually with the dimension (i.e., height and width) of each input image. These kernels are capable of extracting 2D feature sets from input images [199] – [204]. The convolutional layer consists of an activation function layer, known as a Rectified Linear Unit (ReLU). It is stipulated that ReLU causes an increase in CNN nonlinearity.

Time-frequency Domain Analysis of Leakage current Signal of Overhead line Polymeric Insulator by Cross Hyperbolic Stockwell Transform using Fine-tuned Convolutional Neural Network Technique

- **Pooling Layer:** The pooling layer, which comes before the ReLu layer, streamlines each convolutional layer's output while retaining significant data. It is noteworthy that after the pooling layer, the output features will decrease, but they will still include the most significant features of the previous feature map. Moreover, network overfitting is additionally controlled by pooling layers [204]. The fully connected (or FC layer) layer receives the outcome of the pooling layer for feature prediction.
- **Fully Connected (FC) Layer:** The FC layers help to transform a 2D feature map into 1D features matrix. Through the encoded 1D feature vector, the FC layer determines the score for each input image. In order to estimate the probable class of image data, scores are converted into probabilistic values by the SoftMax layer based on the training model [204]. Fig. 5.2 shows a typical CNN architecture schematic diagram [202].

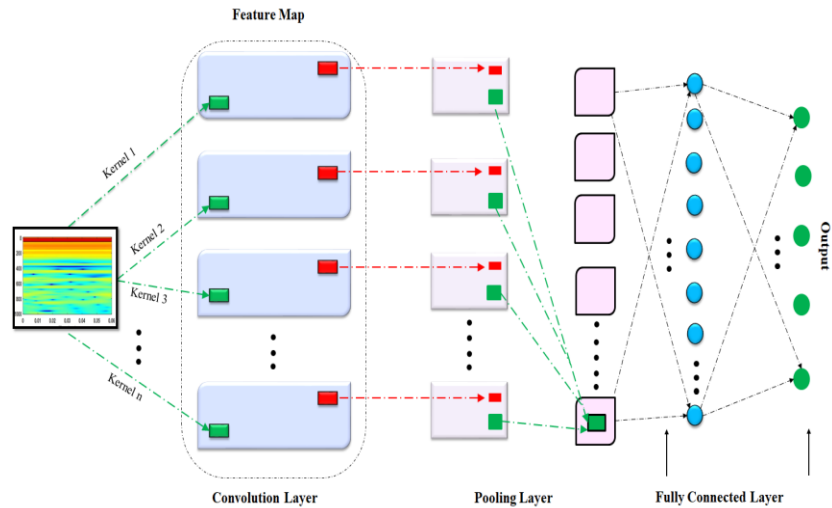


Fig. 5.2 Schematic diagram of Convolutional Neural Network (CNN) architecture [202].

In this work, to extract features from the joint time-frequency XHST spectrum image, a deep learning framework was used. The automated feature extraction procedure is a benefit of the deep learning framework.

5.3.1 Transfer Learning Aided Fine-Tuning Approach to Proposed CNN Model

The conventional manual feature extraction processes are time-consuming and there is the possibility of data being lost. This traditional approach requires quantitative and qualitative analysis for decision-making [196] – [198]. Although CNN is very useful for the image-related task, but the training of a CNN model from scratch has some limitations, which are reported as follows:

- i. Massive amounts of data should be required to train a network from scratch and with the limited amount of data there is a possibility that the CNN model may overfit the training data [202] – [204].
- ii. The weights are randomly initialized in a deep CNN model. These weights are updated after each iteration during the network training based on the loss function and labelled data. However, it involves a computational challenge while updating the weights of all layers [202] – [205].

Considering the above-mentioned limitations, this article adopts transfer learning with a fine-tuning strategy to identify contamination classes from the T-F plane SLC signal. As the name suggests, in Transfer Learning (TL), knowledge learned previously from a pre-trained model has been applied to a new task. The application of transfer learning is prevalent in various engineering problems [202] – [205]. It should be mentioned here that the TL-based approach is convenient on a limited dataset. Also, this approach works faster than the network trained from scratch [202] – [205].

In this work, a popular deep CNN model named VGGNet-16 has been applied to classy SLC signal converted XHST spectrum images [205]. In addition, before being fed as inputs, the XHST images were resized to $(227 \times 227 \times 3)$ into the proposed CNN module. Table 5.1 presents the training parameters for the proposed CNN architecture, including the minimum batch size, number of epochs, testing frequency, and learning rate. The Adam Optimizer has been employed in order to scale the learning rate for each network weight. The cross-entropy has been chosen as a loss function for the proposed CNN model. Fig. 5.3 illustrates the training and validation performance of the proposed CNN module with the XHST image datasets.

In this fine-tuning strategy, the last three convolutional block of VGGNet16 have been fine-tuned, whereas the top three convolutional blocks have been kept frozen. The bottom convolutional block can capture significant information from the input image [29], [205].

Time-frequency Domain Analysis of Leakage current Signal of Overhead line Polymeric Insulator by Cross Hyperbolic Stockwell Transform using Fine-tuned Convolutional Neural Network Technique

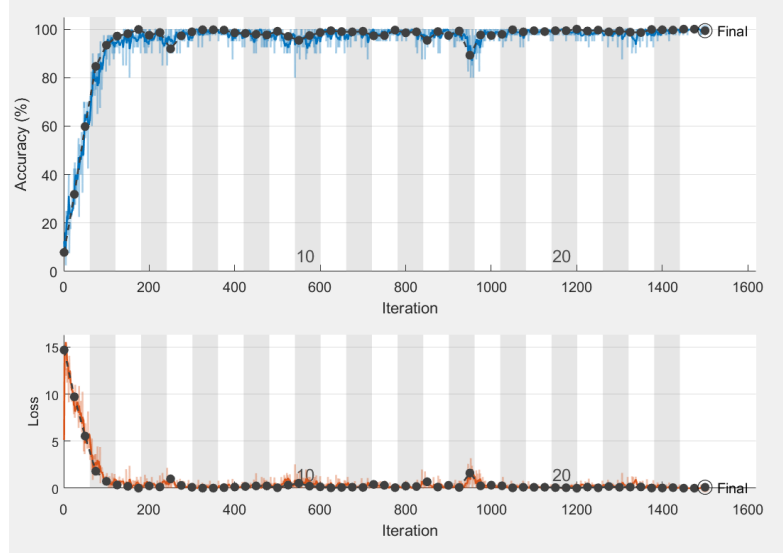


Fig. 5.3. Training and validation performance of the proposed CNN module using XHST image dataset.

In addition, Fig. 5.4 illustrates an overview of the proposed transfer learning framework with a fine-tuning strategy to identify contamination classes. Due to the fact that this assignment consists of five classes, the number of neurons in the final FC layer has been maintained at five.

Table 5.1 Training Parameter of Pre-trained VGGNet-16 Model.

Sl. No.	Tuning Parameters	Technical Details
1	Learning Rate	0.0001 ms
2	Minimum Batch Size	100
3	Testing Frequency	50 Hz
4	Number of Epochs	30
5	Loss Function	Cross Entropy
6	Solver	Adam Optimizer

Table 5.1 shows the training parameters during VGGNet-16 fine-tuning. It is essential to mention that it took around 35 minutes (approx.) to train the

proposed model. An Intel® Core™ i5 (7200U, CPU @ 2.50 GHz to 2.71 GHz) processor paired with 24 GB (DDR4) RAM and 2 GB of graphics memory (NVIDIA GeForce 940MX) was used to carry out the VGGNet-16 architecture's fine-tuning process. The training of the proposed VGGNet-16 architecture has been implemented on Python and Keras Library-based TensorFlow2 platforms.

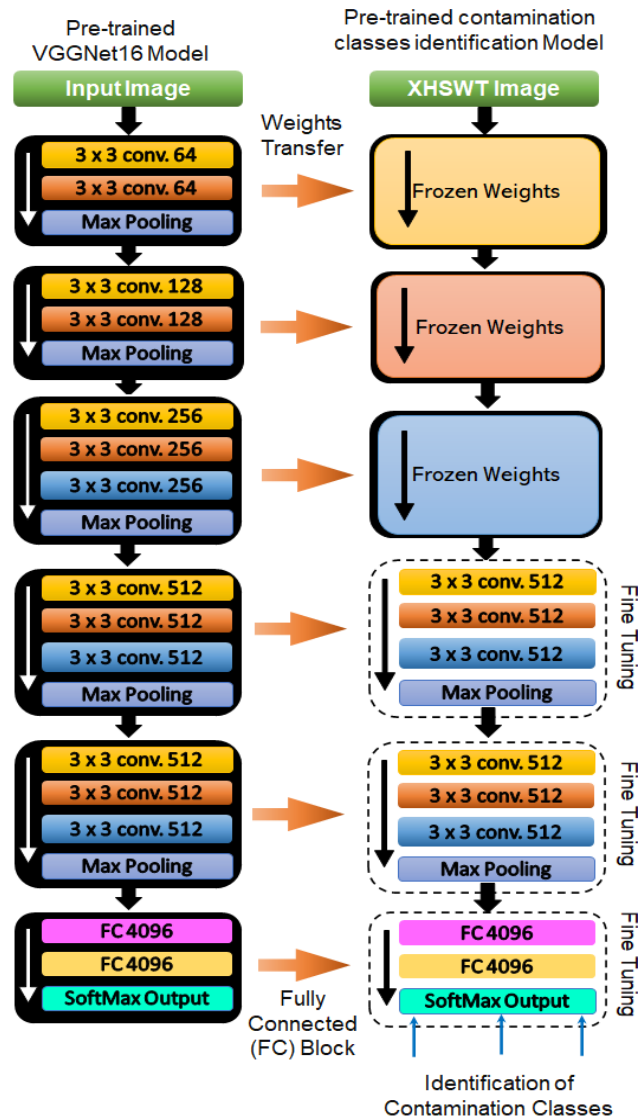


Fig. 5.4 Proposed transfer learning framework with a fine-tuning strategy to identify contamination classes.

5.4 Results and Discussions

This work is aimed to detect the degree of contamination of overhead SiR insulators using an SLC signal. In order to accomplish this, five distinct contamination levels were used to acquire the SLC signals of 11 kV SiR insulator samples. It is worth mentioning that 400 SLC signals were stored for each of the classes of contamination, that is, a total of 2000 SLC signals were recorded for all classes. After that, time-frequency XHST images are produced from the recorded SLC signals. After that, the XHST method's image dataset was fed to a pre-trained deep CNN architecture (i.e., VGGNet-16) for automated feature extraction and contamination severity detection. The classification performance of the proposed framework and comparative study are discussed in the following sections.

5.4.1 Evaluation of the Proposed Framework's Performance

Three statistical parameters including accuracy, precision, and specificity have been utilized to evaluate the effectiveness of the proposed model [205] – [208]. The aforementioned statistical parameters have been measured after the five-fold cross-validation technique [205], [208]. In Table 5.2, the result of the comprehensive study has been presented. The result shows that after an initial improvement, the classification performance almost saturates after fine-tuning the 3rd convolution block of VGGNet-16. However, the computational time has increased rapidly with the number of fine-tuned convolutional blocks. This is because the number of trainable parameters in VGGNet-16 increases with the number of fine-tuned convolution blocks. Considering the computational time and accuracy, the VGGNet-16 model fine-tuned up to the 3rd convolution block (i.e., from the bottom) should be considered for real-life implementation.

Table 5.2 Performance of Fine-Tuned Proposed CNN Model for Different Training Parameters

Sl. No.	Number of fine-tuned Convolution block	Training time / epoch (p.u.)	Accuracy (%)
1	Block - 0	1	97.65
2	Block - 1	2.34	98.35
3	Block - 2	4.56	99.20
4	Block - 3	7.89	99.70
5	Block - 4	9.98	99.75
6	Block - 5	11.12	99.75

The presented framework's elaborate performance is illustrated in Table 5.3. It can be inferred from the outcome that the proposed framework has exhibited excellent results. As a result, the proposed framework is perfectly acceptable for use in practical implementation. Three indices such as "Accuracy", "Precision" and "False Positive Rate (FPR)" have been used to assess the performance of the proposed CNN architecture [209]. For the purpose of determining the efficiency of the proposed architecture, five-fold cross-validation has been applied. For each class of surface contamination, the average value is reported in Table 5.3 after five repetitions. According to the results, the proposed CNN module returned outstanding performance results for the XHST image dataset. In this regard, the proposed deep-learning framework appears robust for predicting contamination classes.

Table 5.3 Performance of Pre-Trained Proposed CNN Model.

SI. No.	Contamination Classes (CL)	Accuracy (%)	Precision (%)	False Positive Rate (FPR) (%)
1	CL-Very Light	99.5	99.75	99.93
2	CL- Light	99.25	99.5	99.87
3	CL-Medium	100	99.5	99.87
4	CL-High	100	99.75	99.93
5	CL-Very High	99.75	100	100
6	Overall	99.70	99.70	99.93

5.4.2 Impact of Fine-Tuning on Pre-Trained Architecture System

In this section, the impact of the number of the fine-tuned layer in the VGGNet-16 model has been rigorously analyzed. For this purpose, the number of trainable parameters has been varied; in other words, the number of fine-tuned convolution blocks has been iteratively increased and the performance has been assessed. The amount of fine-tuning, the size of the most recent input dataset, how similar the input dataset is to the pre-training dataset, and other factors are often used to determine how the suggested VGGNet-16 model is tuned. By using pre-trained models that are appropriate for the assessment of particular duties. Apart from this, it is a successful method for reducing time and labor in training updated models.

5.4.3 Comparison with other Time-Frequency Imaging Techniques

To get better insight into the efficacy of the proposed framework, the performance of the VGGNet-16 involving other time-frequency imaging techniques has also been investigated in this section. For this purpose, the time-frequency spectrum image of acquired SLC signals has been obtained through other time-frequency methods such as Hyperbolic Stockwell Transform (HST), Stockwell Transform (ST), and Cross-Stockwell Transform (XST), respectively. Each time-frequency image dataset has been analyzed using a fine-tuned VGGNet-16 model to identify the contamination classes of SiR insulators. It is worth mentioning that a comparison study on the performance with aforesaid time-frequency methods has been shown in Table 5.4. The XHSWT time-frequency representation should be considered for identifying the degree of contamination of overhead line insulators, according to the analysis.

Table 5.4 Comparison Study with Different Time-Frequency Strategies.

Time-Frequency Methods	Accuracy (%)
Stockwell Transform (ST)	98.65
Hyperbolic Stockwell Transform (HST)	99.05
Cross Stockwell Transform (XST)	99.15
Cross-Hyperbolic Stockwell Transform (XHST)	99.70

5.4.4 Validation with Different Dimensions SiR Insulator

The SLC signal recorded from the SiR insulator in various dimensions served as evidence to support the effectiveness of the proposed model. A 33 kV rated SiR insulator sample was used for validation purposes. Table 5.5 contains the 33 kV rated SiR insulator's technical specifications. The insulator sample was then contaminated and the SLC signals were acquired accordingly (as shown in Fig. 5.5).

Table 5.5 Technical Specification of 33 kV SiR Insulator.

Sl. No.	Parameters	Specifications
1	Rated Voltage	33 kV
2	Creepage distance	900 mm
3	Section length	545 mm

It is worth noting that 500 SLC signals (100 per class) were recorded for validation. That means each surface contamination class had 100 numbers of surface leakage current signal data. After that, the SLC signals were converted into XHST images in the time-frequency (T-F) domain. Those image datasets were fed to a proposed pre-trained VGGNet-16 architecture for identifying the intensity of surface contamination.

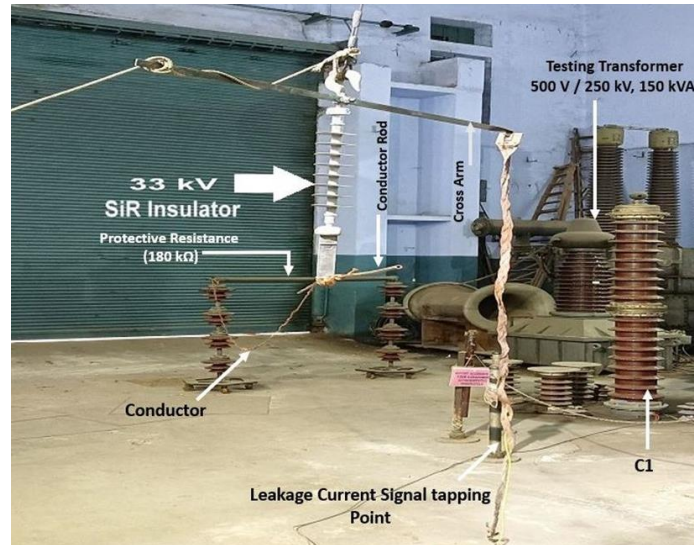


Fig. 5.5 Image of Actual Hardware Setup for SLC Measurement using of 33 kV rated SiR Insulator.

According to the results shown in Fig. 5.6, the proposed method can be deduced to be capable of monitoring the SiR insulator's condition in any dimension.

True Class	1	99	1			
	2		100			
	3		2	98		
	4			3	97	
	5				2	98
		1	2	3	4	5
		Predicted Class				

Fig. 5.6 Validation Performance of the Proposed CNN framework.

5.5 Conclusion

This article presents an advanced technique to estimate the contamination level of the SiR insulator. This technique analyses the SLC signal of SiR insulators through the time-frequency (T-F) method. It demonstrates that joint T-F plots of SLC signal obtained through the XHST method can provide in-depth information about the contamination level of the SiR insulator. After that, the XHST method's image dataset was then fed to a pre-trained deep CNN architecture (i.e., VGGNet-16) for automated feature extraction and contamination severity detection. In this proposed technique, no handcrafted feature extraction techniques have been used. A comparison study with the existing method also revealed that the proposed method produced superior results to those of other time-frequency methods, as per the outcome. The automatic feature extraction process used by the proposed deep learning VGGNet-16 architecture is very sophisticated. As a result, the model performs better since it can select the attributes that are most pertinent to the input dataset. Additionally, by retraining the model on the fresh input dataset, it is simple to adapt it to the new set of objectives. Notably, the proposed deep learning system becomes extremely resilient and flexible. Apart from this, in comparison with handcrafted feature-based and conventional time-frequency aided deep learning frameworks (i.e., reported in the previous chapters), cross-spectrum deep learning frameworks performed better in mean recognition interpretation.

Hence, it can be summarized that the proposed technique can be used to estimate the level of contamination in any dimension's SiR insulator in real-time. The proposed technique makes it possible to detect surface contamination of overhead line insulator in its early stages, allowing for proactive maintenance and reducing the risk of power outages. It also results in lower maintenance costs and a more reliable along with an efficient system.

Chapter 6

Conclusions and Future Scope

6.1 Conclusion

The purpose of this dissertation is to address some factors that contribute to the degradation of overhead line insulators. Environmental pollutants and moisture association cause severe surface contamination in overhead line insulators. Pollutants can be accumulated on the surface of overhead line insulators which creates conductive layers. This leads to the initiation of leakage current flow along the surface of overhead line insulators. The flow of leakage current on the surface is more rapid and noticeable when moisture is associated with pollutants. Due to this, dry bands may develop at various points on the external surface due to an increase in current density. There can be a variety of consequences caused by these dry bands:

- Overhead lines can cause overheating and non-uniform voltage distribution stress across the surface of insulators.
- Insulating property of overhead line insulators can degrade due to rapid leakage current flow through the surface.
- The development of tracking and erosion on the housing of overhead line insulators can lead to surface flashover.

Through the analysis of leakage current profiles of overhead line insulators, the dissertation aims to understand leakage current dynamics associated with surface contamination severity. Therefore, early identification of surface contamination of overhead line insulators is imperative for preventing premature failure of overhead line insulators, which contributes to power system reliability. The degree of surface contamination of overhead line insulators can be estimated by conventional techniques, which is direct measurement of equivalent salt deposit density (ESDD). In spite of this, ESDD measurement is a time-consuming and cumbersome technique. It has been observed experimentally that leakage current profiles become non-stationary and distorted with increasing of surface contamination severity.

In this regard, the severity of surface contamination was artificially prepared in the laboratory as per the IEC 60507 standard. In the laboratory, five different classes of artificial contamination slurry were prepared according to the standard (i.e., IEC 60507) using different proportions of mixture of NaCl, Kaolin and distilled water. The slurry was applied to the overhead line insulator's surface to prepare the insulator sample. Afterward, the samples were kept for 24 hours to dry. According to IEC 60507, the detailed sample preparation has been discussed in *Chapter 2* (Section 2.2.1). In order to acquire the surface leakage current (SLC) data from the various

contaminated samples, an experimental setup was developed in the laboratory. The SLC data was acquired and was stored on the computer for data analysis purposes. The elaborate discussion about the experimental setup has been demonstrated in *Chapter 2* (section: 2.2.2).

In *Chapter 3*, mathematical morphology has been employed for analysis of SLC, as demonstrated. Notably, mathematical morphology can be very useful for analyzing non-stationary signals due to its ability to extract temporal characteristics. After that, the extracted features were fed to a Random Forest (RF) classifier to identify the contamination level of overhead line insulators. The results show that features of mathematical morphology can predict overhead line insulators' surface contamination severity with satisfactory results for the RF classifier. Apart from this, the proposed filter technique can efficiently provide optimal features, which improve the proposed framework's prediction accuracy. Moreover, the method can be applied to other types of non-stationary signals. On the contrary, employing the proposed filter model with Mathematical Morphology operation for acquiring features from SLC signals is time-consuming and cumbersome. In addition, the mathematical morphological technique depends on structural element dimensions. Assigning structural elements depends on the signature of the input signal, which is the trickiest. Notably, the proposed model's success rate was examined with only one machine learning classifier (i.e., Random Forest). It is impractical to accurately validate the surface contamination level of overhead line insulators by testing just one classifier at a time.

For this reason, in *Chapter 4*, the author reported an integrated time-frequency signal processing technique applied to SLC signals to overcome the flaws mentioned in the mathematical metaphorical-based model. Using a data acquisition system, SLC signals of different contamination classes were acquired and converted into a joint time-frequency image data bank by Hyperbolic Stockwell Transform (HST). In addition, HST provided different statistical features from the image bank as output features. Optimal features were extracted using the LASSO regression technique to predict surface contamination levels of overhead line insulators accurately. Notable, the framework's performance was compared with four standard classifiers for validation, such as Support Vector Machine (SVM), Random Forest (RF), Gaussian Naive Bayes (GNB) and k-Nearest Neighbor (k-NN). The proposed model's performance is unaffected by external noise and aliasing effects. Additionally, the framework reported here does not depend on structural element dimensions. On the other hand, the proposed framework's feature classification process is a supervised learning approach, which is cumbersome. The generated features matrix from the HST method can only be utilized if it is arranged as input and output variables for supervised feature classification. The classifier models must perform iterative operations based on the training dataset to predict the correct contamination level. It has been observed that the proposed model's algorithm is terminated when it reaches an acceptable performance level. That is why it is time-consuming to predict the contamination class of the overhead line insulators.

Conclusions and Future Scope

In **Chapter 5**, by using the cross hyperbolic stockwell transform (XHST) approach, the distinct characteristics of surface leakage current (SLC) signals at different surface contamination levels of overhead line insulator samples were revealed. Also, the extracted features are not affected by external noise and the aliasing effects. Furthermore, the XHST method was a powerful tool for detecting surface contamination because it is cross-correlated with a reference signal (i.e., the SLC at the clean surface of overhead line insulator). In addition, time-frequency cross-spectrum images are fed to a pre-trained CNN architecture (i.e., VGGNet-16). Automatic feature extraction and classification have been achieved using the transfer learning strategy with fine-tuning techniques to train VGGNet-16 architecture. The performance of the proposed model is validated for any dimension of the overhead line SiR insulator. In a deep learning framework, feature extraction is fully automated and the abundant features are eliminated without any supervision. The cross-spectrum deep learning framework described here is simple, accurate, and robust, which makes it potentially suitable for predicting overhead line insulators' surface contamination severity. The pre-trained deep VGGNet-16 architectures' major advantage is automatic feature extraction and prediction of the contamination classes. This significantly reduces the effort and time needed to develop a model for a specific task. Furthermore, the pre-conditioned models can be further fine-tuned over a few epochs to validate the model performance for any dimension's overhead line insulators.

6.2 Scope of Future Work

In this dissertation, several techniques have been proposed for condition assessment of overhead line insulators in service. These techniques are potentially worthy to implement in real time offline condition assessment of overhead line insulators. This study's outcomes can support scientists currently exploring techniques for monitoring the condition of different types of overhead line insulators. Some of the future scopes in this research field have been mentioned below.

Development of a visual based condition monitoring framework to estimate the life of the any types of overhead line insulators. Although, surface leakage current spectrum can estimate the life of the overhead line insulators effectively but all the proposed framework are suitable for offline condition assessment. Therefore, infrared thermal images of overhead line insulators at different surface contamination level can be analyzed through advanced image processing technique on-line. The thermal infrared imaging-based approach can more effectively predict surface contamination level as well as and life span of that insulator. The main advantage of thermal infrared imaging is that it can be utilized in any environmental conditions or at any location, such as outdoor or indoor applications. Most importantly, the visual imaging technique has no dependency on input voltage levels to monitor the condition of overhead line insulators. Moreover, image classification based online monitoring techniques are more efficient than the conventional techniques.

Therefore, it is appropriate to mention here that this dissertation has presented certain approaches for condition monitoring of in-service overhead line insulators. However, a more accurate picture regarding the practical implementation of these approaches will emerge with the deployment of field monitoring devices that would be developed based on the proposed methods. The field monitoring devices can be practically implemented for real time condition assessment of overhead line insulators.

References

- [1] R. S. Gorur et al., "Aging in silicone rubber used for outdoor insulation," in *IEEE Trans. on Power Delivery*, vol. 7, no. 2. pp. 525-538, 1992.
- [2] J. P. Reynders, I. R. Jandrell and S. M. Reynders, "Review of aging and recovery of silicone rubber insulation for outdoor use," in *IEEE Trans. on Dielectrics and Electrical Insulation*, vol. 6, no. 5, pp. 620-631, Dec. 1999.
- [3] R. Chakraborty and B. S. Reddy, "Studies on high temperature vulcanized silicone rubber insulators under arid climatic aging," in *IEEE Trans. on Dielectrics and Electrical Insulation*, vol. 24, no. 3, pp. 1751-1760, June 2017.
- [4] X. Jiang et al., "Effect of arc-levitating from polluted insulators' surface in the low air pressure on its DC flashover performance," in *IET Generation, Transmission & Distribution*, vol. 5, no. 7 pp. 729-734, 2011.
- [5] X. Jiang et al., "Comparison of DC Pollution Flashover Performances of Various Types of Porcelain, Glass, and Composite Insulators," in *IEEE Trans. on Power Delivery*, vol. 23, no. 2, pp. 1183-1190, April 2008.
- [6] Y. Gao et al., "Comparative Investigation on Fracture of Suspension High Voltage Composite Insulators: A Review—Part I: Fracture Morphology Characteristics," in *IEEE Electrical Insulation Magazine*, vol. 37, no. 3, pp. 7-17, May/June 2021.
- [7] M. M. Hussain et al., "Mechanism of saline deposition and surface flashover on outdoor insulators near coastal areas part II: Impact of various environment stresses," in *IEEE Trans. on Dielectrics and Electrical Insulation*, vol. 24, no. 2, pp. 1068-1076, April 2017.
- [8] M Akbar, R Ullah and S Alam, "Aging of silicone rubber-based composite insulators under multi-stressed conditions: an overview," in *Materials Research Express*, vol. 6, no. 10, 6th September 2019.
- [9] H. Zha et al., "The Characteristic Analysis of ESDD and NSDD Detection of Composite Insulators Based on Hyperspectral Technology," in *IEEE Transactions on Instrumentation and Measurement*, vol. 72, pp. 1-8, 2023, Art no. 4502108.
- [10] Xidong Liang and Jianjun Dai, "Analysis of the acid sources of a field brittle fractured composite insulator," in *IEEE Trans. on Dielectrics and Electrical Insulation*, vol. 13, no. 4, pp. 870-876, Aug. 2006.

References

- [11] B. S. Reddy and P. C. Ramamurthy, "Analysis of in-service composite insulators used in overhead railway traction," in *Engineering Failure Analysis*, vol. 108, no. 104227, ISSN 1350-6307, 2020.
- [12] S. M. Rowland et al., "Electrical and material characterization of field-aged 400 kV silicone rubber composite insulators," in *IEEE Trans. on Dielectrics and Electrical Insulation*, vol. 17, no. 2, pp. 375-383, April 2010.
- [13] J. -P. Habas et al., "Effects of electric partial discharges on the rheological and chemical properties of polymers used in HV composite insulators after railway service," in *IEEE Trans. on Dielectrics and Electrical Insulation*, vol. 16, no. 5, pp. 1444-1454, Oct. 2009.
- [14] H. Khan, Md. Amin and A. Ahmad, "Characteristics of silicone composites for high voltage insulations," in *Reviews on Advanced Materials Science*, vol. 56, no. 1, pp. 91-123, 2018.
- [15] B. Venkatesulu and M. J. Thomas, "Erosion resistance of alumina-filled silicone rubber nanocomposites," in *IEEE Trans. on Dielectrics and Electrical Insulation*, vol. 17, no. 2, pp. 615-624, April 2010.
- [16] Y. Gao et al., "Comparative Investigation on Fracture of Suspension High Voltage Composite Insulators: A Review—Part II: Chemical Properties and Criteria System," in *IEEE Electrical Insulation Magazine*, vol. 37, no. 4, pp. 18-30, July/August 2021.
- [17] Pleșa et al., "Properties of Polymer Composites used in High-Voltage Applications," in *Polymers*; vol. 8, no. 5, pp. 173, 2016.
- [18] R. Verma and B. S. Reddy, "Tracking and erosion resistance of LSR and HTV silicon rubber samples under acid rain conditions," in *IEEE Trans. on Dielectrics and Electrical Insulation*, vol. 25, no. 1, pp. 46-52, Feb. 2018.
- [19] Rashid et al., "Investigation of 9000 hours multi-stress aging effects on High-Temperature Vulcanized Silicone Rubber with silica (nano/micro) filler hybrid composite insulator," in *Plos one*, vol. 16, no. 7, 2021.
- [20] Y. Xue et al., "Comparison of ATH and SiO₂ fillers filled silicone rubber composites for HTV insulators," in *Composites Science and Technology*, vol. 155, pp. 137-143, 2018.
- [21] H. Khan et al., "Investigation of electrical, tracking/erosion, and water absorption resistance properties of ATH-SiO₂-reinforced RTV-SiR composites for high-voltage insulations," in *Journal of Elastomers & Plastics*, vol. 50, no. 6 pp. 501-519, 2018.

References

- [22] M. T. Nazir et al., "Effects of thermal properties on tracking and erosion resistance of micro-ATH/AlN/BN filled silicone rubber composites," in *IEEE Trans. on Dielectrics and Electrical Insulation*, vol. 25, no. 6, pp. 2076-2085, Dec. 2018.
- [23] R. S. Gorur et al., "Mold growth on nonceramic insulators and its impact on electrical performance," in *IEEE Trans. on Power Delivery*, vol. 18, no. 2, pp. 559-563, April 2003.
- [24] S. Liu et al., "Influence of Liquid Type Filler and Coupling Agent on the Interface Resistivity Between Silicone Rubber and Fiber Reinforced Plastic," in *IEEE Trans. on Dielectrics and Electrical Insulation*, vol. 28, no. 4, pp. 1207-1215, August 2021.
- [25] T. Jiang et al., "Impact of Water Permeation on the Dielectric Response of HTV Silicone Rubber," in *2020 IEEE International Conference on High Voltage Engineering and Application (ICHVE)*, pp. 1-4, 2020.
- [26] Wang Z et al., "Effects of aging on the structural, mechanical, and thermal properties of the silicone rubber current transformer insulation bushing for a 500 kV substation," in *Springer plus*, 2016.
- [27] IEC-60093:1980, "Methods of test for volume resistivity and surface resistivity of solid electrical insulating materials," 1980.
- [28] J. Ma, X. Wang, R. Zhang, Z. Qi and W. Wang, "Influence of Sheath Radial Crack on Flashover Arc and Leakage Current of Roof Silicon Rubber Insulator for High-Speed Train," in *IEEE Access*, vol. 10, pp. 19720-19731, 2022.
- [29] K. Sit et al., "Condition Monitoring of Overhead Polymeric Insulators Employing Hyperbolic Window Stockwell Transform of Surface Leakage Current Signals," in *IEEE Sensors Journal*, vol. 21, no. 9, pp. 10957-10964, May, 2021.
- [30] J.Y. Li, C.X. Sun and S.A. Sebo, "Humidity and contamination Severity Impact on Leakage Currents of Porcelain Insulators" in *IET Gener. Trnas. Distrib.*, vol.5, pp. 19-28, 2009.
- [31] S. Chandrasekar et al., "Investigations on Leakage Current and Phase Angle Characteristics of Porcelain and Polymeric Insulator Under Contaminated Conditions", in *IEEE Trans. Dielectric and Electrical Insulation*, vol. 16, pp. 574-583, 2009.
- [32] K. Petcharaks et al., "An Investigation of ESDD on Porcelain Insulators Along the Coastal Region of Thailand", in *Proc. IEEE Int. Conf. (TENCON)*, Thailand, 2004.
- [33] H. Homma et al., "Comparison of Leakage Current Properties between Polymeric Insulators and Porcelain Insulators Under Salt Polluted Conditions", in *Proc. IEEE Int. Conf. on Elec. Insul. Materials (ISEIM)*, Japan, 2005.

References

- [34] S. Chandrasekar et al., "Investigations on Flashover Performance of Porcelain Insulators Under Contaminated Conditions", in *Proc. Nat. Conf. on Elec. Engg. Embedded Sys. (NCEEE)*, pp.112-116, 2008.
- [35] Nasir, Algeelani, M. Afendi and M. Piah, "Characterization of Acoustic Signals Due to Surface Discharges on H.V. Glass Insulators Using Wavelet Radial Basis Function Neural Networks", in *J. Appl. Soft Comp.*, vol. 12, pp. 1239-1246, 2012.
- [36] TF 33.04.03 CIGRE: "Insulation pollution monitoring", in *Eleatra*, no. 152, pp.79-89, Paris, France, 1994.
- [37] Z. Zhong, Y. Chen, Y. Liu, S. Hou, J. Geng, "Study On the Influence Mechanism Of Ambient Humidity On The Temperature Rise Of Decay-like Composite Insulators", in *High Voltage*, vol. 7, no. 5, p. 916-924, 2021.
- [38] S. Gao et al. "A Comparative Study of Abnormal Heating Composite Insulators." in *Polymers*, vol. 15, no. 13, Jun. 2023.
- [39] Bielecki et al. "Impact of increased temperature of lower end-fitting of a composite long rod insulator on its mechanical strength under variable loads." in *Archives of Electrical Engineering*, vol. 72, no. 2, pp. 391 – 405, 2023.
- [40] IEC 61109, "Insulators for overhead lines – Composite suspension and tension insulators for a.c. systems with a nominal voltage greater than 1000 V – Definitions, test methods and acceptance criteria", 2008.
- [41] Y. Mizuno, H. Kusada and K. Naito, "Effect of climatic conditions on contamination flashover voltage of insulators," in *IEEE Transactions on Dielectrics and Electrical Insulation*, vol. 4, no. 3, pp. 286-289, June 1997.
- [42] Y. Tu et al., "Moisture induced local heating of overhead line composite insulators," in *IEEE Transactions on Dielectrics and Electrical Insulation*, vol. 24, no. 1, pp. 483-489, Feb. 2017.
- [43] Y. Chen, Y. Chen, Y. Liu, S. Hou, J. Geng, "Study On the Influence Mechanism Of Ambient Humidity On The Temperature Rise Of Decay-like Composite Insulators", in *High Voltage*, vol. 7, no. 5, pp. 916-924, 2021.
- [44] Z. Yuan, Y. Tu, H. Jiang, C. Wang, C. Wang, "Study On Heating Mechanism Of Grp Rod In a Composite Insulator", in *IET Science, Measurement & Technology*, vol. 13, no. 1, p. 108-113, 2019.
- [45] Y. Tu et al., "Effect of moisture on temperature rise of composite insulators operating in power system," in *IEEE Transactions on Dielectrics and Electrical Insulation*, vol. 22, no. 4, pp. 2207-2213, August 2015.

References

- [46] Z. Jiang, X. Jiang, Y. Guo, Y. Hu, Z. Meng, "Pollution Accumulation Characteristics of Insulators Under Natural Rainfall", in *IET Generation, Transmission and Distribution*, vol. 11, no. 6, p. 1479-1485, 2017.
- [47] Z. Jiang, X. Jiang, Z. Zhang, Y. Guo, and Y. Li, "Investigating the Effect of Rainfall Parameters on the Self-Cleaning of Polluted Suspension Insulators: Insight from Southern China," in *Energies*, vol. 10, no. 5, p. 601, May 2017.
- [48] M. M. Hussain, S. Farokhi, S. G. McMeekin and M. Farzaneh, "Contamination performance of high voltage outdoor insulators in harsh marine pollution environments," in *2017 IEEE 21st International Conference on Pulsed Power (PPC)*, pp. 1-6, Brighton, UK, 2017.
- [49] D. Sharma and S. Reddy B., "Studies on High Voltage Composite Insulators under very low Temperature," in *2018 IEEE International Conference on High Voltage Engineering and Application (ICHVE)*, pp. 1-4, Athens, Greece, 2018.
- [50] S. Thong-Om et al., "Comparison Ageing Deterioration of Silicone Rubber Outdoor Polymer Insulators in Artificial Accelerated Salt Fog Ageing Test", in *World Academy of Science, Engineering and Technology, Open Science Index 60, International Journal of Materials and Metallurgical Engineering*, vol. 5, no. 12, pp. 1110 - 1119, 2011.
- [51] E. Kuffel, W. S. Zaengl, and J. Kuffel, "High Voltage Engineering: Fundamentals," in 2nd Edition. *Oxford: Butterworth-Heinemann*. ISBN: 0750636345, 2000.
- [52] J. Wang, X. -d. Liang, L. -h. Chen and Y. Liu, "Combined effect of different fields on the motion characteristics of dust particles around the insulators," in *2011 Annual Report Conference on Electrical Insulation and Dielectric Phenomena*, pp. 373-376, Cancun, Mexico, 2011.
- [53] A. Salem et al., "Risk Assessment of Polluted Glass Insulator Using Leakage Current Index Under Different Operating Conditions," in *IEEE Access*, vol. 8, pp. 175827-175839, 2020.
- [54] M. Jiang et al., "Dust contamination on surface of transmission line insulators in air-polluted regions in China: statistical characteristics, adhesion mechanism, and environmental impact factors," in *Environmental Science and Pollution Research*, vol. 27, pp. 23643–23654, 2020.
- [55] Li et al., "Dust Figures as a Way for Mapping Surface Charge Distribution — A Review," in *IEEE Transactions on Dielectrics and Electrical Insulation*, vol. 28, no. 3, pp. 853-863, June 2021.

References

- [56] R. Verma et al., "Multi-stress aging studies on polymeric insulators," in *IEEE Trans. on Dielectrics and Electrical Insulation*, vol. 25, no. 2, pp. 524-532, April 2018.
- [57] Khattak and Md. Amin, "Influence of stresses and fillers on the aging behaviour of polymeric insulators," in *Rev. Adv. Mater. Sci*, vol. 44, pp. 194-205, 2016.
- [58] IEC 60071: "Insulation Coordination", Part 1: Terms, Definitions, Principles and Rules (1993), Part 2: Application Guide, 1996.
- [59] C. Baker et al., "High Voltage Insulators Mechanical Load Limits— Part I: Overhead Line Load and Strength Requirements," in *IEEE Transactions on Power Delivery*, vol. 27, no. 3, pp. 1106-1115, July 2012.
- [60] Ramirez, R. Hernandez and G. Montoya, "Measurement of Leakage Current for Monitoring the Performance of Outdoor Insulators in Polluted Environments," in *IEEE Electr. Insul. Mag.*, vol. 28, no. 4, pp. 29-34, 2012.
- [61] Subba Reddy and G. R. Nagabhushana, "Study of Leakage Current Behaviour on Artificially Polluted Surface of Ceramic Insulator", in *Plasma Sci. & Tech.*, vol.1.5, no. 4, pp. 1921-1926, 2003.
- [62] K Aggarwal et al., "An overview of the condition monitoring of overhead lines," in *Electric Power Systems Research*, vol. 53, no. 1, pp. 15 -22, 2000.
- [63] L. He and R. S. Gorur, "Source strength impact analysis on polymer insulator flashover under contaminated conditions and a comparison with porcelain," in *IEEE Transactions on Dielectrics and Electrical Insulation*, vol. 23, no. 4, pp. 2189-2195, August 2016.
- [64] L. Xia et al., "Aging Evaluation of Silicone Rubber Composite Insulators with Long-Term Operation in the Outdoor," in *2023 IEEE 4th International Conference on Electrical Materials and Power Equipment (ICEMPE)*, pp. 1-4, Shanghai, China, 2023.
- [65] L. Zeng, et al. "Study on Thermal Aging Characteristics of HTV Silicone Rubber Sheds of Composite Insulators." in *IOP Conference Series: Materials Science and Engineering*, vol. 782. no. 2. IOP Publishing, 2020.
- [66] Hedir et al., "Ultraviolet radiation aging impact on physicochemical properties of crosslinked polyethylene cable insulation," in *Journal of Applied Polymer Science*, vol. 137, no. 16, 2020.
- [67] X. Qiao, Y. Ming, K. Xu, N. Yi, and R. Sundararajan, "Aging of Polymeric Insulators under Various Conditions and Environments: Another Look," in *Energies*, vol. 15, no. 23, Nov. 2022.

References

- [68] G. Montoya, I. Ramirez and J.I. Montoya, "Correlation among ESDD, NSDD and leakage current in distribution insulators," in *Proc. IEE Gen. Trans. and Dist.*, vol. 151, no.3, pp. 334-340, 2004.
- [69] L. Maraaba et al., "Contamination Level Monitoring Techniques for High-Voltage Insulators: A Review," in *Energies*, vol. 15, no. 20, pp. 76-56, Oct. 2022.
- [70] IEC Standard 60815: "Guide for Selection of Insulators in Respect of Polluted Condition," 1986.
- [71] IEC Standard 60273: "Characteristic of Indoor and Outdoor Post Insulators for Systems with Nominal Voltages Greater than 1000V", 1990.
- [72] Y. Gao, X. Liang, W. Bao, S. Li and C. Wu, "Failure analysis of a field brittle fracture composite insulator: Characterization by FTIR analysis and fractography," in *IEEE Trans. on Dielectrics and Electrical Insulation*, vol. 25, no. 3, pp. 919-927, June 2018.
- [73] H. Ahmad, M.A. Salam, L.Y. Ying and N. Bashir, "Harmonic Components of Leakage Current as Diagnostic Tool to Study the Aging of Insulators", in *Journal of Electrostatics*, vol. 66, pp. 156-164, 2008.
- [74] M. Elad, *Sparse and Redundant Representations: From Theory to Applications*, in *Signal and Image Processing*, Springer, New York, USA, 2010.
- [75] K. Sit et al., "Mathematical Morphology aided Random Forest Classifier based High Voltage Porcelain Insulator Contamination Level Classification," in *2020 IEEE Region 10 Symposium (TENSYP)*, pp. 98-101, 2020.
- [76] S. Li et al., "A novel method to study the property of the interface between silicone rubber and fiber reinforced plastic," in *IEEE Trans. on Dielectrics and Electrical Insulation*, vol. 27, no. 2, pp. 658-665, April 2020.
- [77] Patil et al., "Fabrication of self-cleaning superhydrophobic silicone rubber insulator through laser texturing," in *Surface Engineering*, vol. 37, no. 3, page 308-317, 2021.
- [78] Z. Yan, X. Liang, Y. Gao and Y. Liu, "Aging and self-healing properties of superhydrophobic silicone rubber," in *IEEE Trans. on Dielectrics and Electrical Insulation*, vol. 23, no. 6, pp. 3531-3538, Dec. 2016.
- [79] Ahmadi-Joneidi et al., "Aging evaluation of silicone rubber insulators using leakage current and flashover voltage analysis," in *IEEE Trans. on Dielectrics and Electrical Insulation*, vol. 20, no. 1, pp. 212-220, February 2013.

References

- [80] Pierce et al., "Understanding of sliding and contact angle results in tilted plate experiments," in *Colloids and Surfaces A: Physicochemical and Engineering Aspects*, vol. 323, no. 1–3, Pages 73-82, ISSN 0927-7757, 2008.
- [81] M. H. Raza et al., "Surface Recovery Investigation of Silicone Rubber Composites for Outdoor Electrical Insulation under Accelerated Temperature and Humidity," in *Polymers*, vol. 13, no. 18, 2021.
- [82] N. Jahromi et al., "Aging Characteristics of RTV Silicone Rubber Insulator Coatings," in *IEEE Trans. on Dielectrics and Electrical Insulation*, vol. 15, no. 2, pp. 444-452, April 2008.
- [83] Y. Zhang et al., "Aging Process Evaluation Method of Silicone Rubber in Composite Insulators in Natural Environmental Experiment Station," in *IEEE Access*, vol. 7, pp. 169734-169744, 2019.
- [84] Y. Li, X. Wan, X. Liu, J. Nan and Y. Li, "Contamination Characteristics of Superhydrophobic Coated Insulators in Natural Environment and Artificial Simulation," in *2021 International Conference on Advanced Electrical Equipment and Reliable Operation (AEERO)*, pp. 1-6, 2021.
- [85] Banik, S. Dalai and B. Chatterjee, "Studies the effect of Equivalent Salt Deposit Density on leakage current and flashover voltage of artificially contaminated disc insulators," in *2015 1st Conference on Power, Dielectric and Energy Management at NERIST (ICPDEN)*, pp. 1-5, 2015.
- [86] S. H. Hamza et al., "Effect of desert environmental conditions on the flashover voltage of insulators," in *Energy Conversion and Management*, vol. 43, no. 17, pp. 2437-2442, 2002.
- [87] X. Liang et al., "Improving the outdoor insulation performance of Chinese EHV and UHV AC and DC overhead transmission lines," in *IEEE Electrical Insulation Magazine*, vol. 36, no. 4, pp. 7-25, July-Aug. 2020.
- [88] S. Wallström et al., "Microbiological growth testing of polymeric materials: an evaluation of new methods," in *Polymer Testing*, vol. 24, no. 5 pp. 557-563, 2005.
- [89] S. M. Gubanski et al., "Performance and Diagnostics of Biologically Contaminated Insulators," in *2006 IEEE 8th International Conference on Properties & applications of Dielectric Materials*, pp. 23-30, 2006.
- [90] M. N. Dinesh et al., "Performance of composite insulators with and without bio-contamination," in *2008 International Conference on High Voltage Engineering and Application*, pp. 124-127, 2008.

References

- [91] S. Kumagai and N. Yoshimura, "Hydrophobic transfer of RTV silicone rubber aged in single and multiple environmental stresses and the behavior of LMW silicone fluid," in *IEEE Trans. on Power Delivery*, vol. 18, no. 2, pp. 506-516, April 2003.
- [92] N. Md. Tariq and B. T. Phung, "Accelerated ultraviolet weathering investigation on micro-/nano-SiO₂ filled silicone rubber composites," in *High voltage*, vol. 3, no. 4, pp. 295-302, 2018.
- [93] Larsson, A. Roslund, S. Kroll and A. Dernfalk, "In-situ diagnostics of HV outdoor insulators using laser-induced fluorescence spectroscopy," in *IEEE Trans. on Dielectrics and Electrical Insulation*, vol. 9, no. 2, pp. 274-281, April 2002.
- [94] M. Wakhidin and Suwarno, "Effects of Artificial Tropical Climate Aging on Insulation Performance of Silicone Rubber Polymeric Insulators," in *2019 2nd International Conference on High Voltage Engineering and Power Systems (ICHVEPS)*, pp. 1-6, Denpasar, Indonesia, 2019.
- [95] Y. Lin et al., "Influence of vulcanization factors on UV-A resistance of silicone rubber for outdoor insulators," in *IEEE Trans. on Dielectrics and Electrical Insulation*, vol. 27, no. 1, pp. 296-304, Feb. 2020.
- [96] Y. Lin et al., "Effect of ultraviolet-A radiation on surface structure, thermal, and mechanical and electrical properties of liquid silicone rubber," in *Journal of Applied Polymer Science*, vol. 136, no. 24, 47652, 2019.
- [97] T. Asefa, and V. Dubovoy, "Ordered Mesoporous/Nanoporous Inorganic Materials via Self-Assembly," in *Nanotechnology Elsevier Inc.*, pp. 158-192, 2017.
- [98] L. Lan et al., "Characteristics of corona aged Nano-composite RTV and HTV silicone rubber," in *2013 Annual Report Conference on Electrical Insulation and Dielectric Phenomena*, pp. 804-808, Chenzhen, China, 2013.
- [99] W. Xilin et al., "In-situ and quantitative analysis of aged silicone rubber materials with laser-induced breakdown spectroscopy," in *IET Journals High Voltage*, vol. 3, no. 2, pp. 140-146, Jun 2018.
- [100] Y. Gao et al., "Degradation characteristics of epoxy resin of GFRP rod in the decay-like fracture of composite insulator," in *IEEE Trans. on Dielectrics and Electrical Insulation*, vol. 26, no. 1, pp. 107-114, Feb. 2019.
- [101] T. G. Gustavsson et al., "Aging of silicone rubber under ac or dc voltages in a coastal environment," in *IEEE Trans. on Dielectrics and Electrical Insulation*, vol. 8, no. 6, pp. 1029-1039, Dec. 2001.

References

- [102] H. Homma et al., "Evaluation of surface degradation of silicone rubber using gas chromatography/mass spectroscopy," in *IEEE Trans. on Power Delivery*, vol. 15, no. 2, pp. 796-803, April 2000.
- [103] S. Wallström, K. Dowling and S. Karlsson, "Development and comparison of test methods for evaluating formation of biofilms on silicones," in *Polymer degradation and stability*, vol. 78, no. 2, pp. 257-262, 2002.
- [104] R. S. Gorur, L. A. Johnson and H. C. Hervie, "Contamination performance of Silicone Rubber Cable Terminations," in *IEEE Trans. on Power Delivery*, vol. 6, no. 4, pp. 1366-1370, October 1991.
- [105] H. Mei et al., "Study on Detecting Dielectric Properties of Typical Electrical Insulation Materials by Terahertz Wave Spectroscopy," in *IEEE Access*, vol. 8, pp. 226887-226896, 2020.
- [106] L. Cheng et al., "Research of non-destructive methods to test defects hidden within composite insulators based on THz time-domain spectroscopy technology," in *IEEE Trans on Dielectrics and Electrical Insulation*, vol. 23, no. 4, pp. 2126-2133, August 2016.
- [107] H. Mei et al., "Detection of Small Defects in Composite Insulators Using Terahertz Technique and Deconvolution Method," in *IEEE Trans. on Instrumentation and Measurement*, vol. 69, no. 10, pp. 8146-8155, Oct. 2020.
- [108] X. Wang, H. Wang, C. Chen and Z. Jia, "Ablation Properties and Elemental Analysis of Silicone Rubber Using Laser-Induced Breakdown Spectroscopy," in *IEEE Transactions on Plasma Science*, vol. 44, no. 11, pp. 2766-2771, 2016.
- [109] X. Wang et al., "Surface Hardness Analysis of Aged Composite Insulators via Laser-Induced Plasma Spectra Characterization," in *IEEE Trans. on Plasma Science*, vol. 47, no. 1, pp. 387-394, Jan. 2019.
- [110] Waluyo, Fauziah and I. M. Khaidir, "The Evaluation of Daily Comparative Leakage Currents on Porcelain and Silicone Rubber Insulators Under Natural Environmental Conditions," in *IEEE Access*, vol. 9, pp. 27451-27466, 2021.
- [111] D. Pylarinos et al., "Investigation and classification of field leakage current waveforms," in *IEEE Transactions on Dielectrics and Electrical Insulation*, vol. 19, no. 6, pp. 2111-2118, December 2012.
- [112] Thalassinakis et al., "Measurements and Interpretations Concerning Leakage Currents on Polluted High Voltage Insulators", in *Meas. Sci. Techn.*, vol. 14, pp. 421-426, 2003.

References

- [113] K. Volkhov and D. Titov, "Diagnostics of Overhead Line Insulator State based on Leakage Current Regression Analysis," in *2023 International Conference on Industrial Engineering, Applications and Manufacturing (ICIEAM)*, pp. 45-51, Sochi, Russian Federation, 2023.
- [114] J.Y. Li, W.X. Sima, C.X. Sun. and S.A. Sebo, "Use of Leakage Currents of Insulators to Determine the Stage Characteristics of the Flashover Process and Contamination Level Prediction", in *IEEE Trans. Dielectr. Electr. Insul.*, Vol. 17, No.2, pp. 490–501, 2010.
- [115] D. Waluyo et al., "The Evaluation of Daily Comparative Leakage Currents on Porcelain and Silicone Rubber Insulators Under Natural Environmental Conditions," in *IEEE Access*, vol. 9, pp. 27451-27466, 2021.
- [116] D. Pylarinos et al., "Investigation and classification of field leakage current waveforms," in *IEEE Transactions on Dielectrics and Electrical Insulation*, vol. 19, no. 6, pp. 2111-2118, December 2012.
- [117] H.H. Kordkheili et al., "Determining the Probability of Flashover Occurrence in Composite Insulators by Using Leakage Current Harmonic Components", in *IEEE Trans. Dielectr. Electr. Insul.*, vol. 17, pp. 502-512, 2010.
- [118] S. Nandi and B. S. Reddy, "Understanding field failures of composite insulators," in *Engineering Failure Analysis*, in *Elsevier*, vol. 116, no. 104758, ISSN 1350-6307, 2020.
- [119] S. Kumagai, "Influence of Algal Fouling on Hydrophobicity and Leakage Current on Silicone Rubber," in *IEEE Trans. on Dielectrics and Electrical Insulation*, vol. 14, no. 5, pp. 1201-1206, October 2007.
- [120] S. Chandrasekar et al., "Partial discharge detection as a tool to infer pollution severity of polymeric insulators," in *IEEE Trans. on Dielectrics and Electrical Insulation*, vol. 17, no. 1, pp. 181-188, February 2010.
- [121] R. Ullah and Md. Akbar, "Effect of AC stressed aging on partial discharge, thermal and tensile performance of silicone rubber-based composites," in *Composites Communications*, *Elsevier*, vol. 24, ISSN 2452-2139, 2021.
- [122] Yang et al., "Analysis of the Influence of Silicone Rubber Aging on the Transmission Parameters of Terahertz Waves," in *Energies*, *Elsevier*, vol. 14, no. 14, p. 4238, Jul. 2021.
- [123] Qi et al., "Surface discharge initiated by immobilized metallic particles attached to gas insulated substation insulators: process and features," in *IEEE Trans. on Dielectrics and Electrical Insulation*, vol. 18, no. 3, pp. 792-800, June 2011.

References

- [124] M. H. Nazemi and V. Hinrichsen, "Experimental investigations on partial discharge characteristics of water droplets on polymeric insulating surfaces at AC, DC and combined AC-DC voltages," in *IEEE Trans. on Dielectrics and Electrical Insulation*, vol. 22, no. 4, pp. 2261-2270, August 2015.
- [125] M. T. Nazir et al., "Resistance against AC corona discharge of micro-ATH / nano-Al₂O₃ co-filled silicone rubber composites," in *IEEE Trans. on Dielectrics and Electrical Insulation*, vol. 25, no. 2, pp. 657-667, April 2018.
- [126] M. T. Nazir, B. T. Phung and M. Hoffman, "Performance of silicone rubber composites with SiO₂ micro/nano-filler under AC corona discharge," in *IEEE Trans. on Dielectrics and Electrical Insulation*, vol. 23, no. 5, pp. 2804-2815, October 2016.
- [127] Y. Zhu et al., "Aging performance of silicone rubber exposed to UV and sandstorm," in *2013 Annual Report Conference on Electrical Insulation and Dielectric Phenomena*, pp. 426-429, 2013.
- [128] M. Bi et al., "Study on Corona Aging Characteristics of Silicone Rubber Material Under Different Environmental Conditions," in *IEEE Trans. on Dielectrics and Electrical Insulation*, vol. 29, no. 2, pp. 534-542, April 2022.
- [129] M. Schneider et al., "Accelerated aging and flashover tests on 138 kV nonceramic line post insulators," in *IEEE Trans. on Power Delivery*, vol. 8, no. 1, pp. 325-336, Jan. 1993.
- [130] S. Khatoun and A. A. Khan, "Influence of Different Contaminants with Clean Steam fog on the Flashover behavior of Porcelain and Polymeric Insulators: An Experimental Study," in *2019 International Conference on Electrical, Electronics and Computer Engineering (UPCON)*, pp. 1-6, 2019.
- [131] J.D. Samakosh and M Mirzaie, "Experimental-based models for predicting the flashover voltage of polluted SiR insulators using leakage current characteristics," in *IET Science, Measurement & Technology*, vol. 14, no. 10, p. 943 – 952, December 20, 2020.
- [132] M. Albano et al., "Infrared analysis of dry-band flashover of silicone rubber insulators," in *IEEE Trans. on Dielectrics and Electrical Insulation*, vol. 23, no. 1, pp. 304-310, February 2016.
- [133] W. Fang et al., "Investigation of the tracking and erosion resistance of cured liquid silicone rubber containing ureido-modified MQ silicone resin," in *IEEE Trans. on Dielectrics and Electrical Insulation*, vol. 23, no. 6, pp. 3668-3675, Dec. 2016.

References

- [134] M. T. Nazir et al., "Erosion resistance of micro-AlN and nano-SiO₂ hybrid filled silicone rubber composites," in *2017 International Symposium on Electrical Insulating Materials (ISEIM)*, pp. 370-373, 2017.
- [135] R. A. Ghunem, "Using the inclined-plane test to evaluate the resistance of outdoor polymer insulating materials to electrical tracking and erosion," in *IEEE Electrical Insulation Magazine*, vol. 31, no. 5, pp. 16-22, Sept.-Oct. 2015.
- [136] U. Asad et al., "The tracking and erosion performance of silicone rubber incorporated with novel TiO₂@ SiO₂ core-shell nanofillers under the IEC 60587 standard," in *Materials Research Express*, vol. 7, no. 2, 4th February 2020.
- [137] M. Dutta and C. K. Dwivedi, "Liquid-Contaminant: Inclined Plane Tracking and Erosion of Insulating Materials," in *2010 3rd International Conference on Emerging Trends in Engineering and Technology*, pp. 235-240, 2010.
- [138] L. E. Schmidt et al., "Tracking and erosion resistance of high temperature vulcanizing ATH-free silicone rubber," in *IEEE Trans. on Dielectrics and Electrical Insulation*, vol. 17, no. 2, pp. 533-540, April 2010.
- [139] Guo et al., "Characteristic properties of High Consistency Rubber and Liquid Silicone Rubber," in *2018 IEEE Conference on Electrical Insulation and Dielectric Phenomena (CEIDP)*, pp. 223-226, 2018.
- [140] H. El-Hag, L. C. Simon, S. H. Jayaram and E. A. Cherney, "Erosion resistance of nano-filled silicone rubber," in *IEEE Trans. on Dielectrics and Electrical Insulation*, vol. 13, no. 1, pp. 122-128, Feb. 2006.
- [141] S. Bian, S. Jayaram and E. A. Cherney, "Erosion resistance of electrospun silicone rubber nanocomposites," in *IEEE Trans. on Dielectrics and Electrical Insulation*, vol. 20, no. 1, pp. 185-193, February 2013.
- [142] Arshad, A. Nekahi, S. McMeekin, and M. Farzaneh, "Flashover Characteristics of Silicone Rubber Sheets under Various Environmental Conditions," in *Energies*, vol. 9, no. 9, p. 683, Aug. 2016.
- [143] Arshad et al., "Effect of pollution severity and dry band location on the flashover characteristics of silicone rubber surfaces," in *Electrical Engineering, Springer link*, vol. 99, pp. 1053–1063, 2017.

References

- [144] N. Bashir and H. Ahmad, "Odd Harmonics and Third to Fifth Harmonic Ratios of Leakage Currents as Diagnostic Tools to Study the Ageing of Glass Insulators." in *IEEE Trans. on Dielectrics and Electrical Insulation*, vol. 17, no. 3, pp. 819-832, 2010.
- [145] S. Deb et al., "Estimation of Contamination Level of Overhead Insulators Based on Surface Leakage Current Employing Detrended Fluctuation Analysis," in *IEEE Trans. Indus. Electr.*, vol. 67, no. 7, pp. 5729-5736, 2020.
- [146] A. Banik, S. Dalai, and B. Chatterjee, "Autocorrelation aided rough set-based contamination level prediction of high voltage insulator at different environmental condition," in *IEEE Trans. Dielectric Electr. Insul.*, vol. 23, no. 5, pp. 2883-2891, 2016.
- [147] IEC TS 60815-1:2008 (2008, Oct. 28), "Selection and dimensioning of high-voltage insulators intended for use in contaminated conditions - Part 1: Definitions, information and general principles" [Online], Available: <https://webstore.iec.ch/publication/3573>.
- [148] IEC Standard 60060-3:2006, "High Voltage Test Techniques - Part 3: Definitions and Requirements for on-site Testing," 2006.
- [149] IEC 60507:2013 (2013, Dec. 13), Artificial contamination tests on high-voltage ceramic and glass insulators to be used on a.c systems [online]. Available: <https://webstore.iec.ch/publication/2277>.
- [150] S. Deb et al., "Short Time Modified Hilbert Transform-Aided Sparse Representation for Sensing of Overhead Line Insulator Contamination," in *IEEE Sensors J.*, vol. 18, no. 19, pp. 8125-8132, 1 2018.
- [151] J. Serra, "Image Analysis and Mathematical Morphology," New York: Academic, 1982.
- [152] T. Asplund et al., "A new approach to mathematical morphology on one dimensional sampled signals," in *2016 23rd International Conference on Pattern Recognition (ICPR)*, 2016, pp. 3904-3909.
- [153] S. Gautam, and S. M. Brahma, "Overview of mathematical morphology in power systems — A tutorial approach," in *2009 IEEE Power & Energy Society General Meeting*, Calgary, pp. 1-7, 2009.
- [154] A. Baug et al., "Identification of single and multiple partial discharge sources by optical method using mathematical morphology aided sparse representation classifier," in *IEEE Trans. Dielectric and Electrical Insulations*, vol. 24, no. 6, pp. 3703-3712, 2017.
- [155] G. Matheron, "Random Sets and Integral Geometry", New York: Wiley Publication, 1975.
- [156] L. Breiman, "Random Forests", in *Machine Learning*, vol. 45, pp. 5-32, 2001.

References

- [157] N. Haque et al., "Accurate Sensing of Power Transformer Faults from Dissolved Gas Data Using Random Forest Classifier Aided by Data Clustering Method," in *IEEE Sensors Journal*, vol. 22, no. 6, pp. 5902-5910, 15 March 2022.
- [158] S. S. Roy, S. Dey, and S. Chatterjee, "Autocorrelation Aided Random Forest Classifier Based Bearing Fault Detection Framework," in *IEEE Sensors J.*, vol. 20, no. 18, pp. 10792-10800, 2020.
- [159] T. Sorqvist and A. E. Vlastos, "Outdoor Polymeric Insulators Long-Term Exposed to HVDC", in *IEEE Transactions on Power Delivery*, vol. 12, no. 2, pp. 1041-1048, 1997.
- [160] C. N. Richards and J. D. Renowden, "Development of a Remote Insulator Contamination Monitoring System", in *IEEE Transactions on Power Delivery*, vol. 2, no. 1, pp. 389-397, 2005.
- [161] S. Chatterjee, S. S. Roy, K. Samanta and S. Modak, "Sensing Wettability Condition of Insulation Surface Employing Convolutional Neural Network," in *IEEE Sensors Letters*, vol. 4, no. 7, pp. 1-4, July 2020.
- [162] S. Chatterjee and M. H. Nazemi, "Influence of viscosity and conductivity of water droplets on partial discharge inception voltage of polymeric insulating surfaces," in *Proceeding of 1st IEEE Int. Conf. Energy Power Environ.*, pp. 1-4. Shillong, India, 2015.
- [163] I. Gutman and A. Dernfalk, "Pollution tests for polymeric insulators made of hydrophobicity transfer materials," in *IEEE Transactions on Dielectrics and Electrical Insulation*, vol. 17, no. 2, pp. 384-393, 2010.
- [164] A. Arshad, S. Nekahi, G. McMeekin and M. Farzaneh, "Effect of pollution severity on electric field distribution along a polymeric insulator," in *Proceedings of 2015 IEEE 11th International Conference on the Properties and Applications of Dielectric Materials (ICPADM)*, Sydney, NSW, 2015, pp. 612-615.
- [165] Yu-Hsiang Wang, "The Tutorial: S Transform," 2010.
- [166] R. G. Stockwell, L. Mansinha and R. P. Lowe, "Localization of the complex spectrum: the S transform," in *IEEE Transactions on Signal Processing*, vol. 44, no. 4, pp. 998-1001, April 1996.
- [167] N. R. Choudhury, S. S. Roy, A. Pal, S. Chatterjee and R. Bose, "Epileptic Seizure Detection Employing Cross-Hyperbolic Stockwell Transform," in *Proceedings of 2018 Fourth International Conference on Research in Computational Intelligence and Communication Networks (ICRCICN)*, pp. 70-74, Kolkata, India, 2018.

References

- [168] S. Chatterjee, K. Samanta, N. R. Choudhury and R. Bose, "Detection of Myopathy and ALS Electromyograms Employing Modified Window Stockwell Transform," in *IEEE Sensors Letters*, vol. 3, no. 7, pp. 1-4, 2019.
- [169] X. Zeng, Y. Liao and W. Li, "Gearbox fault classification using S-transform and convolutional neural network," Proceedings of 2016 10th International Conference on Sensing Technology (ICST), pp. 1-5, Nanjing, 2016.
- [170] A. K. Das, S. Dalai and B. Chatterjee, "Cross Stockwell transform aided Random Forest based surface condition identification of Metal Oxide Surge Arrester employing Leakage current signal," in *Proceedings of 2020 IEEE Region 10 Symposium (TENSYP)*, pp. 1775-1778, Dhaka, Bangladesh, 2020.
- [171] M. Venkateswara Reddy and R. Sodhi, "A Modified S-Transform and Random Forests-Based Power Quality Assessment Framework," in *IEEE Transactions on Instrumentation and Measurement*, vol. 67, no. 1, pp. 78-89, Jan. 2018.
- [172] A. Ashrafian, M. Rostami and G. B. Gharehpetian, "Hyperbolic S-transform-based method for classification of external faults, incipient faults, inrush currents and internal faults in power transformers", in *IET Generation, Transmission & Distribution*, vol. 6, no. 10, pp. 940-950, October 2012.
- [173] A. K. Das, B. Ghosh, S. Dalai and B. Chatterjee, "Sensing Surface Contamination of Metal Oxide Surge Arrester Through Resistive Leakage Current Signal Analysis by Mathematical Morphology," in *IEEE Sensors Journal*, vol. 20, no. 16, pp. 9460-9468, 15 Aug, 2020.
- [174] V. Vapnik and C. Cortes, 'Support vector networks', in *Machine Learning*, vol. 20, no. 3, pp. 273–295, 1995.
- [175] F. F. Chamasemani and Y. P. Singh, "Multi-class Support Vector Machine (SVM) Classifiers -- An Application in Hypothyroid Detection and Classification," in *Proceedings of 2011 Sixth International Conference on Bio-Inspired Computing: Theories and Applications*, Penang, pp. 351-356, 2011.
- [176] I. Banerjee, S. S. Mullick, and S. Das, "On Convergence of the Class Membership Estimator in Fuzzy k-Nearest Neighbor Classifier," in *IEEE Trans. Fuzzy Syst.*, vol. 27, no. 6, pp. 1226–1236, 2018.
- [177] T. Zhang, W. Chen, and M. Li, "AR based quadratic feature extraction in the VMD domain for the automated seizure detection of EEG using random forest classifier," in *Biomed. Signal Process. Control*, vol. 31, pp. 550–559, Jan. 2017.

References

- [178] F. Pedregosa, et al., "Scikit-learn: Machine learning in python," in *Journal of machine learning research*, vol. 12, no. Oct, pp. 2825–2830, 2011.
- [179] F. Li, Y. Yang, and E. P. Xing, "From LASSO regression to feature vector machine." in *Advances in Neural Information Processing Systems*, vol. 18, pp. 779-786, 2005.
- [180] R. Muthukrishnan, and R. Rohini, "LASSO: A feature selection technique in predictive modeling for machine learning," in *IEEE International Conference on Advances in Computer Applications (ICACA)*, Coimbatore, pp. 18-20, 2016.
- [181] Christopher J. C. Burges, "A Tutorial on Support Vector Machines for Pattern Recognition," in *Data Mining and Knowledge Discovery*, vol. 2, no. 2, pp. 121–167, 1998.
- [182] S. Koroglu, and A. Demircali, "Diagnosis of Power Transformer Faults Based on Multi-layer Support Vector Machine Hybridized with Optimization Methods," in *Electric Power Components and Systems*, vol. 44, no. 19, pp. 2172-2184, 2016.
- [183] S. Dalai et al., "Cross-Spectrum Analysis-Based Scheme for Multiple Power Quality Disturbance Sensing Device," in *IEEE Sensors Journal*, vol. 15, no. 7, pp- 3989-3997, 2015.
- [184] K. Taunk et al., "A Brief Review of Nearest Neighbor Algorithm for Learning and Classification," in *2019 International Conference on Intelligent Computing and Control Systems (ICCS)*, pp. 1255-1260, 2019.
- [185] "Naïve Bayes classification algorithm," Available (online): <http://software.ucv.rp/air/docs/naivebayes.pdf>, Feb 2015.
- [186] L. Jiang et al., "Naive bayes text classifiers a locally weighted learning approach," in *Journal of Experimental & Theoretical Artificial Intelligence*, vol. 25, no. 2, pp. 273–286, 2013.
- [187] N. Haque et al., "Accurate Sensing of Power Transformer Faults from Dissolved Gas Data Using Random Forest Classifier Aided by Data Clustering Method," in *IEEE Sensors Journal*, vol. 22, no. 6, pp. 5902-5910, 15 March 15, 2022.
- [188] R. G. Stockwell, L. Mansinha, and R. P. Lowe, "Localization of the complex spectrum: the S transform," in *IEEE Trans. Signal Process.*, vol. 44, no. 4, pp. 998-1001, 1996.
- [189] A. H. El-Hag, "A new technique to detect dry-band arcing," in *IEEE Transactions on Power Delivery*, vol. 20, no. 2, pp. 1202-1203, April 2005.

References

- [190] H. R. Sezavar, N. Fahimi and A. A. Shayegani, "A Dynamic Intelligent Approach Based on Gaussian Function for Prediction of the Flashover Voltage Conditions on Polluted Polymer Insulators," in *IEEE Transactions on Power Delivery*, vol. 37, no. 5, pp. 3458 - 3468, Oct. 2022.
- [191] S. Nandi and S. R. B, "Transient Electric Field Analysis for Polluted Composite Insulators Under HVDC Stress," in *IEEE Transactions on Power Delivery*, vol. 36, no. 2, pp. 607-617, April 2021.
- [192] H. de Santos and M. Á. Sanz-Bobi, "A Cumulative Pollution Index for the Estimation of the Leakage Current on Insulator Strings," in *IEEE Transactions on Power Delivery*, vol. 35, no. 5, pp. 2438-2446, Oct. 2020.
- [193] M. F. Palangar, S. Mohseni, M. Mirzaie and A. Mahmoudi, "Designing an Automatic Detector Device to Diagnose Insulator State on Overhead Distribution Lines," in *IEEE Transactions on Industrial Informatics*, vol. 18, no. 2, pp. 1072-1082, Feb. 2022.
- [194] C. Engelbrecht, I. Gutman and R. Hartings, "A Practical Implementation of Statistical Principles to Dimension AC Line Insulators with Respect to Contaminated Conditions," in *IEEE Transactions on Power Delivery*, vol. 22, no. 1, pp. 667-673, Jan. 2007.
- [195] A. K. Chaou, A. Mekhaldi and M. Tegar, "Recurrence quantification analysis as a novel LC feature extraction technique for the classification of contamination severity on HV insulator model," in *IEEE Trans. on Dielectrics and Electrical Insulation*, vol. 22, no. 6, pp. 3376-3384, December 2015.
- [196] G. Heger, H. J. Vermeulen, J. P. Holtzhausen and W. L. Vosloo, "A comparative study of insulator materials exposed to high voltage AC and DC surface discharges," in *IEEE Transactions on Dielectrics and Electrical Insulation*, vol. 17, no. 2, pp. 513-520, April 2010.
- [197] S. Chatterjee, N. R. Choudhury, and R. Bose, "Detection of epileptic seizure and seizure-free EEG signals employing generalized S - transform," in *IET Science, Measurement & Technology*, vol. 11, np. 7, pp. 847 – 855, October 2017.
- [198] X. Zhang et al., "InsuDet: A Fault Detection Method for Insulators of Overhead Transmission Lines Using Convolutional Neural Networks," in *IEEE Transactions on Instrumentation and Measurement*, vol. 70, pp. 1-12, Art no. 5018512, 2021.
- [199] X. Huang, E. Shang, J. Xue, H. Ding and P. Li, "A Multi-feature Fusion-based Deep Learning for Insulator Image Identification and Fault Detection," in *2020 IEEE 4th Information Technology, Networking, Electronic and Automation Control Conference (ITNEC)*, pp. 1957-1960, Chongqing, China, 2020.

References

- [200] A. Behvandi, S. G. Seifossadat and A. Saffarian, "A new method for discrimination of internal fault from other transient states in power transformer using Clarke's transform and modified hyperbolic S-transform" in *Electric Power Systems Research*, vol. 178, no. 106023, ISSN, pp. 0378-7796, 2020.
- [201] B. Ganguly, D. Dey and S. Munshi, "Image Visibility Filter-Based Interpretable Deep Learning Framework for Skin Lesion Diagnosis," in *IEEE Trans on Industrial Informatics*, vol. 18, no. 8, pp. 5138-5147, Aug. 2022.
- [202] S. Shao, S. McAleer, R. Yan and P. Baldi, "Highly Accurate Machine Fault Diagnosis Using Deep Transfer Learning," in *IEEE Trans. on Industrial Informatics*, vol. 15, no. 4, pp. 2446-2455, April 2019.
- [203] A. Shamsi *et al.*, "An Uncertainty-Aware Transfer Learning-Based Framework for COVID-19 Diagnosis," in *IEEE Trans. on Neural Networks and Learning Systems*, vol. 32, no. 4, pp. 1408-1417, 2021.
- [204] S. K. Khare, V. Bajaj and U. R. Acharya, "SPWVD-CNN for Automated Detection of Schizophrenia Patients Using EEG Signals," in *IEEE Trans. on Instrumentation and Measurement*, vol. 70, pp. 1-9, 2021.
- [205] K. Simonyan and A. Zisserman, "Very Deep Convolutional Networks for Large-Scale Image Recognition," *arXiv preprint arXiv:1409.1556*, 2014.
- [206] D. Dey et al., "A deep learning framework using convolution neural network for classification of impulse fault patterns in transformers with increased accuracy," in *IEEE Trans. on Dielectric and Electrical Insulation*, vol. 24, no. 6, pp. 3894-3897, 2017.
- [207] X. Peng et al., "A Convolutional Neural Network-Based Deep Learning Methodology for Recognition of Partial Discharge Patterns from High Voltage Cables," in *IEEE Trans. on Power Delivery*, vol. 34, no. 4, pp. 1460-1469, 2019.
- [208] S. Singha Roy et al., "Cross Spectrum Aided Deep Feature Extraction Based Neuromuscular Disease Detection Framework," in *IEEE Sensor Letter*, vol. 4, no. 6, pp. 1-4, 2020.
- [209] S. Chakravorti, D. Dey, and B. Chatterjee, "Recent Trends in the Condition Monitoring of Transformers," in *Power Systems*. Springer, London, 2013.